

AFWAL-TR-85-2085

METHODS OF PLASMA EXCITATION

J. R. Twist  
V. E. Merchant  
M. L. Lake



Universal Energy Systems, Inc.  
4401 Dayton-Xenia Road  
Dayton, Ohio 45432

December 1985

Final Report for Period September 1980 - September 1984

Approved for public release; distribution is unlimited

AD-A170 347

DTIC FILE COPY

DTIC  
ELECTE  
JUL 29 1986  
S D D

Aero Propulsion Laboratory  
AIR FORCE WRIGHT AERONAUTICAL LABORATORIES  
AIR FORCE SYSTEMS COMMAND  
WRIGHT-PATTERSON AIR FORCE BASE, OHIO 45433

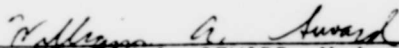
86 7 29 094

NOTICE

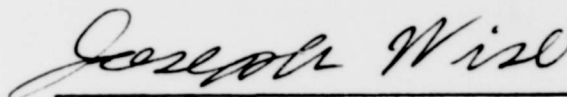
When Government drawings, specifications, or other data are used for any purpose other than in connection with a definitely related Government procurement operation, the United States Government thereby incurs no responsibility nor any obligation whatsoever; and the fact that the government may have formulated, furnished, or in any way supplied the said drawings, specifications, or other data, is not to be regarded by implication or otherwise as in any manner licensing the holder or any other person or corporation, or conveying any rights or permission to manufacture use, or sell any patented invention that may in any way be related thereto.

This report has been reviewed by the Office of Public Affairs (ASD/PA) and is releasable to the National Technical Information Service (NTIS). At NTIS, it will be available to the general public, including foreign nations.

This technical report has been reviewed and is approved for publication.

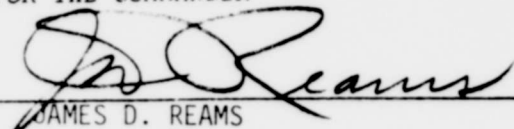


WILLIAM A. SEWARD, Maj  
TAM, Power Components Branch  
Aerospace Power Division  
Aero Propulsion Laboratory



JOSEPH F. WISE, Acting Chief  
Power Components Branch  
Aerospace Power Division  
Aero Propulsion Laboratory

FOR THE COMMANDER



JAMES D. REAMS  
Chief, Aerospace Power Division  
Aero Propulsion Laboratory

"If your address has changed, if you wish to be removed from our mailing list, or if the addressee is no longer employed by your organization please notify AFNAL/POOC-3 W-PAFB, OH 45433 to help us maintain a current mailing list".

Copies of this report should not be returned unless return is required by security considerations, contractual obligations, or notice on a specific document.

## REPORT DOCUMENTATION PAGE

1a. REPORT SECURITY CLASSIFICATION UNCLASSIFIED		1b. RESTRICTIVE MARKINGS	
2a. SECURITY CLASSIFICATION AUTHORITY		3. DISTRIBUTION/AVAILABILITY OF REPORT Approved for public release; distribution is unlimited.	
2b. DECLASSIFICATION/DOWNGRADING SCHEDULE			
4. PERFORMING ORGANIZATION REPORT NUMBER(S)		5. MONITORING ORGANIZATION REPORT NUMBER(S) AFWAL-TR-85-2085	
6a. NAME OF PERFORMING ORGANIZATION Universal Energy Systems, Inc.		6b. OFFICE SYMBOL (If applicable)	7a. NAME OF MONITORING ORGANIZATION Aero Propulsion Laboratory (AFWAL/POOC) Air Force Wright Aeronautical Laboratories
6c. ADDRESS (City, State and ZIP Code) 4401 Dayton-Xenia Road Dayton, Ohio 45432		7b. ADDRESS (City, State and ZIP Code) Air Force Systems Command Wright-Patterson Air Force Base, OH 45433	
8a. NAME OF FUNDING/SPONSORING ORGANIZATION Power Components Branch Aero Propulsion Laboratory	8b. OFFICE SYMBOL (If applicable) AFWAL/POOC-3	9. PROCUREMENT INSTRUMENT IDENTIFICATION NUMBER F33615-80-C-2062	
8c. ADDRESS (City, State and ZIP Code) Air Force Wright Aeronautical Laboratory Wright-Patterson AFB, OH 45433		10. SOURCE OF FUNDING NOS.	
11. TITLE (Include Security Classification) Methods of Plasma Excitation		PROGRAM ELEMENT NO. 61102F	PROJECT NO. 2301
		TASK NO. 52	WORK UNIT NO. 84
12. PERSONAL AUTHOR(S) J. R. Twist, V. E. Merchant, M. L. Lake			
13a. TYPE OF REPORT Final	13b. TIME COVERED FROM 9/80 TO 9/84	14. DATE OF REPORT (Yr., Mo., Day) December 1985	15. PAGE COUNT 154
16. SUPPLEMENTARY NOTATION			
17. COSATI CODES		18. SUBJECT TERMS (Continue on reverse if necessary and identify by block number)	
FIELD	GROUP	SUB. GR.	
20	09		
20	05		
19. ABSTRACT (Continue on reverse if necessary and identify by block number) This report covers three areas. The first section deals with microwave excitation of small volumes. The work emphasized microwave excitation on mercury bromide. In addition, some discharges were performed in silane gas mixes and in sulphur. The florescence produced by the gas is studied as a function of discharge parameters. The transient conductivity of 1/9 nitrogen/argon gas mixes in pulsed high power atmospheric pressure discharges is studied in the second section. The discharge was produced in a U.V. preionized gas and produced a peak current of about 10 amps per square centimeter. The voltage from a capacitor bank was applied to the discharge electrodes by means of triggered spark gap a set delay after the surface preionizers had fired. Data is presented that shows the transient discharge voltage and current as well as the power dissipated in the gas and the resistivity of the discharge as a function of time.			
20. DISTRIBUTION/AVAILABILITY OF ABSTRACT UNCLASSIFIED/UNLIMITED <input checked="" type="checkbox"/> SAME AS RPT. <input type="checkbox"/> DTIC USERS <input type="checkbox"/>		21. ABSTRACT SECURITY CLASSIFICATION Unclassified	
22a. NAME OF RESPONSIBLE INDIVIDUAL William A. Seward, Maj, USAF		22b. TELEPHONE NUMBER (Include Area Code) (513) 255-2923	22c. OFFICE SYMBOL AFWAL/POOC-3

## Block 19, ABSTRACT Continued

The two body ion recombination coefficient for the 1/9 Nitrogen/Argon mix was determined by analyzing the discharge current and voltage. A value of  $1.08 \times 10^{-6}$  cm<sup>3</sup>/sec was determined for the recombination coefficient at an E/N of 9.14 Townsends.

The third section includes data on the dissociative excitation of mercurous bromide by low (10 eV) energy electron beams. The excitation process was studied by measuring the fluorescence produced by fragments of the collision process mainly mercury bromide. The optical cross section for the production of fluorescence in the wavelength range of 300 to 550 nm was determined.

# ACKNOWLEDGMENT

A project such as this can never be done without the help of many people. This will serve to acknowledge some of those who contributed. J. R. Twist would like to thank Bob Olsen, Dennis Grosjeans and Ben Sarka of SRL who freely shared their knowledge.

Jim Ray of AFWAL made the main H. V. feedthrough and made it possible to get the TESLA functioning. Peter Bletzinger contributed many plasma references and helpful discussions on the operation of atmospheric pressure glow discharges. Cliff Van Sickle continued to provide assistance and encouragement long after his formal association with UES had been severed.

Alan Garscadden served as the corner-stone of the project by his intense interest in the physics of the projects.

Final thanks to Charles DeJoeseh who helped stretch the last dollars in the closing hours of the contract.

Accession For	
NTIS CRA&I	<input checked="" type="checkbox"/>
DTIC TAB	<input type="checkbox"/>
Unannounced	<input type="checkbox"/>
Justification	
By	
Distribution/	
Availability Codes	
Dist	Avail and/or Special
A-1	



## TABLE OF CONTENTS

<u>SECTION</u>	<u>TITLE</u>	<u>PAGE</u>
I	MICROWAVE DISCHARGES . . . . .	1-1
	POWER LOADING IN A MICROWAVE EXCITED DISCHARGE . . . . .	1-1
	APPARATUS . . . . .	1-1
	APPLICATOR TYPES . . . . .	1-2
	MODELING OF THE PLASMA LOAD . . . . .	1-8
	MICROWAVE EXCITATION OF A SILANE-ARGON MIXTURE . . . . .	1-13
	MICROWAVE EXCITATION OF MERCURY BROMIDE PLASMAS . . . . .	1-15
	REFERENCES . . . . .	1-36
II	PULSED DISCHARGE SYSTEM TESLA . . . . .	2-1
	INTRODUCTIONS & METHOD . . . . .	2-1
	GAS MIXTURES FOR OPENING SWITCHES . . . . .	2-1
	ANALYSIS OF PULSED DISCHARGES . . . . .	2-4
	ION KINETICS IN ARGON-NITROGEN MIXTURE . . . . .	2-6
	EXPERIMENTAL APPARATUS . . . . .	2-7
	TESLA RESULTS . . . . .	2-20
	REFERENCES . . . . .	2-31
III	ELECTRON DISSOCIATIVE IMPACT EXCITATION OF HgBr <sub>2</sub> . . . . .	3-1
	INTRODUCTION . . . . .	3-1
	EXPERIMENTAL APPARATUS . . . . .	3-2
	METHOD . . . . .	3-9
	RESULTS & DISCUSSION . . . . .	3-29
	REFERENCES . . . . .	3-50
APPENDIX A	STANDARD OPERATING PROCEDURE . . . . .	A-1
APPENDIX B	MEASUREMENT OF TEMPERATURE IN ARGON NITROGEN DISCHARGES . . . . .	B-1

## LIST OF ILLUSTRATIONS

<u>FIGURE</u>	<u>DESCRIPTION</u>	<u>PAGE</u>
1-1	Dependence of length of discharge on the HgBr <sub>2</sub> pressure.	1-3
1-2	Reflection coefficient for simple model of applicator.	1-10
1-3	Transmission coefficient for simple model of applicator.	1-11
1-4	Fraction of power absorbed in applicator in simple model.	1-12
1-5	Dependence of emission from HgBr on HgBr <sub>2</sub> pressure and effect of gas mixes containing N <sub>2</sub> .	1-17
1-6	Dependence of emission from HgBr on HgBr <sub>2</sub> and Helium pressure.	1-18
1-7	Details of the HgBr B-X emission: Dependence of ratio of emission at 500 nm to that at 475 nm on HgBr <sub>2</sub> pressure.	1-20
1-8	Details of the HgBr B-X emission: Dependence of ratio of emission at 420 nm to that at 475 nm on HgBr <sub>2</sub> pressure.	1-21
1-9	Dependence of emission from Hg and Helium on the HgBr <sub>2</sub> pressure.	1-23
1-10	Dependence of emission from three lines of ionic Bromine on the HgBr <sub>2</sub> pressure.	1-24
1-11	Ratio of emission from atomic mercury to that from mercury bromide. Dependence on temperature of discharge tube.	1-26
1-12	Ratio of emission from atomic mercury to that from mercury bromide. Dependence on mode of excitation.	1-27
1-13	Dependence of emission from helium and from nitrogen on HgBr <sub>2</sub> pressure in a discharge tube containing He, N <sub>2</sub> , and HgBr <sub>2</sub> .	1-28
1-14	Electron energy distribution functions.	1-30
1-15	Electronic excitation cross-sections of nitrogen.	1-31
1-16	Time dependence of emission from mercury bromide and from mercury.	1-33
2-1	TESLA vacuum system	2-8
2-2	TESLA gas manifold mixing system	2-9
2-3	TESLA electrical diagram	2-11

LIST OF ILLUSTRATIONS (Continued)

<u>FIGURE</u>	<u>DESCRIPTION</u>	<u>PAGE</u>
2-4	TESLA main electrical discharge system	2-13
2-5	Thyratron trigger unit	2-15
2-6	Voltage and current vs. time raw data	2-16
2-7	High voltage feed through	2-18
2-8	Test of preionizers	2-19
2-9	Uncorrected discharge voltage vs. time	2-21
2-10	Discharge current vs. time	2-22
2-11	Corrected discharge voltage vs. time	2-24
2-12	Resistivity of discharge vs. time	2-25
2-13	Power dissipated in switch vs. time	2-26
2-14	Discharge resistivity vs. current density	2-27
3-1	Experimental apparatus	3-3
3-2	Electron gun schematic diagram	3-7
3-3	HgBr <sub>2</sub> fluorescence signal vs. pressure	3-17
3-4	He fluorescence signal vs. pressure	3-18
3-5	Hg fluorescence signal vs. beam current	3-20
3-6	He optical cross section	3-22
3-7	HgBr <sub>2</sub> spectra	3-30
3-8	Excitation function of HgBr <sub>2</sub>	3-33
3-9	Normalized detector response	3-38
3-10	Uncorrected HgBr <sub>2</sub> spectra	3-39
3-11	Corrected HgBr <sub>2</sub> spectra	3-40
3-12	HgBr <sub>2</sub> excitation function	3-45
3-13	Hg excitation function	3-48



LIST OF TABLES

<u>TABLES</u>	<u>DESCRIPTION</u>	<u>PAGE</u>
1-1	Microwave-Plasma-Coupling-Devices . . . . .	1-4
1-2	Tube Inventory . . . . .	1-14
2-1	Ion Reactions in Nitrogen-Argon Mixtures . . . . .	2-30
3-1	Beam Current Versus Acceleration Voltage . . . . .	3-16

## SECTION 1

### MICROWAVE DISCHARGES

#### POWER LOADING IN A MICROWAVE EXCITED DISCHARGE

The microwave irradiation system described in a previous report was used to continue the study of discharges in gases which behave corrosively towards electrodes. The work during this contract period has emphasized work with Mercury Bromide. In addition, some discharges were performed in silane gas mixes and in sulphur.

#### APPARATUS

The apparatus for the microwave experiment is the same as that described in the report "Investigation of Plasma Excitation. Volume II. Microwave Plasmas" (AFWAL-TR-81-2082 Volume II) and in the references therein. For the work described here, a Serpentine gas heater from GTE Sylvania was used to heat the discharge tubes containing volatile material.

The plasma tube was placed inside a larger tube through which the hot air was blown. A thermocouple was attached to the downstream end of the inner plasma tube. It was found that if the discharge tubes were parallel to the microwave applicator, an adjustment of microwave power simply changed the length of the tube in which the discharge took place. Thus, the dependence of visible emission on incident power in some cases merely reflected the change in the volume from which emission took place. To avoid this, the plasma and heating tubes were placed at an angle to the microwave applicator so that the discharge would take place

in the overlap between the plasma tube and the region of high microwave intensity. Nevertheless, it was found that the length of the discharge in the tube did depend on the experimental parameters. For example, Figure 1-1 shows the dependence of the length of discharge on the  $\text{HgBr}_2$  pressure. This, perhaps, is an indication of the dependence of the intensity of microwave radiation needed for sustaining a discharge on gas pressure.

Note that in this and all the data presented here, the term " $\text{HgBr}_2$  pressure" refers to the pressure that would exist in the absence of a discharge, and ignores the possibility that discharge induced dissociation might take place.

#### APPLICATOR TYPES

A number of devices are available for coupling microwave energy into a gaseous plasma.

A summary of types of microwave applicators was prepared and is included in Table 1-1. This list was prepared from the literature references that were readily available and is not a complete list; I am sure that other microwave-plasma coupling devices have been used.

# LENGTH OF DISCHARGE vs. TUBE PRESSURE

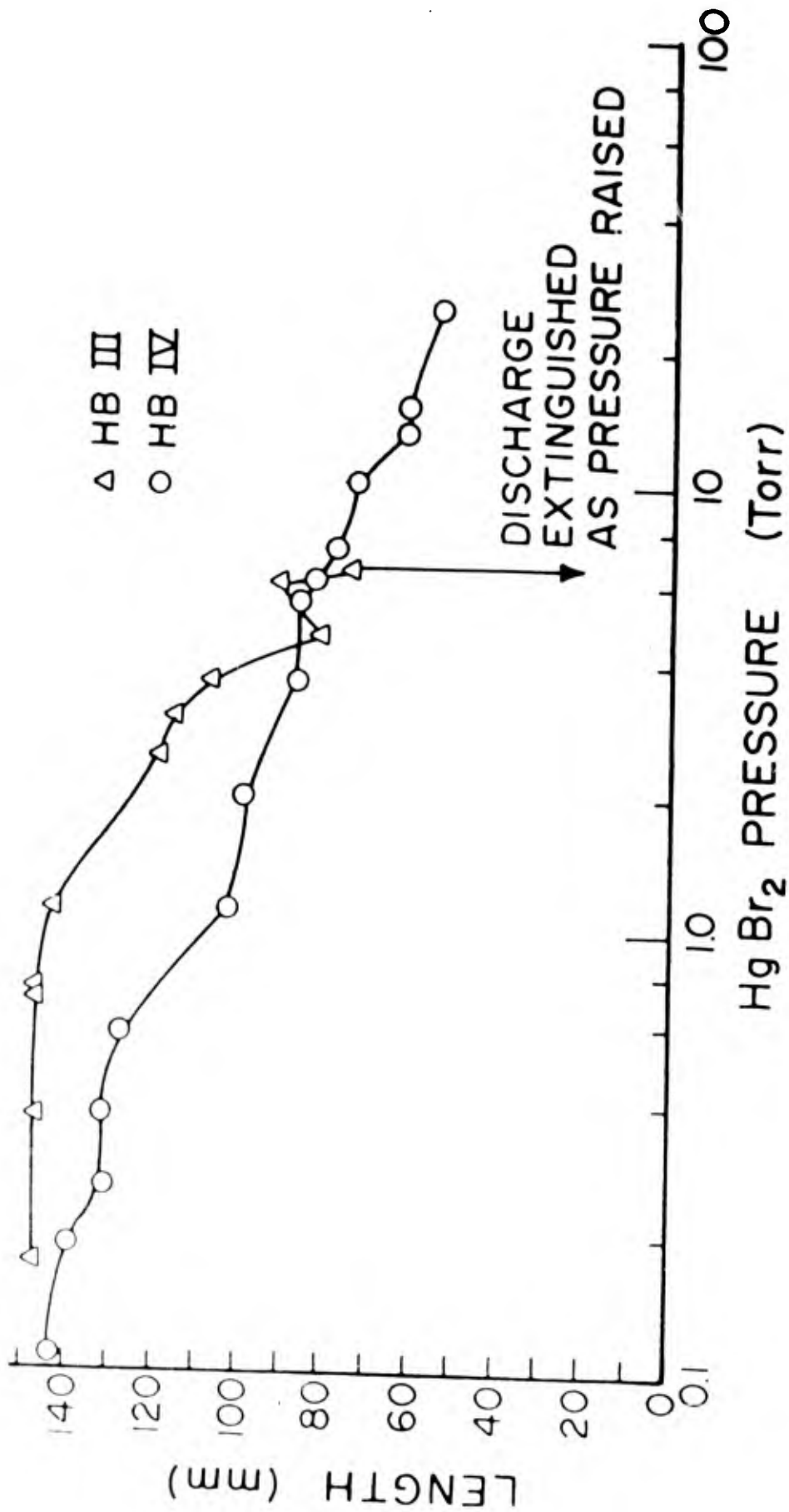


Figure 1-1 LENGTH OF DISCHARGE vs. TUBE PRESSURE

## MICROWAVE - PLASMA - COUPLING - DEVICES

	REFERENCE	POWER (a)	PRESSURE	TUBE DIAMETER
Fusion Systems Applicator	3,4	approx. 1kw	few Torr-few Atm	2-8 mm ID
Gerling-Moore Fringing Field Applicator	1,4	50-1600W	1-200 T	6-10 mm ID
Evenson Cavity	5	125W	10-3 - 760 T	13 mm OD
Asmussen Cavity 1	7	15-25W @ 3.03 Ghz	10-2 - 100 T	6 mm ID
Cavity 2	6,7	200-1000W	5 - 500T	24 mm ID
Bosisio Slow Wave	8	250-2500W	2-600 T N <sub>2</sub> , O <sub>2</sub>	19 mm ID
	10,11	0-2500W	7T SF <sub>6</sub> + He + O <sub>2</sub>	16 mm OD
	14	250-2000W	0.2 - 500 TN <sub>2</sub> ,Ar	19.5 mm ID
Surfatron (b)	9	40W @ 360 Mhz	0.002 - 10 T	25 mm ID
	11,13	0-700W @ 915 Mhz	--	14-25 mm ID
	12	50-700W @ 915 Mhz	1-3 Atm.	6 mm ID
	15	300W @ 915 Mhz	0.04 T Ar	25 mm
Kato Coaxial Line	16,17	240-600W	2-20 T	3.2 - 15 mm ID
Brink Molecular Beam Source	18	--	10-2 - 5 T	12 mm OD

(a) Frequency, if not specified, was 2.45 Ghz.

(b) Surfatron for use at 2.45 Ghz have more recently been built by Moision et al.

REFERENCES AND ADDRESSES FOR TABLE 1-1

1. Thermex Inc. (Formerly Gerling Moore)  
2800 Mead Avenue  
Santa Clara, CA 95051
  
2. Holaday Industries, Inc.  
Hopkins, MN 55343
  
3. Fusion Systems Corp.  
11810 Parklawn Drive  
Rockville, MD 20852
  
4. "Microwave - Discharge Coupling Devices Creating Overdense Plasmas with High Input Power Densities," M. L. Andrews, V. E. Merchant, and J. E. Hopper. Unpublished.
  
5. F. C. Fehsenfeld, R. M. Evenson, and H. P. Broida, "Microwave Discharge Cavities Operating at 2450 Mhz," Rev. Sci Instrum. 36, 294 (1965).
  
6. Jes Asmussen, Jr., R. Mallavarpu, J. R. Hamann, H. C. Park, "The Design of a Microwave Plasma Cavity," Proc IEEE 62, 109 (1974).
  
7. R. Mallavarpu, J. Asmussen, M. C. Hawley, "Behavior of a Microwave Cavity Discharge over a Wide Range of Pressures and Flow Rates," IEEE Trans. on Plasma Science Vol. PS-6 Pg. 341 (1978).

8. R. G. Bosisio, C. F. Weissfloch, M. R. Wertheimer, "The Large Volume Microwave Plasma Generation: A New Tool for Research and Industrial Processing," *M. Microwave Power* Vol 7, Pg. 325 (1972).
9. M. Moisan, C. Beaudry, and P. Leprince, "A Small Microwave Plasma Source for Long Column Production without Magnetic Field," *IEEE Trans. on Plasma Science*, Vol PS-3, Pg. 55 (1975).
10. L. Bertrand, J. M. Gagné, B. Mongeau, B. Lapointe, Y. Conturie, M. Moisan, "A Continuous HF Chemical Laser: Production of Fluorine Atoms by a Microwave Discharge," *J. Appl. Phys.* Vol 43, Pg. 224 (1977).
11. L. Bertrand, J. M. Gagné, R. G. Bosisio, and M. Moison, "Comparison of Two New Microwave Plasma Sources for HF Chemical Laser," *IEEE J. of Quantum Electronics* Vol QE-14, Pg. 8 (1978).
12. M. Moisan, R. Pantel, J. Hubert, E. Ployet, P. Leprince, T. Marec, and A. Ricard, "Production and Applications of Microwave Surface Wave Plasma at Atmospheric Pressure," *J. Microwave Power* Vol 14, Pg. 57 (1979).
13. L. Bertrand, J. P. Monchalin, R. Pitre, M. L. Meyer, J. M. Gagné, and M. Moison, "Design of a Compact cw Chemical HF/DF Laser Using a Microwave Discharge," *Rev. Sci. Instrum.* Vol 50, Pg. 708 (1979).

14. R. G. Bosisio, M. Nachman, T. Spooner, "Power Absorption in High Power Microwave Discharges," IEEE Trans on Plasma Science Vol PS-2, Pg. 273-276 (1974).
15. V. M. M. Glaude, M. Moisan, R. Pantel, P. Leprince and J. Marec, "Axial Electron Density and Wave Power Distributions Along A Plasma Column Sustained by the Propagation of a Surface Microwave," J. Appl. Phys. Vol 51, Pg. 5693 (1981).
16. I. Kato, H. Tsuchida, and M. Nagai, "Radial Distribution of Excited Atoms in a New Coaxial Line Type Microwave cw Discharge Tube," J. Appl. Phys. 51, Pg. 5312 (1980).
17. A variation of the device described in Reference 16 has been used by Dr. Schubel of the Avionics Laboratory of Wright-Patterson Air Force Base.
18. G. O. Brink, R. A. Fluegge, and R. J. Hull, "Microwave Discharge Source for Atomic and Molecular Beam Production," Rev. Sci. Instrum. Vol 39, Pg. 1171 (1968).



## MODELLING OF THE PLASMA LOAD

In these experiments the principal diagnostic measurements were the intensity and spectral distribution of the emitted light and the fractions of the incident power that were reflected from and transmitted through the plasma.

It is not clear to this author how information concerning the plasma properties can be derived from the measured transmitted and reflected power levels. To attempt to rectify this situation, a simple transmission line analog of the microwave applicators was studied. The waveguides connected to a single traveling wave applicator were modeled as transmission lines with a characteristic impedance  $Z_0$ . The applicator and plasma tube were assumed to have a series impedance of  $Z_1$  and an impedance to ground  $Z_2$ . The input power was provided to the applicator down one transmission line; a second line, terminated with its characteristic impedance, carried away the transmitted power.

This is a simplified model for the applicators actually used, in which four waveguides were used. Two waveguides carried power from the cw microwave sources, and two carried power from the pulsed sources. If only one source is being considered, there could be and, in general, was transmitted power down each of the other three waveguides.

With the simplified model of the applicator, the fraction of incident signal reflected and the fraction transmitted through the applicators is given by

$$PR = \frac{Z_e + Z_0}{Z_e + Z_0}$$

and

$$\rho_T = \frac{2(1 + \rho_R) Z_0}{(2 + Z_1/Z_0 + 2Z_2/Z_0) Z_e}$$

respectively, where

$$Z_e = \frac{1}{2}Z_1 + \frac{Z_2 (Z_1 + 2Z_0)}{Z_1 + 2Z_0 + 2Z_2}$$

These coefficients refer to the voltages, not the power, in the transmission lines. The power absorbed by the load is given by

$$f = 1 - (\rho_R)^2 - (\rho_T)^2$$

The reflection and transmission coefficients and the fraction of power absorbed in the load are illustrated in Figures 1-2, 1-3 and 1-4 for various real values of  $Z_1/Z_0$  and  $Z_2/Z_0$ .

Note that:

1. If there is no impedance to ground ( $Z_2 = \infty$ ), a maximum of 50% of the incident energy will be deposited in the load. For the Fusion Systems applicator in which the plasma tube forms the center conductor of a coaxial transmission line, the plasma would be expected to act as a series impedance  $Z_1$ , rather than as an impedance to ground. This analysis implies there will be a maximum of 50% energy deposition into the Fusion System Applicator.
2. For high series impedance ( $Z_1 = 2Z_0$ ) maximum energy deposition occurs for a short to ground ( $Z_2 = 0$ ). However, as  $Z_2$  increases from zero to  $Z_2 = Z_0$ , the power deposition drops by only 10%, which is less than the accuracy of the available power meters.

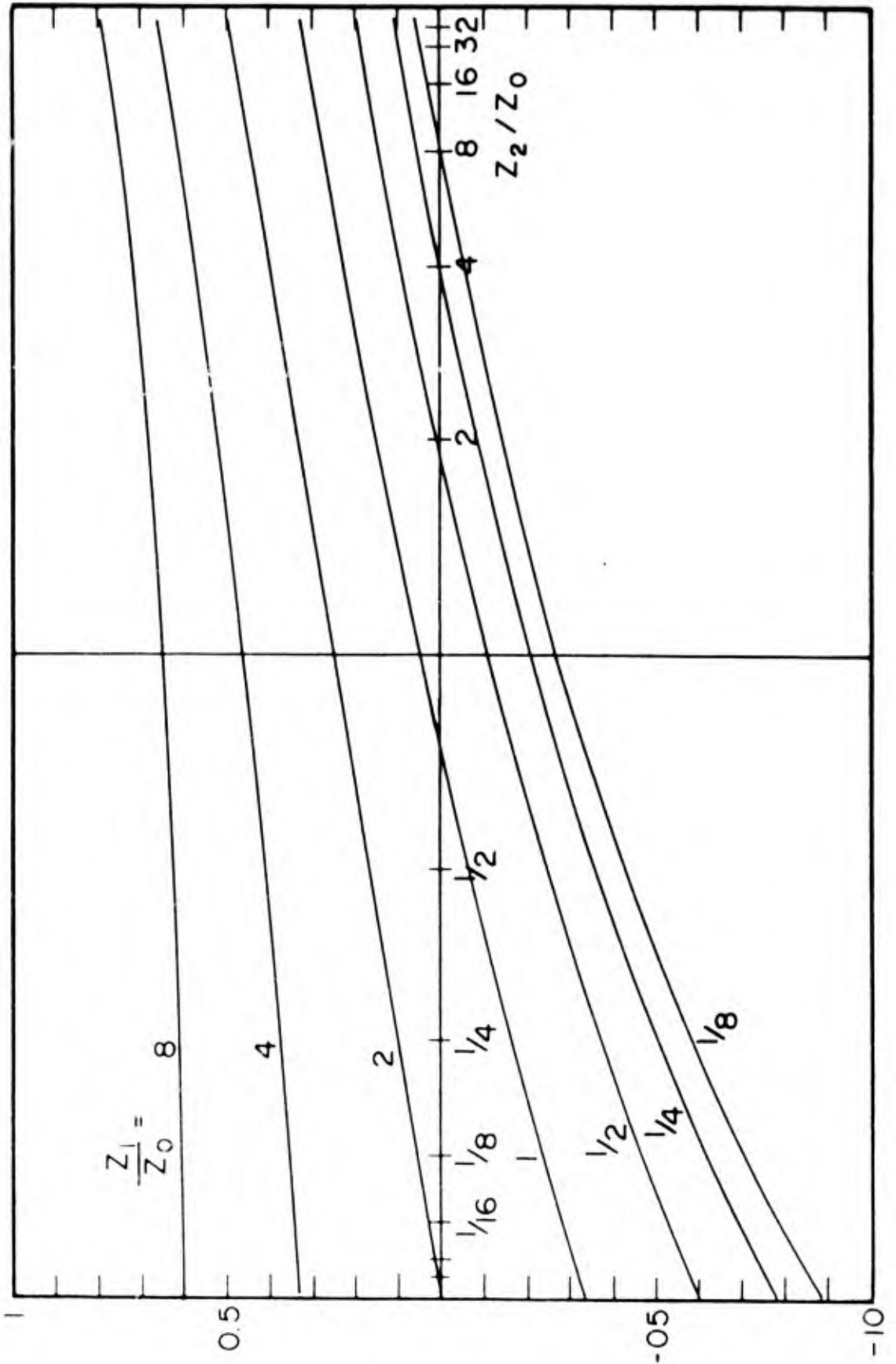
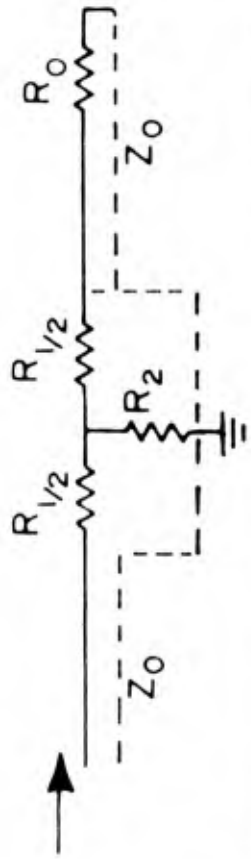


Figure 1-2 REFLECTION COEFFICIENT

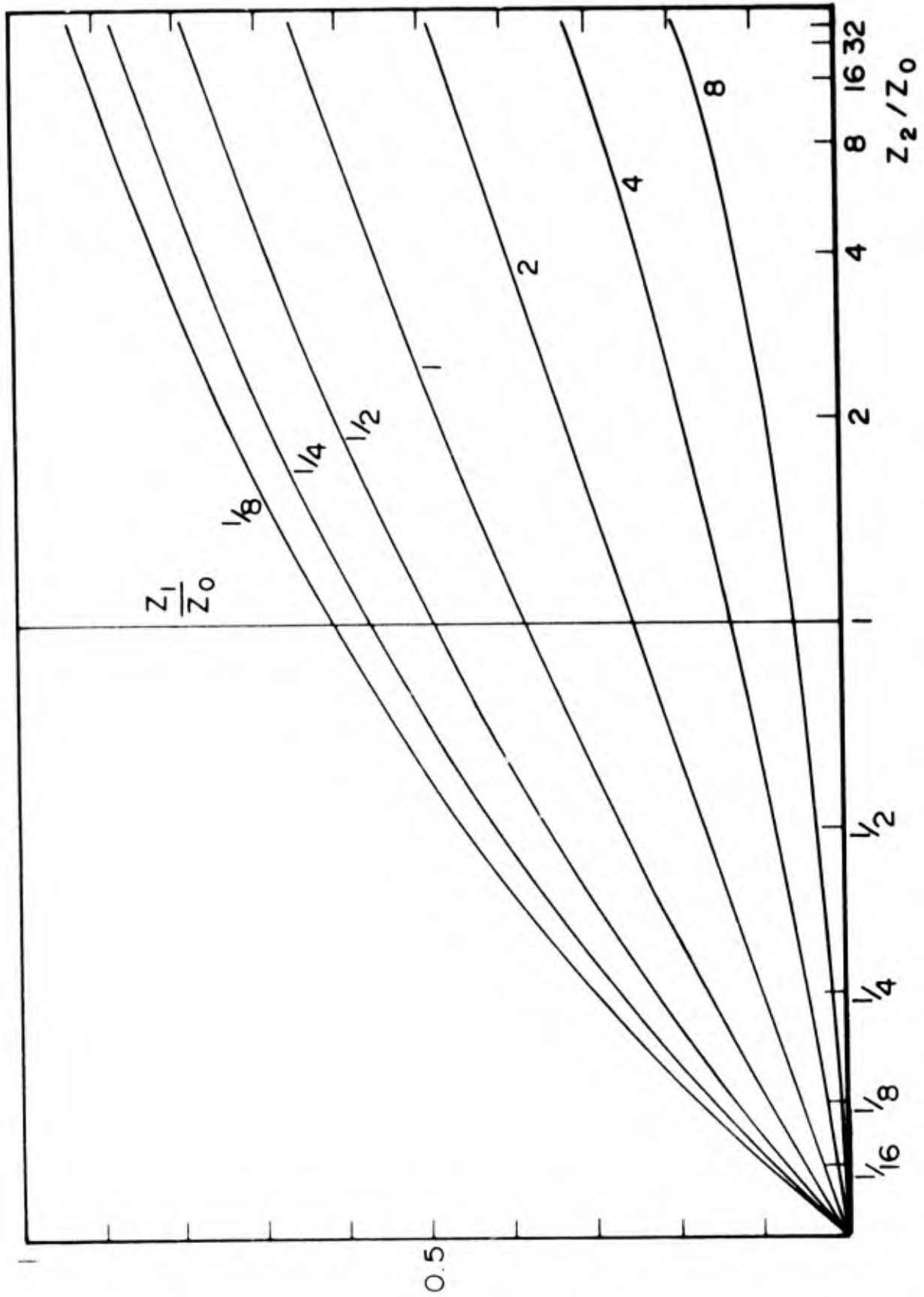


Figure 1-3 TRANSMISSION COEFFICIENT

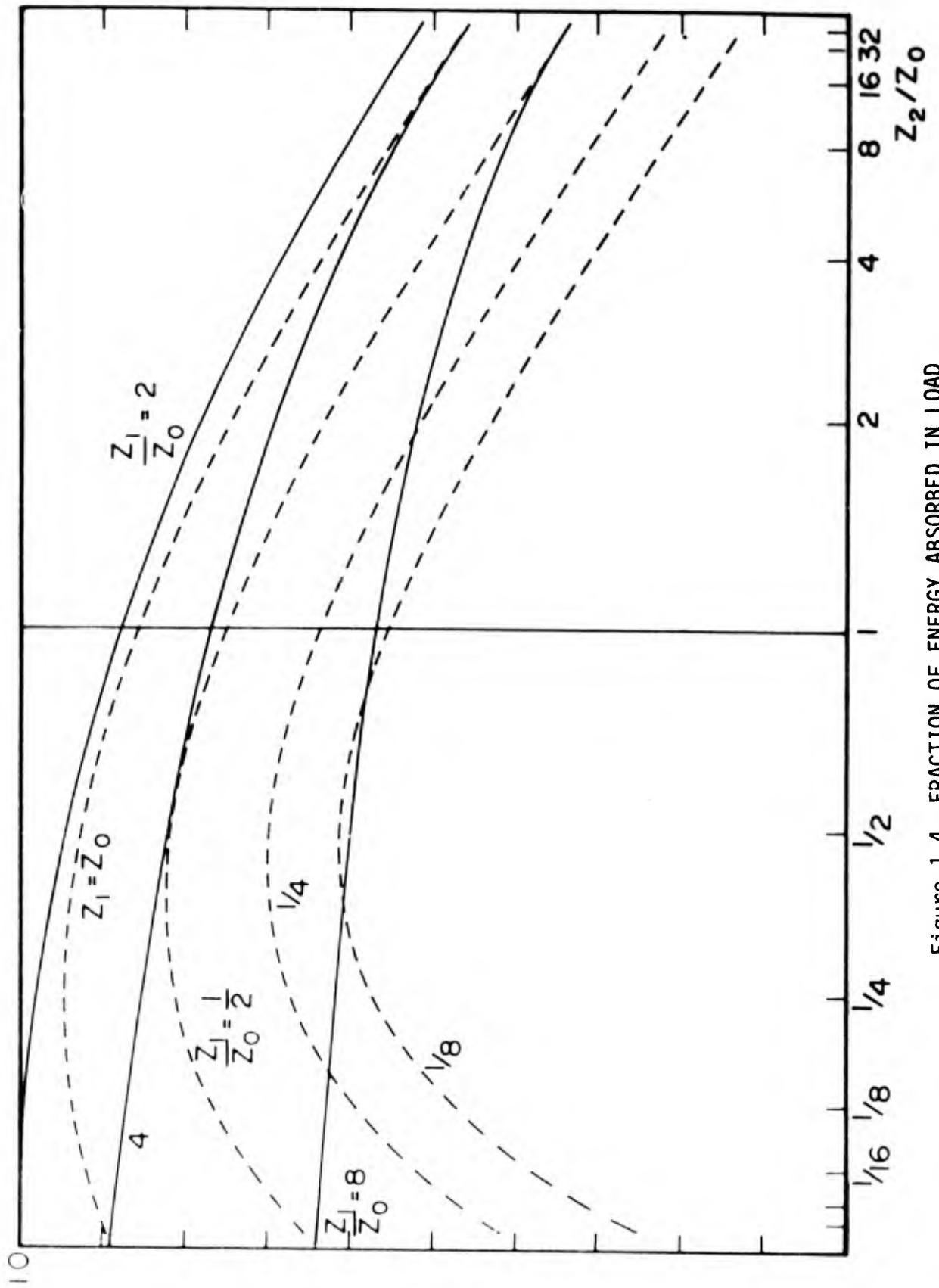


Figure 1-4 FRACTION OF ENERGY ABSORBED IN LOAD

3. For smaller values of the series resistance ( $Z_1 < 2Z_0$ ) the power absorbed by the load has a maximum for a non zero value of  $Z_2$ .

In general, the fraction of the signal that is reflected or transmitted is a slowly varying function of the impedances. This makes it difficult to determine the impedance from measured reflected and transmitted signals. Moreover, it was found experimentally that the reflected and transmitted signals did not vary significantly over a wide range of experimental conditions.

When this calculation was initiated, it was hoped that the measured reflected and transmitted powers could be used to determine a plasma tube impedance and consequently, give some information on the plasma properties.

Because the measured reflectivity and transmittivity were slowly varying functions of experimental parameters, and because the impedance calculated using Figures 1-2 to 1-4 is a slowly varying function of the transmittivity and reflectivity, it was decided that this method of analysis would not provide useful information. This description is included here in the hopes of stimulating discussion which might lead to a more useful method of analysis.

#### MICROWAVE EXCITATION OF A SILANE-ARGON MIXTURE

An investigation was performed of the spectra emitted from a microwave discharge in a silane-argon mixture. The mixture used was 2% silane in argon, which is the standard silane mixture used by the Avionics Branch scientists in encapsulating GaAs substrates. No other gas mixture was studied, and hence, the only experimental parameter was the total gas pressure.

The microwave excitation was a series of 4 kw 2.5 Ghz pulses of width approximately 1 micro sec. and pulse repetition frequency of 1.4 khz. The microwaves were applied to a plasma tube by an interdigital applicator manufactured by Gerling Moore. The plasma tube was made of quartz and was refillable through a stopcock.

Spectra obtained when the discharge tube was filled with 7.5 Torr of the gas mixture showed a structureless continuum extending from 220-350 nm. A number of spectral lines were observable in the region 415-450 nm, in which a variety of SiH and Ar lines occur. These spectral lines were, however, not due to SiH. The hydrogen lines at 656 and 486 nm and strong Argon lines at 697 and 707 nm were observed and identified.

A discharge in 20.1 Torr of the silane-argon mixture showed no hydrogen lines, and the strong argon lines were reduced by a factor of five. The low wavelength continuum was still observed but had superimposed a series of lines extending from 212 to 391 nm. These new lines were positively identified as being due to atomic silicon. In a discharge at 39.3 Torr of the mixture, both the continuum and the silicon atomic lines were reduced in intensity by approximately the same factor. The argon atomic lines at 697 and 707 nm were still observed.

Following this series of measurements, the discharge tube was evacuated to a pressure of  $3 \times 10^{-5}$  Torr and refilled with 7.4 Torr of Argon. A spectra showed not only the known argon lines but also the broad continuum and the lines positively attributed to atomic silicon.

The source of the continuum emission remains unidentified. However, it has been reported by Spanier and MacDiarmid<sup>10</sup> that

efficient conversion of silane into high silanes occurs in an "ozonizer" electrical discharge. Reaction products in the above referenced experiment were 42% disilane, 14% trisilane, 7% high silanes with a vapor pressure at room temperature of 3.2 Torr, solid silicon subhydrides  $\text{SiH}_n$  ( $n=1.2-1.7$ ), and hydrogen.

The experiments described here indicate that a heavy molecular weight silicon hydride compound was formed in the microwave discharge. This material was not readily pumped away and remained in the tube when it was refilled with argon. Bombardment of the walls during the discharge resulted in vaporization of the material, and subsequent excitation resulted in the observed spectral emission from silicon.

No emission from SiH was observed in any of these experiments.

#### MICROWAVE EXCITATION OF MERCURY BROMIDE PLASMAS

Table 1-2 lists the plasma tubes which were available. The discharge tubes were made of fused silica with 8 mm inside diameter, one mm wall, and 20 cm length. They were prepared by placing an amount of mercury bromide powder in the tube, evacuating at room temperature, back filling with a gas or gas mixture, and sealing off. Ultra high purity gases were used, and no emission due to contaminants was observed.

From each tube emission from the HgBr molecule was seen. The spectra of the emission agreed qualitatively with that in Pearse and Gaydon<sup>4</sup> and with that in Wieland.<sup>9</sup>



**TABLE 1-2**  
**TUBE INVENTORY**

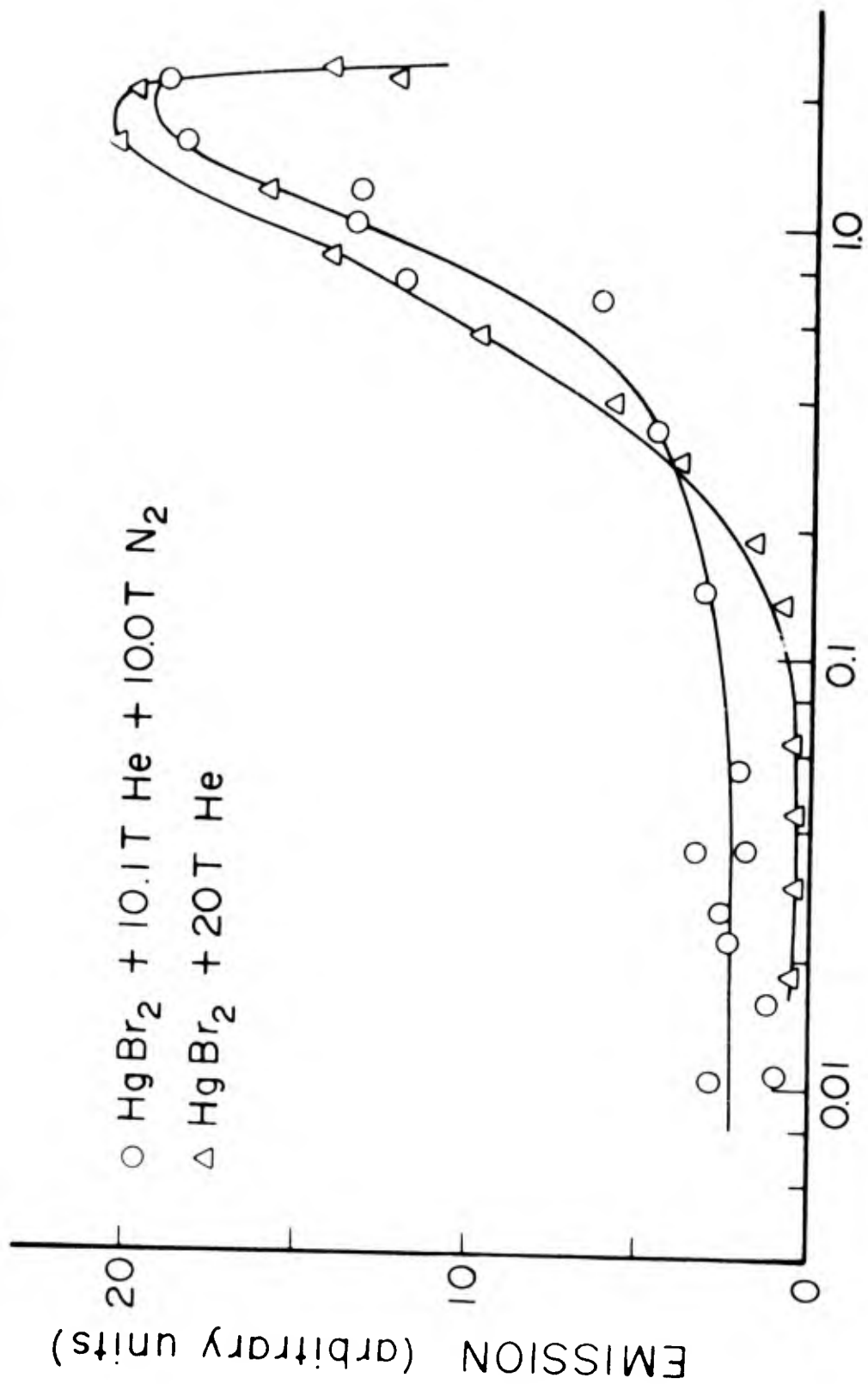
HB I	0.5 mg HgBr <sub>2</sub>	200T He
HB II	1.5 mg HgBr <sub>2</sub> *	10.1T He, 10.0 T N <sub>2</sub>
HB III	excess HgBr <sub>2</sub>	20T He
HB IV	excess HgBr <sub>2</sub>	0.12T He

\* This amount of mercury bromide would be completely vaporized at 180°C, producing a pressure of 11.5 Torr.

For constant incident microwave power, the emission intensity from the HgBr molecule was measured as a function of HgBr<sub>2</sub> pressure. Figure 1-5 compares the emission from tubes HB II and HB III. It is seen that for HgBr<sub>2</sub> pressures greater than 0.2 Torr, the emission from the two tubes is the same within the scatter in the data. However, for pressures less than 0.2 Torr emission from the tube containing N<sub>2</sub> is larger by a factor of four. In Figure 1-6, it is seen that emission from a tube containing 20 Torr of helium is greater than that from a tube containing a low helium pressure. The tube with a low helium pressure would not sustain a discharge with pressures less than 0.19 Torr of HgBr<sub>2</sub>. However, the HgBr emission increased linearly with pressure to the maximum temperature attainable with this experimental configuration.

Emission from discharges in tubes containing 20 Torr of backfill gas increased with increasing pressure, reached a maximum and decreased with a continued increase in pressure. The decrease corresponds to a shrinking of the dimensions of the discharge in the tube. Further increase in pressure would cause the discharge to be extinguished. Note that the position of the HB III tube in the applicator is not the same

# HgBr B-X EMISSION AT 502 nm



HgBr<sub>2</sub> PRESSURE (Torr)

Figure 1-5

# HgBr B-X EMISSION AT 502 nm

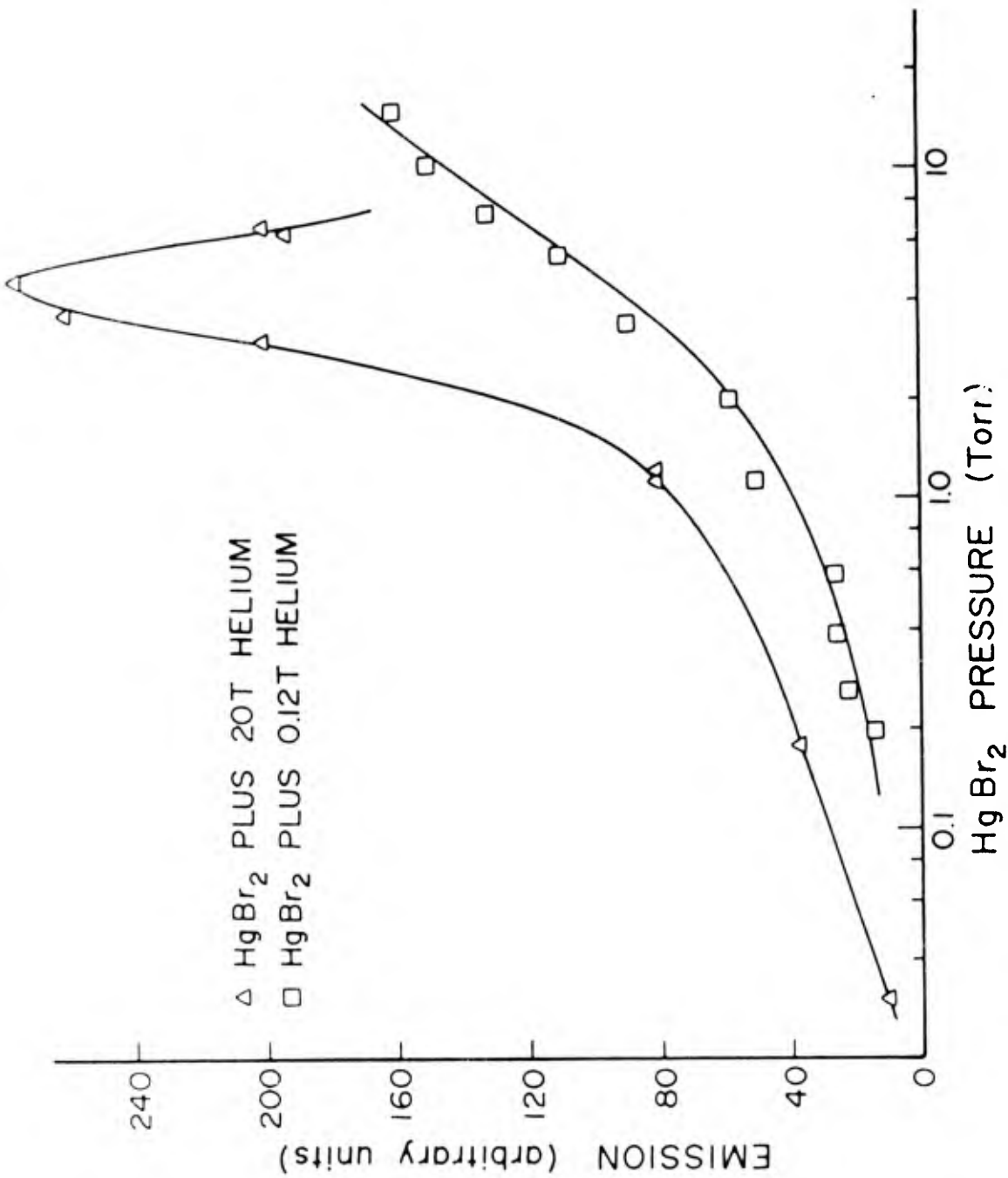


Figure 1-6

for the data presented in Figures 1-5 and 1-6, and hence, the discharge extinguished at a lower pressure in Figure 1-5 than in Figure 1-6.

For the results of Figure 1-6, the plasma was excited by two pulsed microwave supplies, one applied to each end of the applicator. Each pulser was operated at 1.4 khz, but they did not trigger simultaneously. One was triggered from the rise, and the other from the fall of a square wave signal. This increases the effective pulse repetition rate of the pulses applied to the discharge tube. The microwave pulse length was about 1 microsecond.

Emission on the HgBr C-X transitions at 287 nm and on the D-X transition at 256 nm was also observed, but was weaker than that on the B-X transition. The C-X and D-X emission increased approximately linearly with the logarithm of HgBr<sub>2</sub> pressure up to the maximum pressure at which a discharge was observed.

Information can be obtained about the vibrational population distribution of the excited mercury bromide molecules by examining the spectral distribution of the radiation. Emission at 475 nm is primarily due to states with low vibrational excitation ( $V' = 1,2,4$ ); at 500 nm is due to molecules with medium excitation ( $V' = 4$  to 7) and emission at 420 nm is due to highly excited molecules ( $V' = 12$  to 15; Wieland<sup>9</sup>). Emission at the three wavelengths is compared in Figures 1-7 and 1-8 for discharge tubes HB III and HB IV which contain 20 Torr and 0.12 Torr of helium, respectively. For the tube with low helium pressure, it is seen that emission from states with medium and high value of  $V'$  remains approximately constant or perhaps increases slightly as HgBr pressure is raised. Thus, the vibrational temperature is approximately constant.

# DETAILS OF HgBr B-X EMISSION

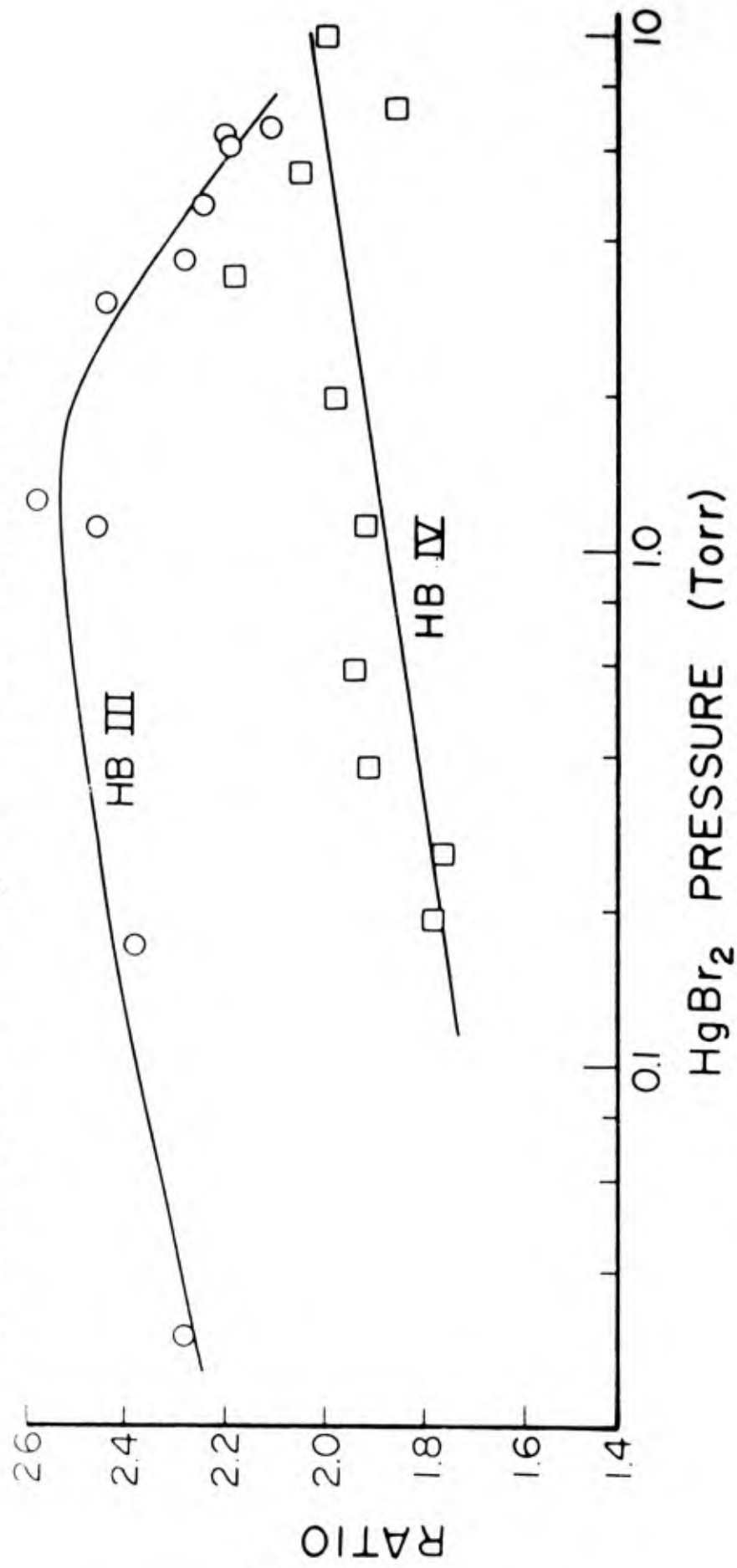


Figure 1-7 DETAILS OF HgBr B-X EMISSION

# DETAILS OF HgBr B-X EMISSION

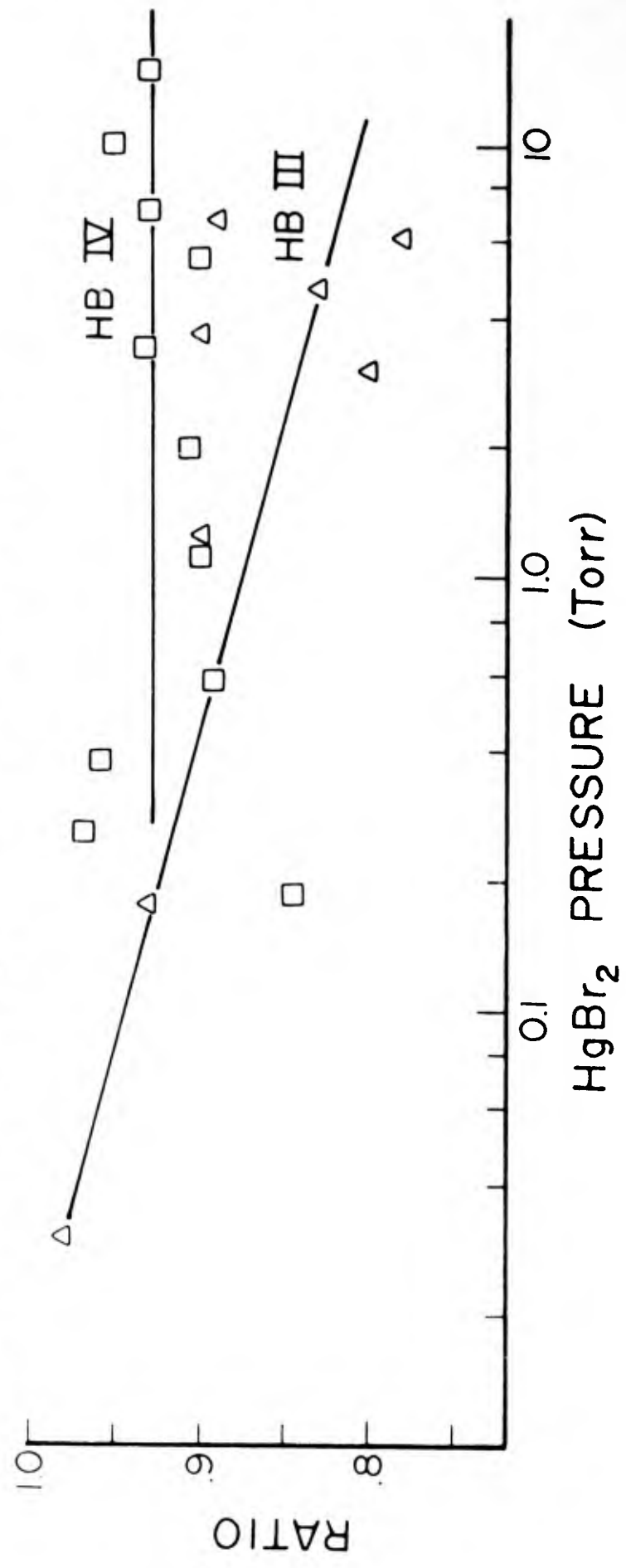


Figure 1-8 DETAILS OF HgBr B-X EMISSION

However, the emission from high excited molecules in the tube containing 20 Torr of helium decreases as pressure increases. The pressure increase causes a decrease in the vibrational temperature of the excited molecules.

Emission was observed from species other than HgBr in these discharges. Figure 1-9 shows the dependence of emission from atomic mercury and from helium on the HgBr<sub>2</sub> pressure. Figure 1-10 shows the dependence of emission from ionic bromine on other HgBr<sub>2</sub> pressure. Atomic bromine has no visible emission lines. The emission from bromine peaks at HgBr<sub>2</sub> pressure of 0.03 Torr and is negligible for pressures greater than 0.5 Torr. Emission from helium decreases monotonically with increasing pressure. The emission from two lines of atomic mercury displays the same pressure dependence. However, emission from the 253 nm line of mercury reaches its maximum value at a lower pressure than does the emission on the other two mercury lines. The 253 nm line is a "resonant" line, terminating on the ground states, and may be subject to self trapping as the temperature, and vapor pressure of any free mercury, is raised. However, there was no evidence of self trapping such as self reversal or broadening of the line profile as pressure is raised. These characteristics are evident in discharge tubes containing mercury alone.

Another possible explanation of the different pressure dependence of the emission on the 253nm mercury line and on other mercury lines is that the mercury emission is absorbed by the HgBr<sub>2</sub> molecules. The measured absorption cross-section is  $4 \times 10^{-18} \text{ cm}^2$  at this wavelength.<sup>2</sup> Note also that HgBr (X, v''=0) has an absorption line at wavelength 253.15 nm,<sup>4</sup> which would have some width due to rotational structure.

VISIBLE EMISSION FROM MICROWAVE  
EXCITED MERCURY BROMIDE-  
HELIUM MIXTURES.

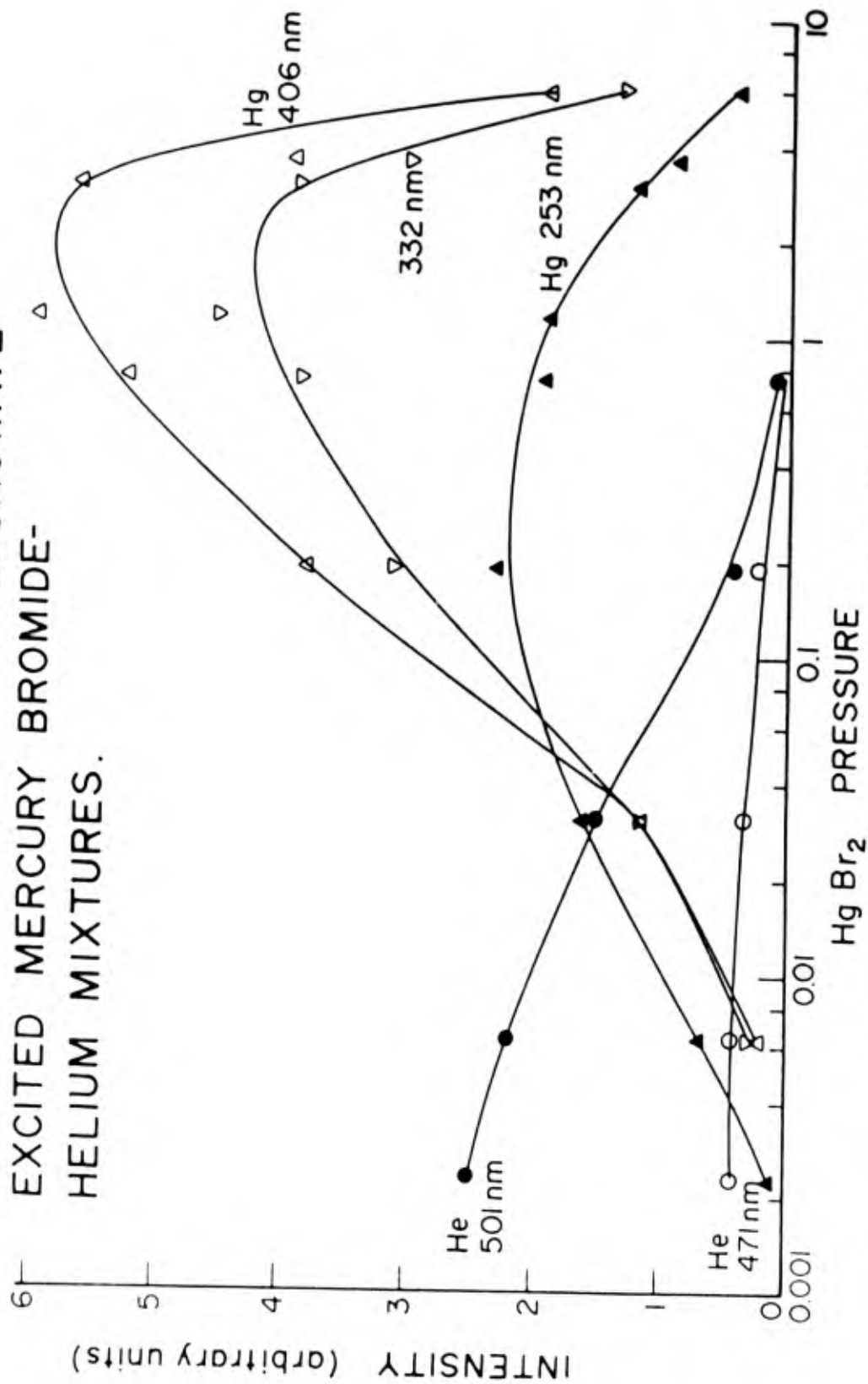


Figure 1-9 VISIBLE EMISSION FROM MICROWAVE EXCITED MERCURY BROMIDE-HELIUM MIXTURES



EMISSION FROM BROMINE IN A  
MICROWAVE EXCITED HgBr<sub>2</sub> PLASMA

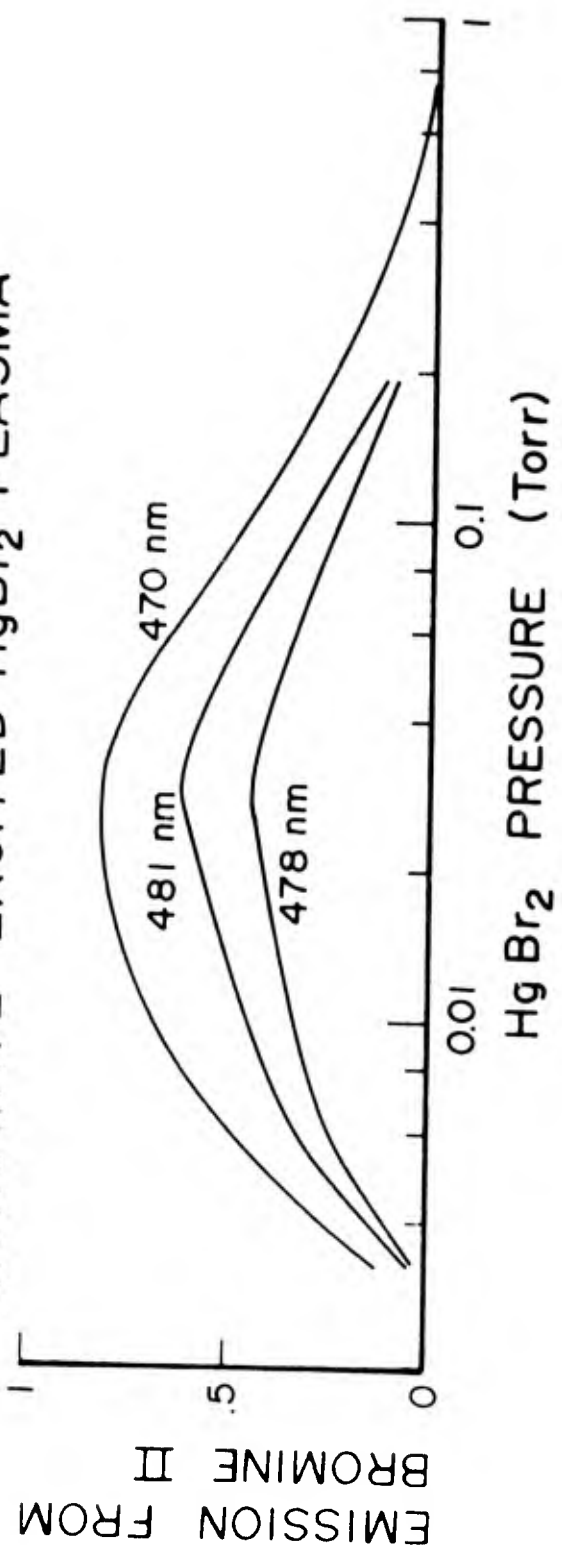


Figure 1-10 EMISSION FROM BROMINE IN A MICROWAVE EXCITED HgBr<sub>2</sub> PLASMA

It is interesting to examine the ratio of emission from atomic mercury to that from molecular  $\text{HgBr}$ . Figure 1-11 presents the dependence of this ratio on tube temperature for three tubes containing a low helium pressure, 20 Torr of helium and the helium-nitrogen mixture. The ratio of atomic to molecular emission reaches its maximum value at a pressure of about 0.1 Torr but is an order of magnitude lower in the tube containing nitrogen than in the tube containing helium at the same pressure. The presence of nitrogen in the discharge appears to deter the complete dissociation of the mercury bromide.

The use of pulsed plus cw power deposition into the plasma increases by a factor of four the relative emission from atomic mercury, as shown in Figure 1-12. This confirms the earlier observations that cw discharges in  $\text{HgBr}_2$  have the character of discharges in mercury with additives.

Note in these graphs, the peak value of a mercury line is used in taking the ratios, and the result that the atomic emission is more intense than the molecular emission is misleading. The spectrally integrated emission from the molecules is far more intense than that from the atomic species, and the discharge tubes give off a vivid blue-green light for  $\text{HgBr}_2$  pressures greater than about 0.1 Torr.

Molecular nitrogen emission was observed from discharges in the tube containing 10 Torr of helium and 10 Torr of nitrogen. Figure 1-13 shows the decay of helium and nitrogen emission as the mercury bromide pressure is raised. The obvious explanation for the decay of the helium emission as the  $\text{HgBr}_2$  pressure is raised is that the presence of a molecule with its cross-sections for electronic vibrational, and

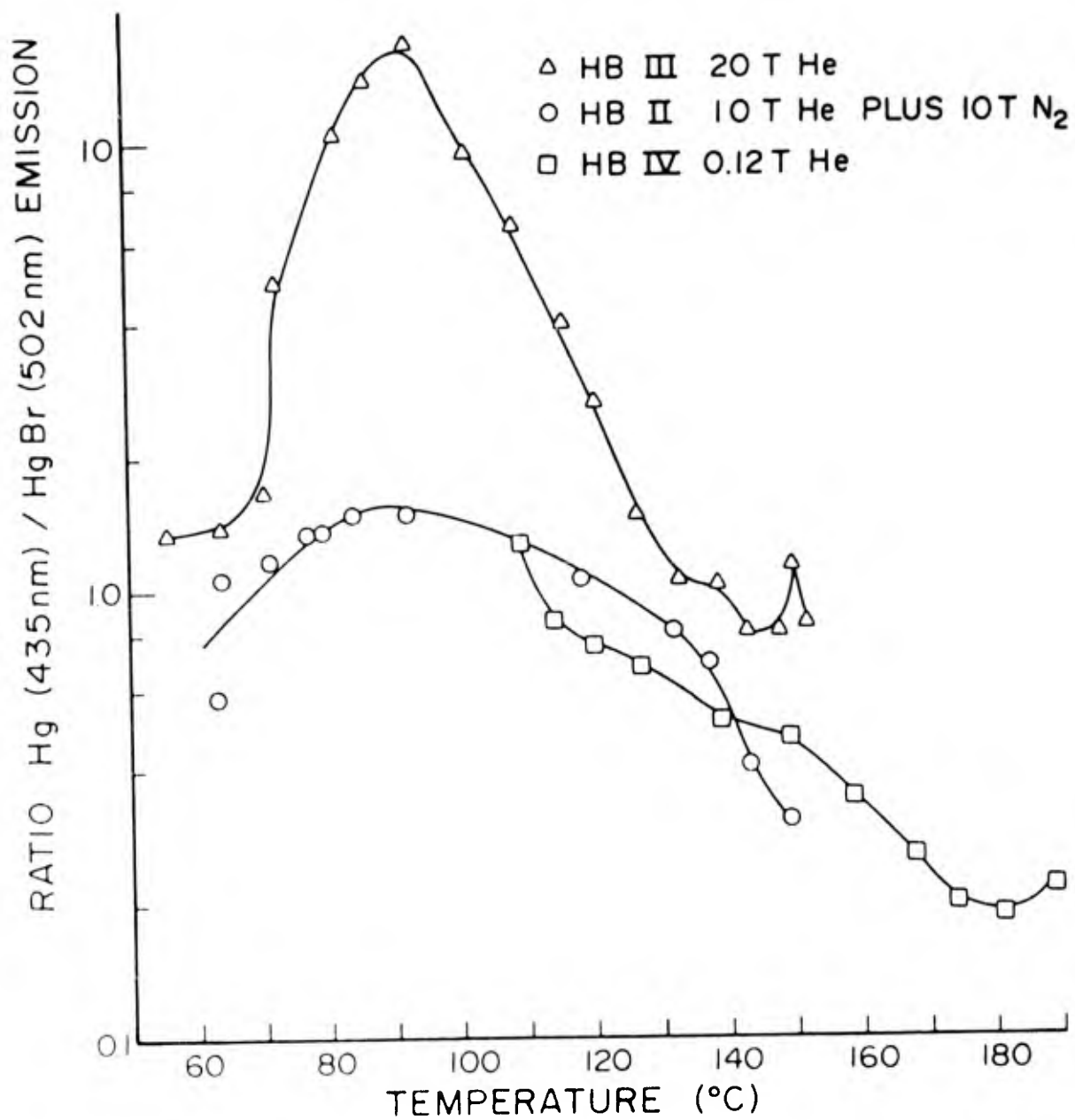


Figure 1-11 EMISSION FROM HgBr<sub>2</sub> DISCHARGE TUBES WITH PULSED MICROWAVE EXCITATION

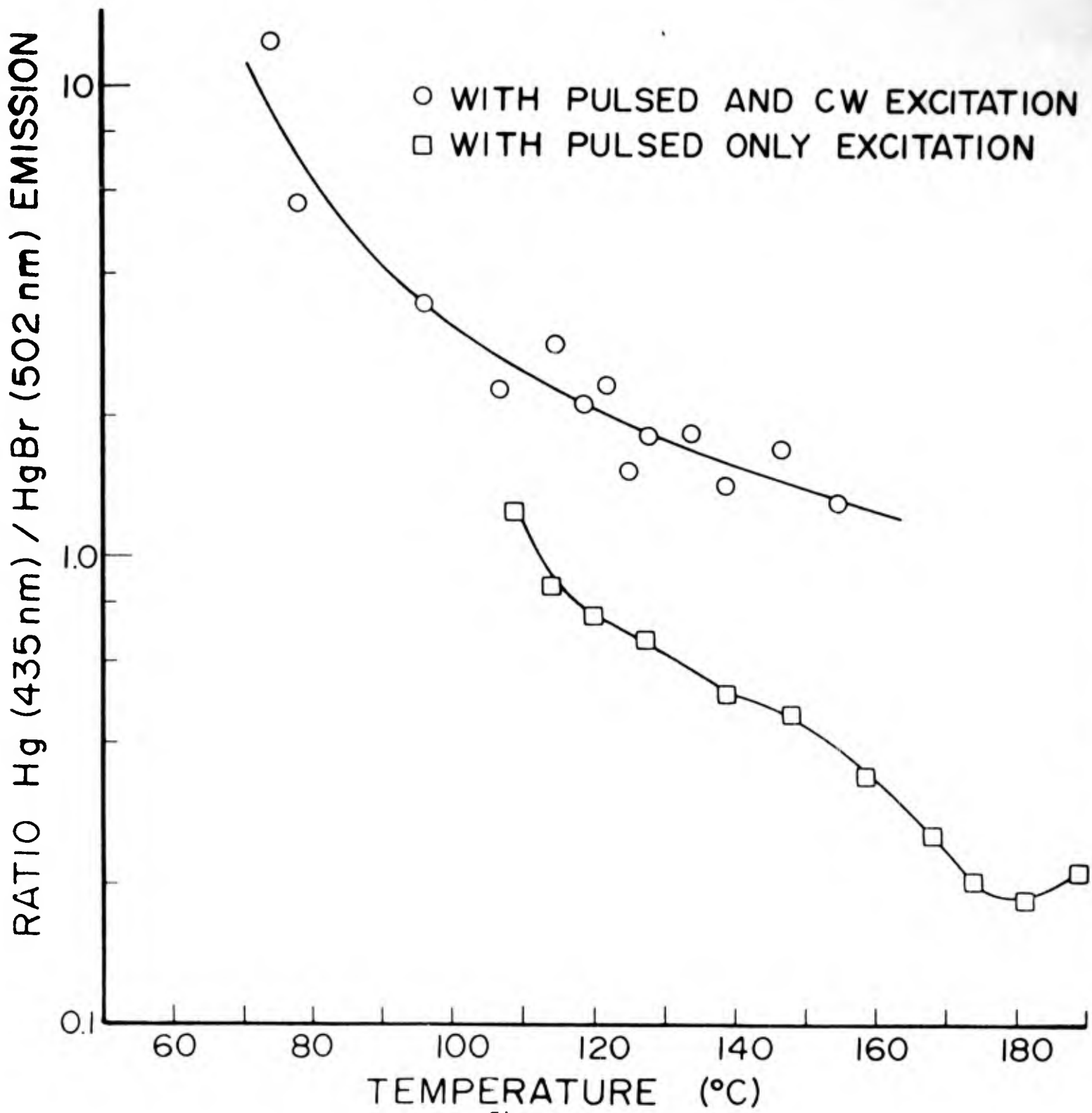


Figure 1-12 EMISSION FROM HgBr<sub>2</sub> DISCHARGE TUBE

# VISIBLE EMISSION FROM MICROWAVE EXCITED MERCURY BROMIDE-NITROGEN-HELIUM MIXTURES.

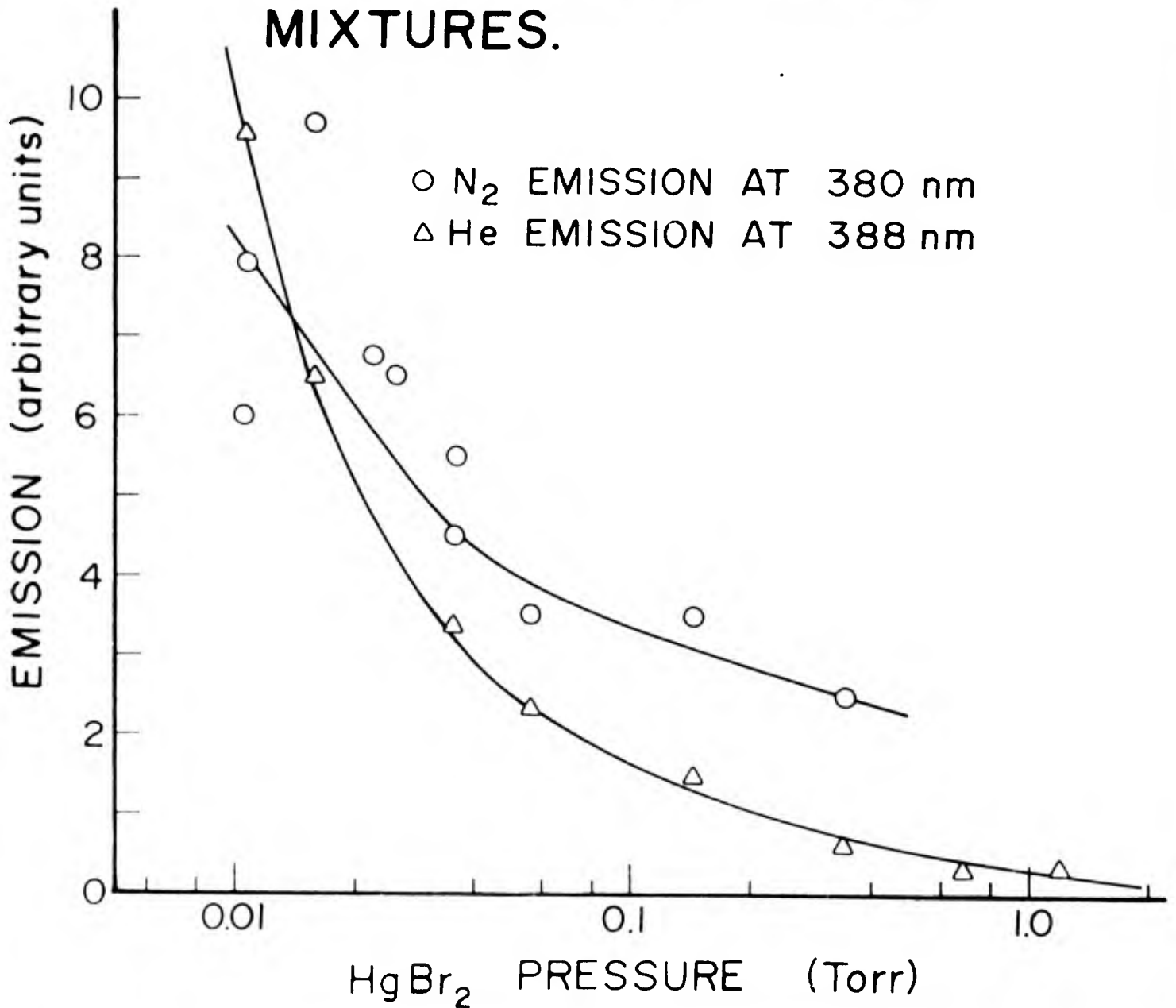


Figure 1-13 VISIBLE EMISSION FROM MICROWAVE EXCITED MERCURY  
BROMIDE-NITROGEN-HELIUM MIXTURES

rotational excitation significantly lowers the electron energy distribution function so that the energetic electrons required to excite the helium become fewer in number. However, if this explanation is valid, it should be noticed that a few tens of milli-torr of  $\text{HgBr}_2$  have a dramatic effect on the helium emission even in the presence of 10 Torr of nitrogen which itself has large cross-sections affecting the electron energy distribution function.

Figure 1-14 shows an electron energy distribution function calculated for Neon/Nitrogen/ $\text{HgBr}_2$  and Neon/Xenon/ $\text{HgBr}_2$  mixtures. In the nitrogen mixture the energy distribution is significantly depleted in the 2-5 eV range within which the  $\text{N}_2$  vibrational cross-sections are very large. As a consequence, a significantly larger E/n value is needed in the nitrogen mixture than in the Xenon mixture to produce the same mean electron energy. Figure 1-15 shows the cross-sections for electronic excitation of nitrogen. The C-A second positive nitrogen emission shown in Figure 1-13 has a threshold energy of about 12 eV. The electron energy distribution function shown in Figure 1-14 shows a significant quantity of electrons with sufficient energy to produce the observed second positive emission.

However, the distribution function of Figure 1-14 was calculated using a mercury bromide excitation cross section as measured by Allison and Zare.<sup>1</sup> This cross-section has recently been remeasured.<sup>7</sup> The new measurements show a threshold at 6 eV, that the cross-section increases rapidly to a value of  $2 \times 10^{-16} \text{ cm}^2$ , and remains approximately constant for higher electron energies. This author

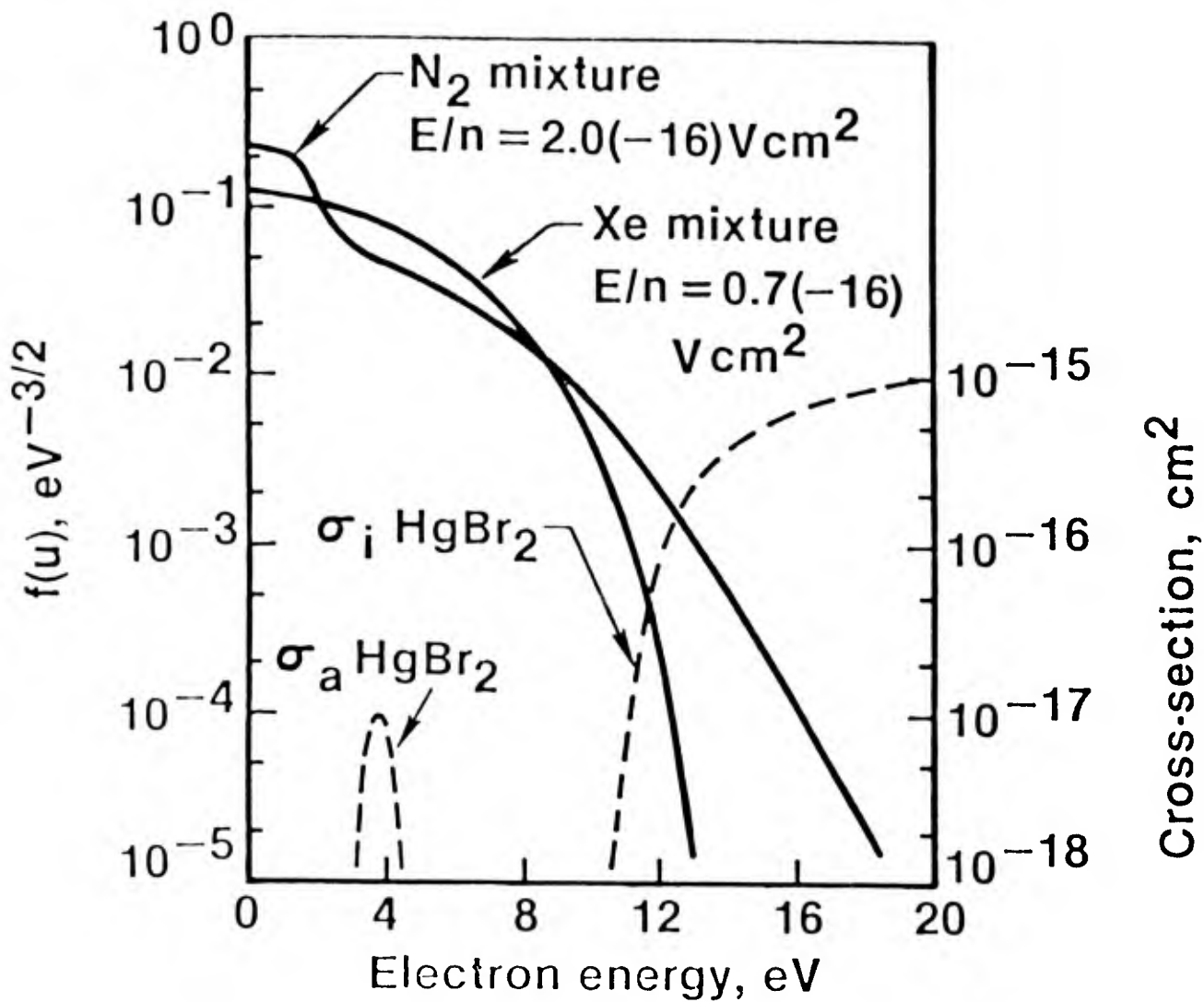


Figure 1-14 Computed electron-energy distributions in Ne-HgBr<sub>2</sub> mixtures containing either 10% N<sub>2</sub> or 10% Xe. Also shown are the cross sections for HgBr<sub>2</sub> dissociative attachment and ionization (from Wiegand and Boedeker, 1982). This figure is from Nighan (1980).

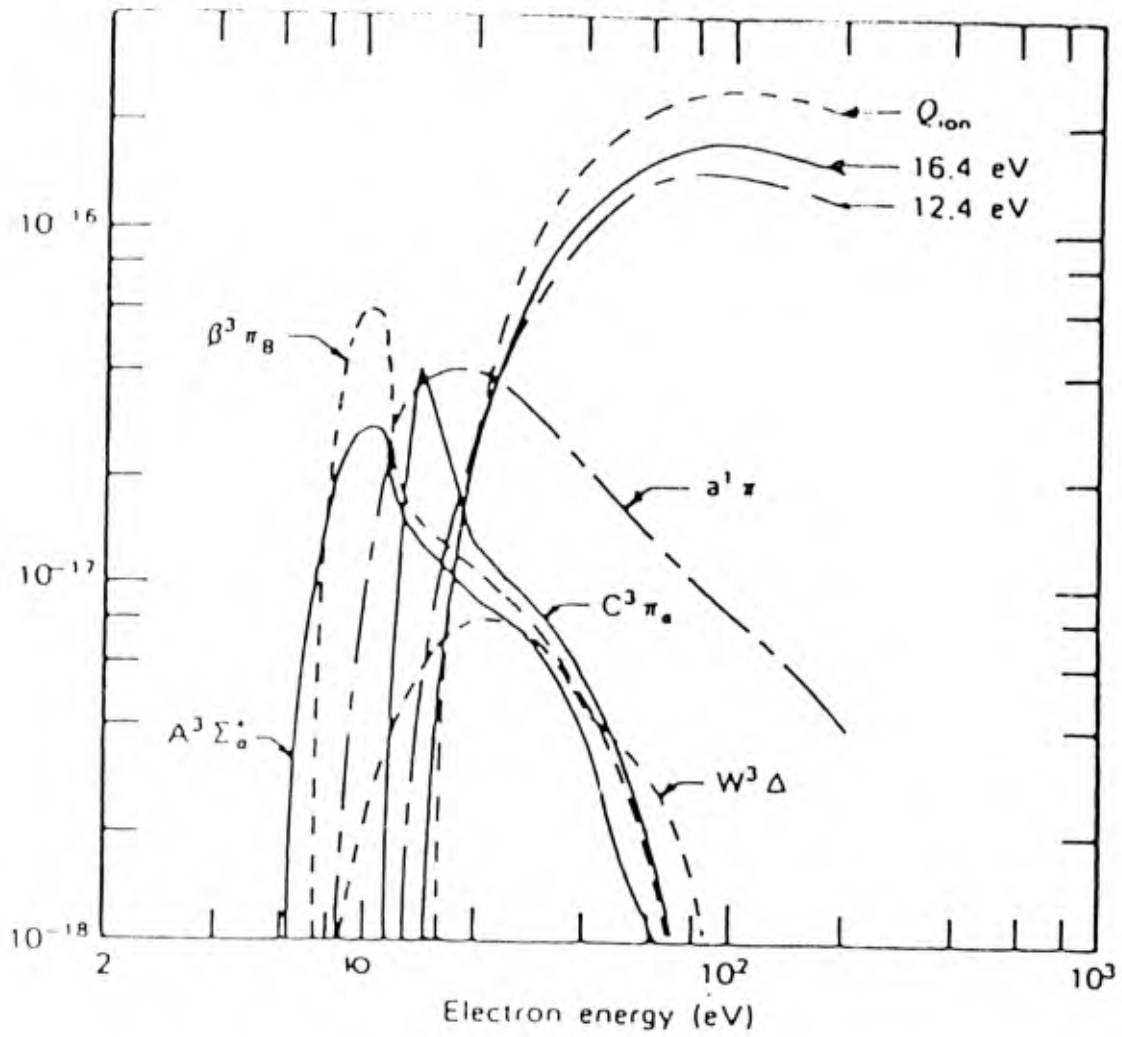


Figure 1-15

Cross-sections in  $\text{cm}^2$  for electronic excitation and ionization of nitrogen (from Rees and Jones (1973) as quoted in Phelps (1979).)

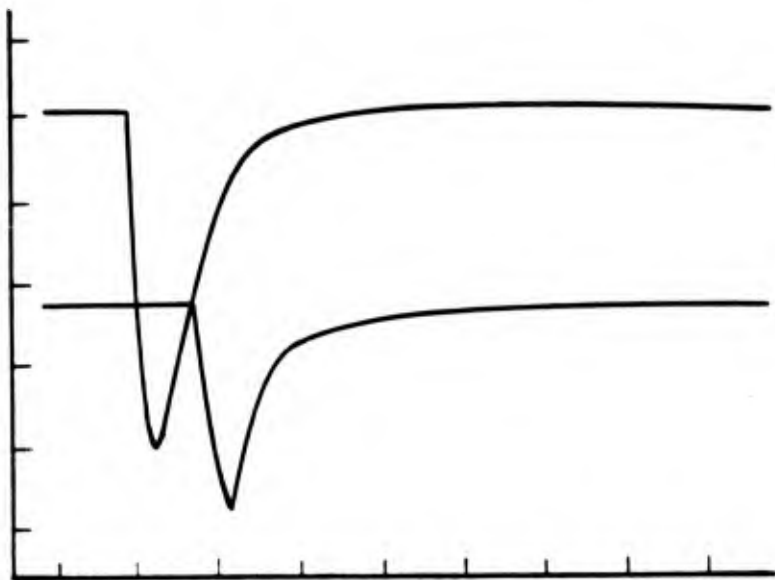


anticipates that the inclusion of this new large cross-section in the calculations of electron energy distribution functions will produce a second step or depletion of electrons at the 6 eV level similar to that produced at 2 eV by the vibrational excitation of nitrogen. The severity of this depletion will, of course, depend on the pressure of mercury bromide in the system.

Thus, the effect of adding mercury bromide is to further reduce the number of high energy electrons. It is these high energy electrons which produce the emission from nitrogen and helium as shown in Figure 1-13. Thus, the decreasing emission is due to the modification of the electron energy distribution function produced by the added  $\text{HgBr}_2$ .

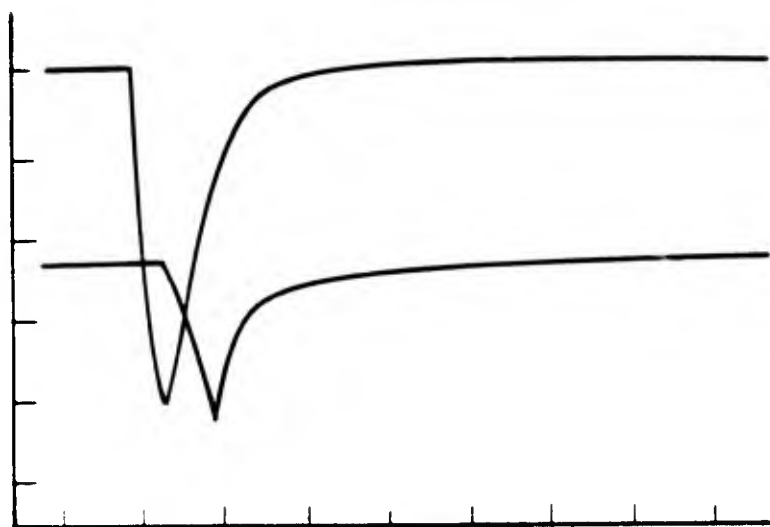
The time dependence of emission on the atomic mercury 253.7 nm line and on the mercury bromide molecular emission is shown in Figure 1-16. For these measurements, the plasma was only excited by pulsed microwaves with the pulse width (FWHM) 400 ns or less. On the oscillographs of Figure 1-16, the response time of the microwave detectors is limited by the cable termination; hence, the duration could be shorter than that shown. The signal from the photomultipliers has a 50  $\Omega$  termination and should have a time response of about 50 ns. Because the use of 50  $\Omega$  termination decreased the signal level from the photomultiplier to measure the time dependence of the HgBr B-X emission, the spectrometer slits were removed making the spectrometer act like a broadband filter of bandpass about 35 nm. Thus, a considerable portion of the molecular emission contributed to the signal shown in Figure 1-16.

The molecular and atomic emission look somewhat similar, but the slight differences are summarized in Table 1-3.



Microwave Pulse

Emission of Hg 253.7nm  
Line



Microwave Pulse

500nm Emission from HgBr

500ns/division

Figure 1.16 TIME RESPONSE OF MERCURY AND MERCURY BROMIDE EMISSION

TABLE 1-3

TIME DEPENDENCE OF EMISSION FROM HB IV

	<u>Delay</u>	<u>Risetime</u>	<u>FWHM</u>
HgBr emission at 500 nm	220 ns	250 ns	300 ns
Hg emission at 253.7 nm	300 ns	300 ns	350 ns

The delay between the microwave pulse and initiation of optical emission cannot be accounted for by the transit time through the photomultiplier, the difference in cable lengths between the two signals, or by triggering characteristics. It is possible that this delay time comes from the breakdown time in the gas; that is, the time it takes the electron density to build up from ambient levels to the density of the fully developed plasma. Further evidence for this comes from examining the transmitted and reflected pulses, which show a sudden drop in the transmitted power after a time delay.

It is interesting, then, that the delay before the appearance of atomic emission is greater than that before molecular emission appears. This is possible if the atomic emission comes not from dissociative excitation of  $\text{HgBr}_2$  excitation, but either from dissociative excitation of HgBr or excitation of Hg. Then the difference in time delay between the atomic and molecular emission is due to the buildup time of the HgBr and Hg populations.

## FIGURE CAPTIONS

- Figure 1-1 Dependence of length of discharge on the  $\text{HgBr}_2$  pressure.
- Figure 1-2 Reflection coefficient for simple model of applicator.
- Figure 1-3 Transmission coefficient for simple model of applicator.
- Figure 1-4 Fraction of power absorbed in applicator in simple model.
- Figure 1-5 Dependence of emission from  $\text{HgBr}$  on  $\text{HgBr}_2$  pressure and effect of gas mixes containing  $\text{N}_2$ .
- Figure 1-6 Dependence of emission from  $\text{HgBr}$  on  $\text{HgBr}_2$  and Helium pressure.
- Figure 1-7 Details of the  $\text{HgBr}$  B-X emission: Dependence of ratio of emission at 500 nm to that at 475 nm on  $\text{HgBr}_2$  pressure.
- Figure 1-8 Details of the  $\text{HgBr}$  B-X emission: Dependence of ratio of emission at 420 nm to that at 475 nm on  $\text{HgBr}_2$  pressure.
- Figure 1-9 Dependence of emission from  $\text{Hg}$  and Helium on the  $\text{HgBr}_2$  pressure.
- Figure 1-10 Dependence of emission from three lines of ionic Bromine on the  $\text{HgBr}_2$  pressure.
- Figure 1-11 Ratio of emission from atomic mercury to that from mercury bromide. Dependence on temperature of discharge tube.
- Figure 1-12 Ratio of emission from atomic mercury to that from mercury bromide. Dependence on mode of excitation.
- Figure 1-13 Dependence of emission from helium and from nitrogen and  $\text{HgBr}_2$  pressure in a discharge tube containing  $\text{He}$ ,  $\text{N}_2$ , and  $\text{HgBr}_2$ .
- Figure 1-14 Electron energy distribution functions.
- Figure 1-15 Electronic excitation cross-sections of nitrogen.
- Figure 1-16 Time dependence of emission from mercury bromide and from mercury.

## REFERENCES

1. Allison, J., and Zare, R. N., 1978, *Chemical Physics* 35, 263.
2. Frampton, G., 1970, M. Sc. Thesis, Air Force Institute of Technology, Wright-Patterson AFB, OH.
3. Nighan, W. L., "Investigation of Plasma Processes in Electronic Transition Lasers," Technical Report TR80-922617-5.
4. Pearse, R. W. B., and Gaydon, A. G., 1976, "The Identification of Molecular Spectra," 4th Edition, John Wiley, New York.
5. Phelps, A. V., 1979, Chapter 3 of "Electron Molecule Scattering," Ed. by S. C. Brown, John Wiley, New York.
6. Rees, M. H. and Jones, R. A., 1973, *Planet Space Sci.* 21, 1213.
7. Twist, J. R., 1983, Private Communication.
8. Wiegand, W. J. and Boedeker, L. R., 1982, *Applied Physics Letters* 40, 225.
9. Wieland, K., 1960, *A. Electrochem* 64, 741.
10. Spanier, E. I., MacDiarmid, A. G., *Inorganic Chemistry* 1, 432 (1962).

SECTION 2  
PULSED DISCHARGE SYSTEM  
TESLA

INTRODUCTION AND METHOD

GAS MIXTURES FOR OPENING SWITCHES

An investigation was performed of pulsed electric discharges in an argon-nitrogen mixture. This mixture has a high electron drift velocity and is potentially useful as the medium of an electron beam controlled opening switch.

An analysis of the time dependence of the current and voltage of the pulsed discharges yielded a value for the effective recombination coefficient of the excited gas.

For many applications involving energy transfer, it is desirable to use inductive energy storage. This would increase the stored energy density as measured in energy per unit volume or energy per unit mass of the storage medium over that available with capacitive energy storage that is commonly used at the current time. Capacitive energy storage requires an opening switch. The switch should be closed while the capacitors are being charged, then open to switch the energy stored in the capacitor into a load.

Inductive energy storage, on the other hand, requires a closing switch. The switch is opened to allow current to flow into the inductor. When the energy stored in the inductor  $\frac{1}{2} Li^2$  has reached its desired value, the switch is opened preventing further current flow.

As the current ceases, the inductor can develop very large voltages  $L \frac{di}{dt}$  to try and force the current to stay constant. This voltage will cause breakdown of a load that is in parallel with the inductor, with subsequent deposition of the energy stored in the inductor into the load.

No opening switch exists at the current time with the desired specifications. These include a fast opening time to generate substantial voltages, and a high voltage holdoff capability in the open state. The switch should be capable of high repetition rate operation, which implies a low voltage drop across the switch in the open condition. It is the failure of existing switches to meet these specifications which has prevented the utilization of inductive energy storage to the present time.

Recently an electron beam controlled discharge has been proposed as a candidate for a closing switch with the desired characteristics. In this case, a switch is turned on by irradiating an interelectrode spacing by high energy electrons. The gap operates as a switch controlled by the electron beam ionization since all electrons in the gap are created by the external source. The field due to the voltage across the electrodes is too low for electrons to be created by avalanching processes. Thus, current is conducted across the gap as long as the external source of ionization is on. When the electron beam is turned off, the electrons are lost due to attachment or recombination, and current flow ceases.

For this procedure to result in a successful switch, a number of requirements must be met. The gap spacing and gas pressure must be chosen so that self-breakdown of the gas does not occur. A gas or gas

mixture must be chosen that gives adequate secondary ionization upon irradiation by high energy electrons. The gas mixture must have a sufficiently low voltage drop that at a current density level high enough to be interesting, the power deposition into the switch is a small fraction of the power being switched. This requirement is satisfied if there is a high electron drift velocity in the chosen gas mixture. The gas mixture must have an attachment coefficient low enough that there is no appreciable loss of electrons during the on period of the switch, but high enough to capture the free electrons and turn off the switch after the controlling electron beam ceases. These seemingly contradictory requirements may be achieved by the addition of a gas with an attachment cross-section that is negligible at low electron energies but becomes much larger at higher electron energies. Candidate gases have been investigated by Christophorou et al.<sup>4</sup>

The requirement of a high electron drift velocity is satisfied by the use of a mixture of a molecular gas and a gas with a Ramsauer minimum. The Ramsauer minimum is a phenomenon observed in, for example, argon and xenon in which the electron-atom momentum transfer cross section becomes very small for a particular value of electron energy. This is, for electrons of that particular energy, the pure gas is essentially transparent. Under the influence of an electric field, however, the electron will gain energy until the momentum transfer cross section becomes appreciable. Then, the electron will be involved in an elastic collision, and lose a small amount of energy.

If a molecular gas is added to the Ramsauer gas, and has a collision cross section for vibrational excitation with an energy



threshold slightly greater than the Ramsauer minimum, then the electron will have an inelastic collision and lose a significant amount of energy. Thus, the electron is confined to the region in energy space near the Ramsauer minimum for which the gas is nearly transparent. The electrons, although travelling slower, experience fewer momentum changing collisions. They, therefore, travel further in the direction of the field and the ensemble of electrons has a high drift velocity.<sup>8</sup>

The predictions of high electron drift velocities have been confirmed by swarm experiments. The purpose of the experiments described herein is to investigate pulsed discharges in a gas mixture with a high electron drift velocity that is useful in an electron beam controlled opening switch.

These pulsed discharges were initiated in a chamber built to ultra high vacuum standards and described in detail in the next section. The discharge was preionized by ultra violet emissions from a sliding spark discharge which was<sup>2,19</sup> triggered a short interval before the main discharge. Accurate current and voltage versus time wave forms for the main discharge were recorded.

#### ANALYSIS OF PULSED DISCHARGES

The voltage and current across the gap are time dependent quantities that can be predicted by the spatio temporal solution of the electron and positive ion continuity equation coupled with Poisson's equation and an equation relating the external circuit parameters.<sup>12</sup> A simpler treatment of the pulsed discharge formation ignores the spatial variation of electron and positive ion densities and of the electric field. The simplified model can be used to calculate the current growth

when the discharge formative time is comparable to, or much shorter than, the electron transit time.<sup>14</sup> However, the discharge formative time is determined primarily by the characteristics of the external circuit.

One purpose of the experiments reported here is a measurement of the voltage drop in the cathode fall region in which significant spatial variation of the charged particle densities occur. Subtracting this voltage drop from the measured voltage drop across the entire gap, and neglecting a possible small voltage drop in the anode fall region, results in a value of the voltage across the positive column region of the discharge. In the region, spatial variation of the charged particle densities and of the electric field is insignificant, and the simplified theoretical description is applicable.

In this treatment the time development of the electron density is given by:

$$\frac{\partial N_e}{\partial t} = (\alpha - a) W N_e - \gamma N_e N_p + d N_n. \quad (2-1)$$

Here  $N_e$ ,  $N_n$  and  $N_p$  electron, negative, and positive ion densities, and  $\alpha$ ,  $a$ , and  $\gamma$  are the electron ionization, attachment, and recombination coefficients;  $d$  is the detachment rate, and  $W$  is the electron drift velocity. These parameters are functions of the electric field. The term on the right hand side of the equation which describes electron motion  $-\frac{\partial (N_e W)}{\partial x}$ , makes a contribution only in regions of significant spatial variation and has, therefore, been neglected. Charge neutrality  $N_p = N + N_n$  is a consequence of Poisson's equation and neglect of spatial variations.

The pulsed discharge experiments here were in a nitrogen argon gas mixture. Neither of these two gases is a strong attacher of electrons, and electron loss is predominately due to recombination, as discussed later. Hence,  $N_n = 0$  and  $N = N_p$ .

#### ION KINETICS IN ARGON-NITROGEN MIXTURE

Apart from the initial photo-ionization, ions are produced by electron impact ionization of nitrogen and argon. This produces  $N^+$ ,  $N_2$ ,  $Ar^+$  and also excited argon ions. In addition, metastable argon and nitrogen are produced by electron impact, and can be ionized by a second electron collision or by a collision between two metastable species; for example:



The reactions between metastable species are summarized in detail by Hill.<sup>10</sup> The initially produced ions can react with neutrals transferring the charge or possibly producing an ion cluster. The main ion reactions are summarized in Table 1-1, neglecting multiply ionized species. Other recombination channels not listed are possible, but data is not available. The calculation of reaction times assumes an  $N_2$ :  
Ar = 10:90 mixture at atmospheric pressure, that a majority of species are in the ground state and that argon is as effective as helium in promoting reactions (3) and (5).

The ion kinetics in argon-nitrogen mixtures have not been previously investigated. In pure nitrogen, recombination times have been measured by Douglas-Hamilton<sup>5</sup> and by Meyer et al.<sup>18</sup> See also McDaniel et al.<sup>17</sup> pg. 1469. For values of E/N greater than 6 Td,

Meyer et al. have measured  $\gamma = 5.5 \times 10^{-8} \text{ cm}^3/\text{s}$ , while Douglas-Hamilton has measured  $\gamma = 8 \times 10^{-8} \text{ cm}^3/\text{s}$ . The recombination coefficient increases as E/N decreases, reaching a value  $\gamma = 8 \times 10^{-6} \text{ cm}^3/\text{s}$  for E/N = 0 (cf. McDaniel Report).

There is no data available for attachment to N, N<sub>2</sub> or Ar. The attachment coefficient can safely be considered to be zero, in the absence of impurities.

### EXPERIMENTAL APPARATUS

The vacuum system consists of a 50 liter stainless container approximately 20 cm in diameter and 120 cm in length. Four pyrex windows on Varian 4.5 inch conflat<sup>tm</sup> flanges are installed along the length of the cell at about 25 cm intervals. Ten inch conflat<sup>tm</sup> flanges on both ends of the cell also are fitted with pyrex windows. The test cell can be isolated from the pumping manifold by a gold sealed Varian valve. The system can be pumped to  $1 \times 10^{-7}$  Torr by the oil diffusion pump and the entire system is bakeable to 200 C. Figure 2-1 shows a schematic diagram of the vacuum system and the vacuum pump system. Appendix A outlines the procedure for operation of the TESLA vacuum system and discharge electronics.

The gas manifold illustrated in Figure 2-2 has been designed and constructed to allow gas mixtures to be repeatedly and accurately backfilled into the vacuum chamber. A number of constraints were followed in the construction of the design of the gas input system. The system is compatible with ultra high vacuum standards and is bakeable to 200 C. A gas sample bottle can be attached to the system and will

# TESLA

## VACUUM SYSTEM

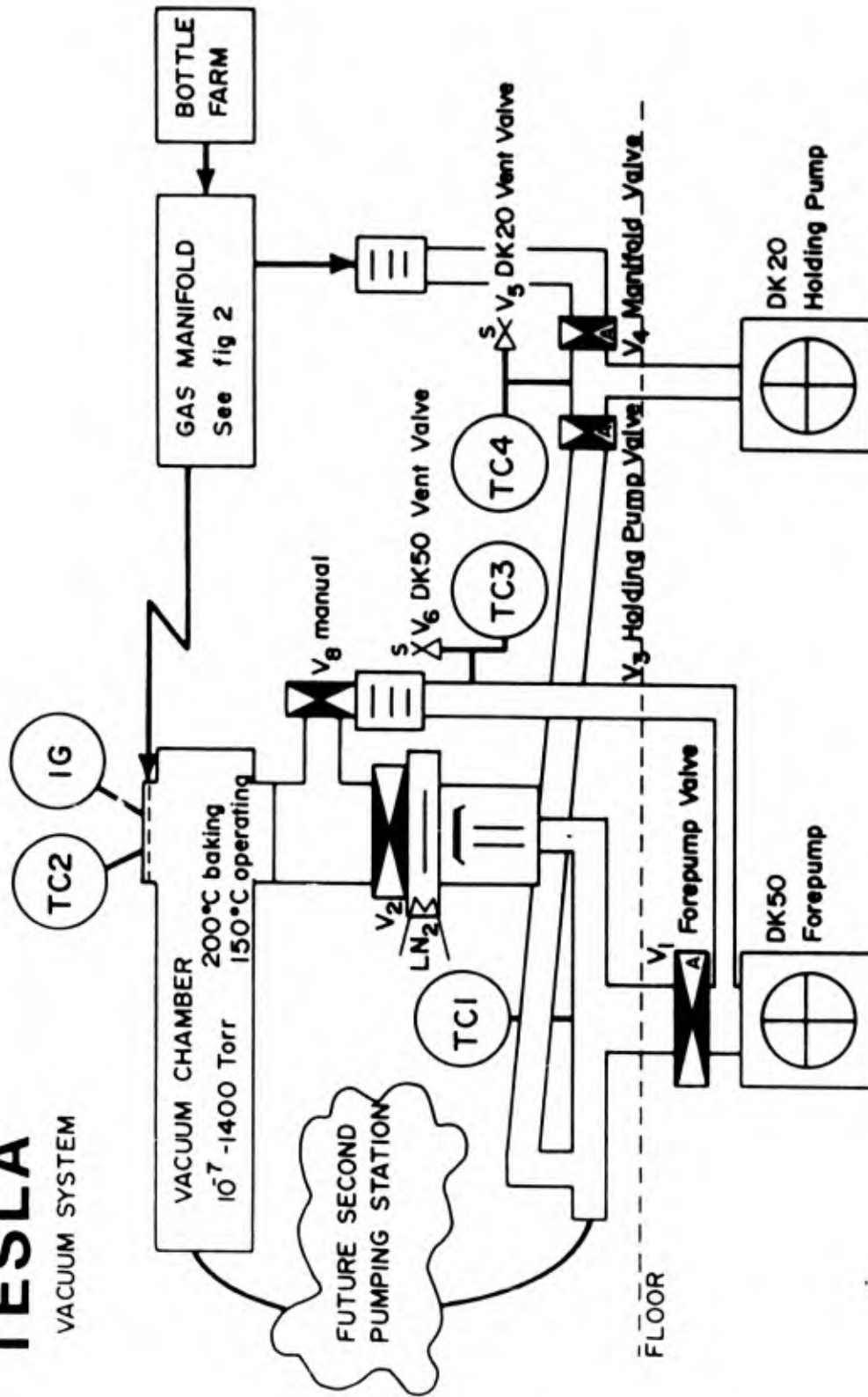


Figure 2-1 TESLA VACUUM SYSTEM

# TESLA gas manifold mixing system

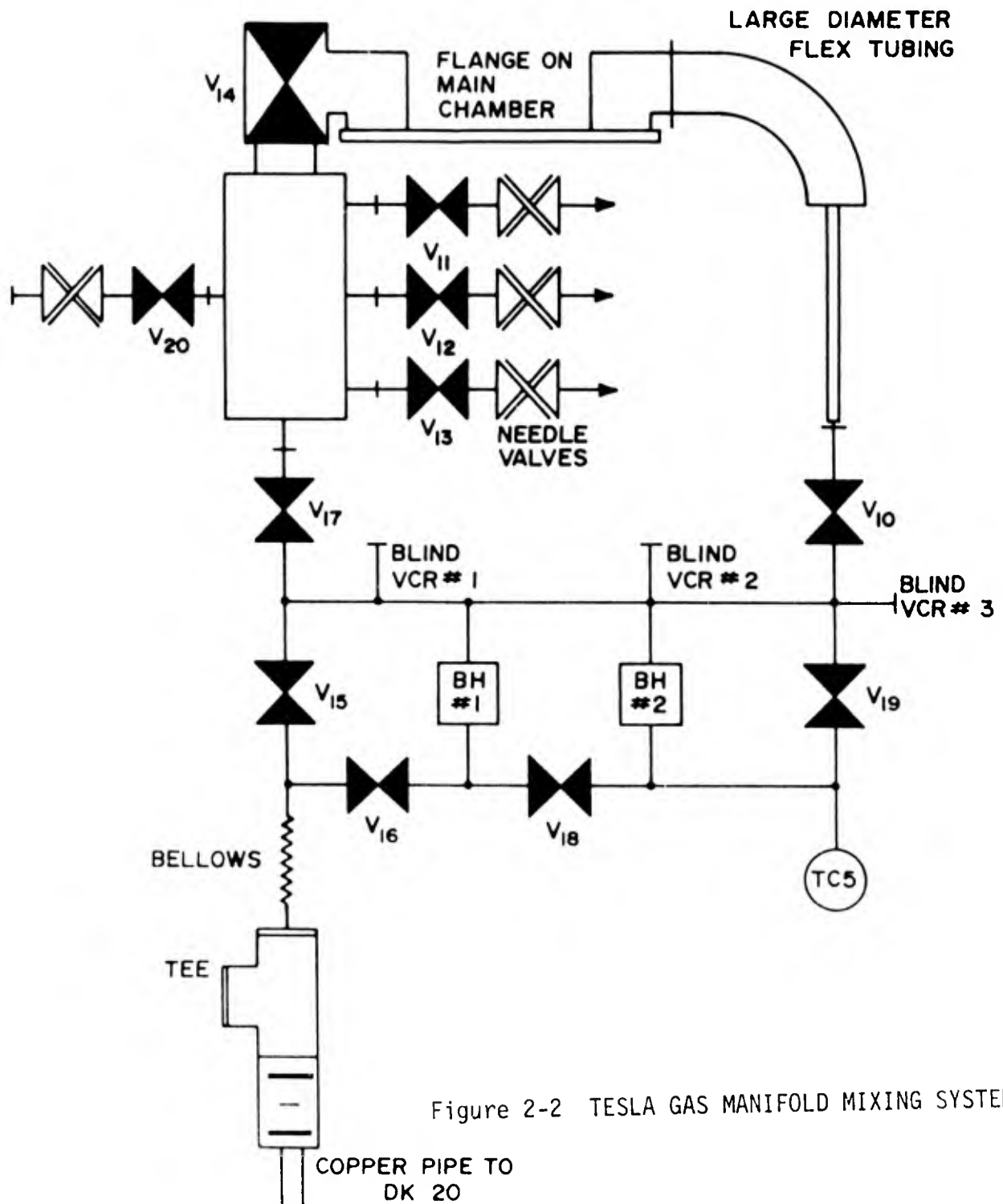


Figure 2-2 TESLA GAS MANIFOLD MIXING SYSTEM

collect samples either from the manifold or from the discharge chamber. MKS Baratron<sup>tm</sup> heads can be used to measure the pressures in either the gas manifold or in the discharge chamber. The gas manifold is capable of being overfilled so that the test chamber can be repeatedly filled from the manifold.

Salient features of the gas manifold design are illustrated in Figure 2-2 as follows. To insure a low ultimate pressure of the manifold, it is connected to the main chamber through a relatively large throughput metal seal valve  $v_{14}$ . All the valves in the system with the exception of the metering valves can withstand 400 C in the closed position. The entire system on the high vacuum side of the foreline trap is constructed of stainless steel. The DK20 mechanical pump is used to provide a reference pressure for the Baratrons, to evacuate gas sample bottles before filling, and to rough out the manifold when required.

The data collection electronics consists of two model 466 Tektronix storage oscilloscopes, a Tektronix 20 KV probe, a model 110 Pearson current probe and a large copper enclosure which houses the electronics and provides EMI shielding. A Polaroid camera is used to take pictures of the scope traces and the photographs are saved for later analysis. The schematic diagram in Figure 2-3 shows the electrical connection between the preionizers, main firing circuits and the detection electronics. All the electronic equipment was synchronized by means of a cable delay unit; it was found that this type delay had less timing jitter and less susceptibility to false firing due to EMI pickup. A TTL based delay unit was designed and constructed; the unit was tested and

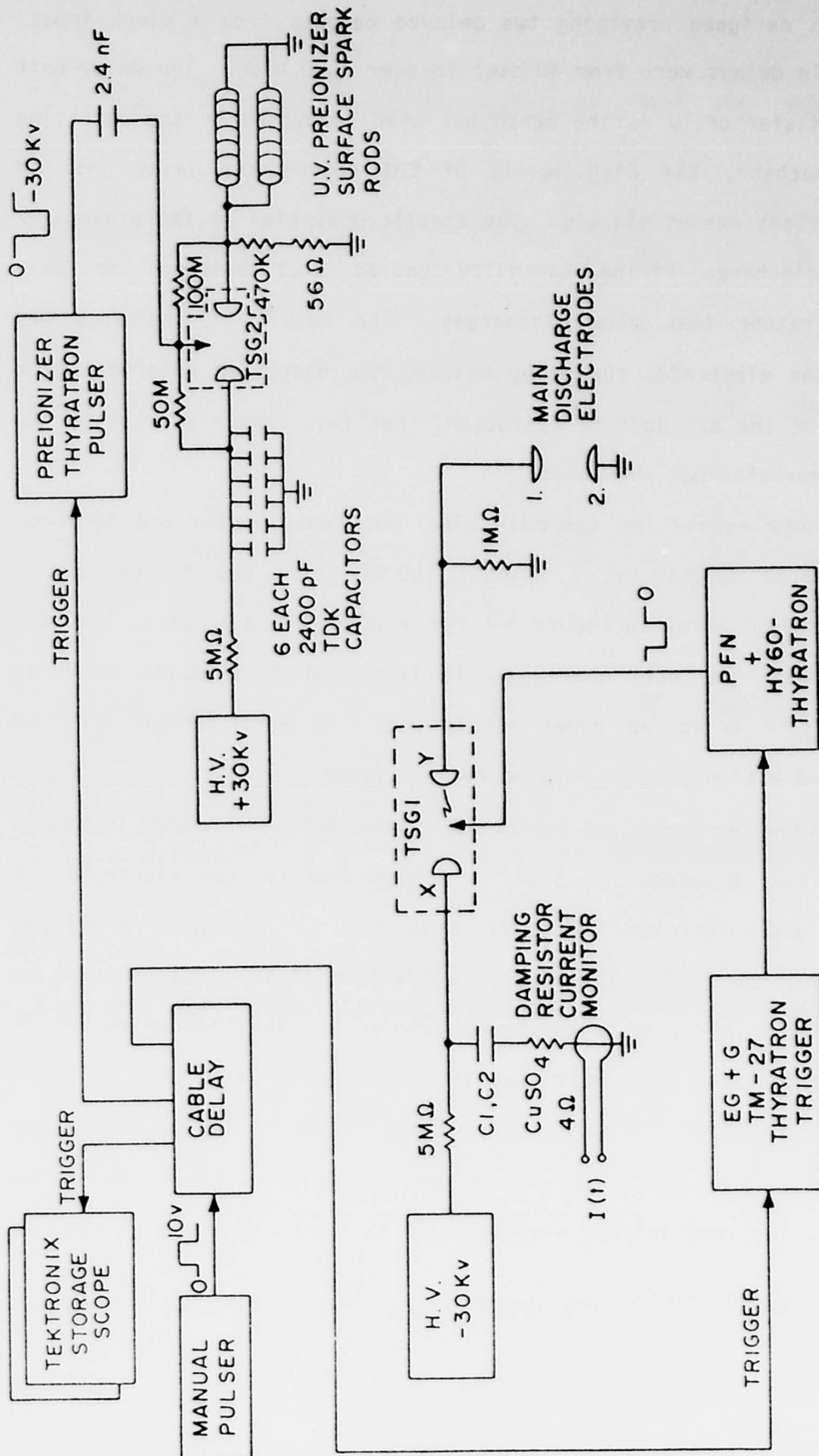


Figure 2-3



performed as designed providing two delayed outputs from a clock input. The available delays were from 40 nsec to over 1000 nsec. The delay unit operated satisfactorily on the bench but when connected to the operating discharge machine, the high levels of EMI caused the delay unit to produce spurious output signals. The erratic operation of the preionizer and main discharge firing circuitry caused arcs between the main electrodes rather than glow discharges. The result of the arcs was damage to the electrodes caused by melting the electrode material which is typical of the arc mode of operation. For this reason the use of the TTL delay generator was abandoned.

The power supply for the main electrodes consists of one to three 0.06 microfarad capacitors, a Maxwell 100 KV spark gap trigger and a 30 KV DC supply. Refer to Figure 2-4 for a schematic diagram of the main firing system. The main spark gap is triggered by a pulse which is generated in a triggered power supply which is built around a HY-60 thyatron and a simple pulse forming network (pfn).

The triggered spark gap connected to the main electrodes is biased so that initial breakdown of TSGI is between the trigger electrode and the spark gap electrode which is connected to the main electrode labeled 1 in Figure 2-3. This causes a fraction of the trigger pulse to appear on the main discharge electrode labeled 1. This low energy pulse aids in preionizing the main gap by breaking it down for a short (40 nsec) time before the main voltage from C1 and C2 is applied to the electrodes by spark gap, TSGI. This application of a short low energy pulse to provide some initial preionization is very similar in concept to

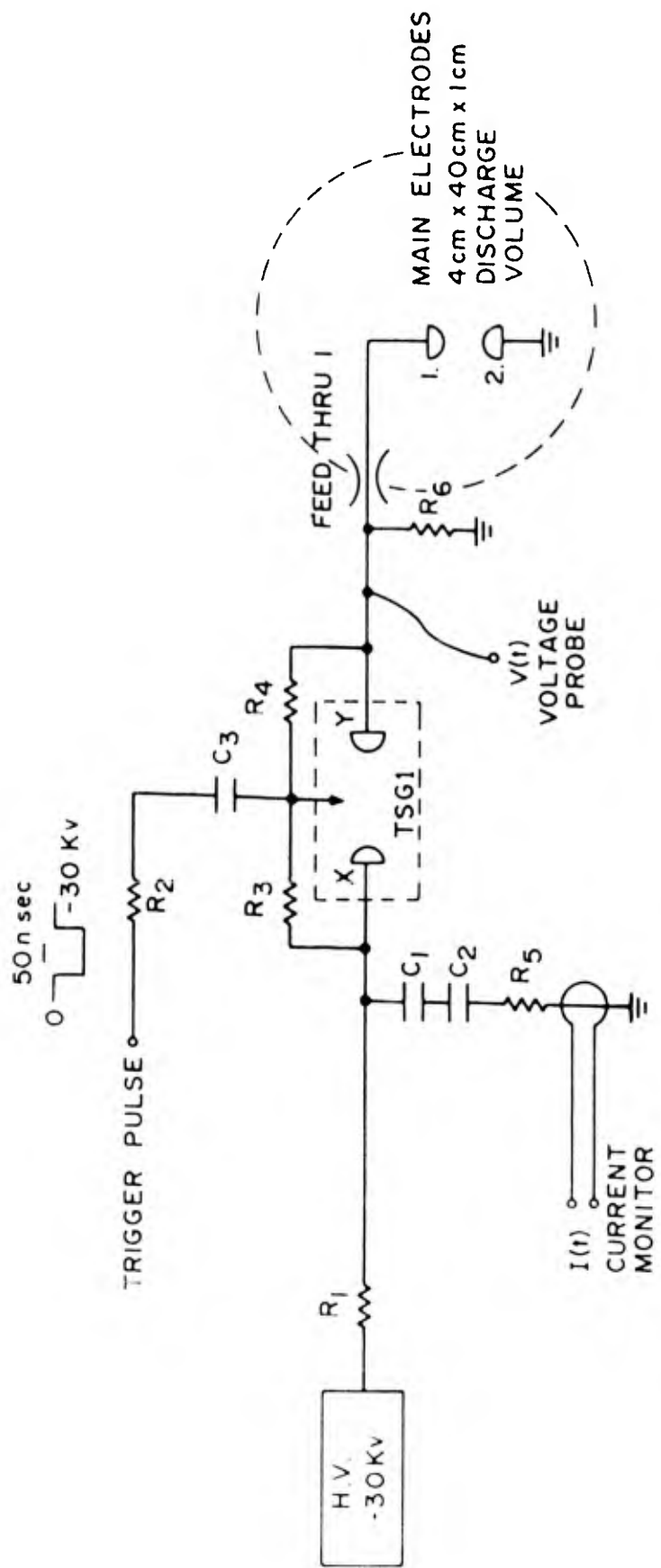


Figure 2-4

the "poker pulse"<sup>22</sup> used in CO<sub>2</sub> lasers. What is novel in the present application is the source of the prepulse i.e. from the triggering pulse applied to the spark gap. The pulse has very little effect on the main discharge as is evidenced on the current waveforms where no effect from this pulse is seen. The effect of this prepulse on the main gap current was not observable on the scale used in the photographs; however, the prepulse was clearly seen as a separate voltage pulse, see Figure 2-6 for an example of this type data. The effect of the prepulse on the uniform initiation of the main discharge was dramatic. Without the prepulse, the delay between the preionizer and the main discharge firing was very critical. However, the timing delay could be adjusted over a wide range of time when the prepulse was utilized and still have a uniform glow discharge between the main electrodes. The timing sequence when the apparatus is fired is the following: (1) surface spark preionizers fire, (2) delay of 50 to 1500 nsec, (3) TSG1 trigger, (4) trigger pulse appears on electrode 1, (5) delay due to TSG1 breakdown, (6) main voltage pulse appears on electrode 1.

The preionizers for the main discharge utilized surface spark discharges along rods mounted on both sides of the main electrodes. Surface spark arrays produce ions by the production of large flux of uv photons which ionize the gas in the surrounding volumes. Figure 2-5 is an electrical diagram of the spark gap trigger unit used to generate a trigger pulse for the preionizer spark gap. Figure 2-3 shows the electronic circuitry that controlled the preionizers and triggered them a set, variable time delay before the main electrodes fired.

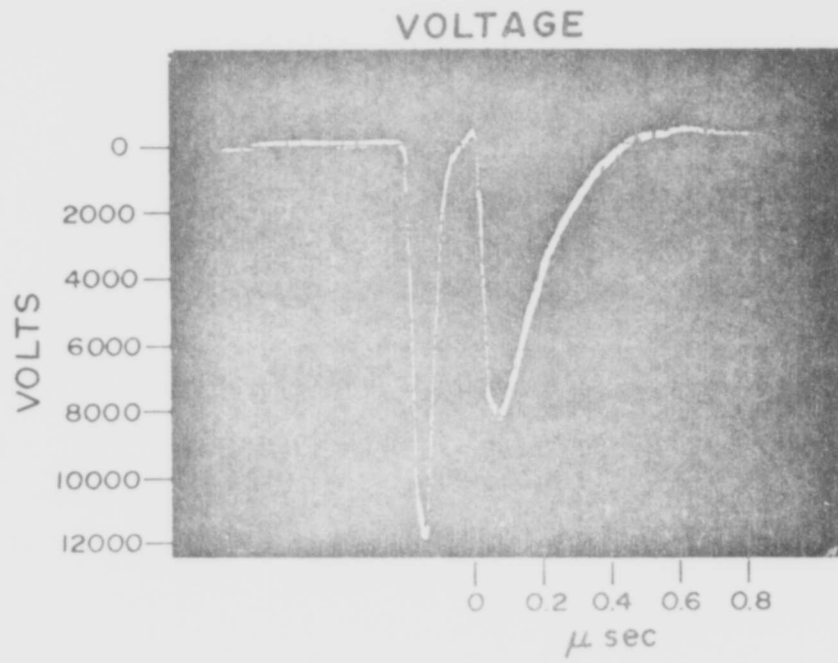
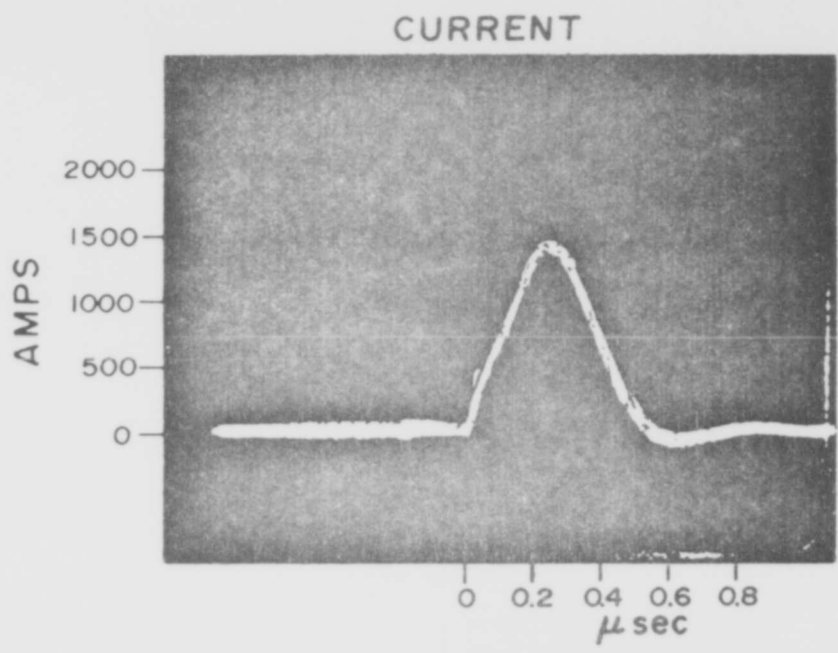


Figure 2-6 VOLTAGE/CURRENT vs. TIME

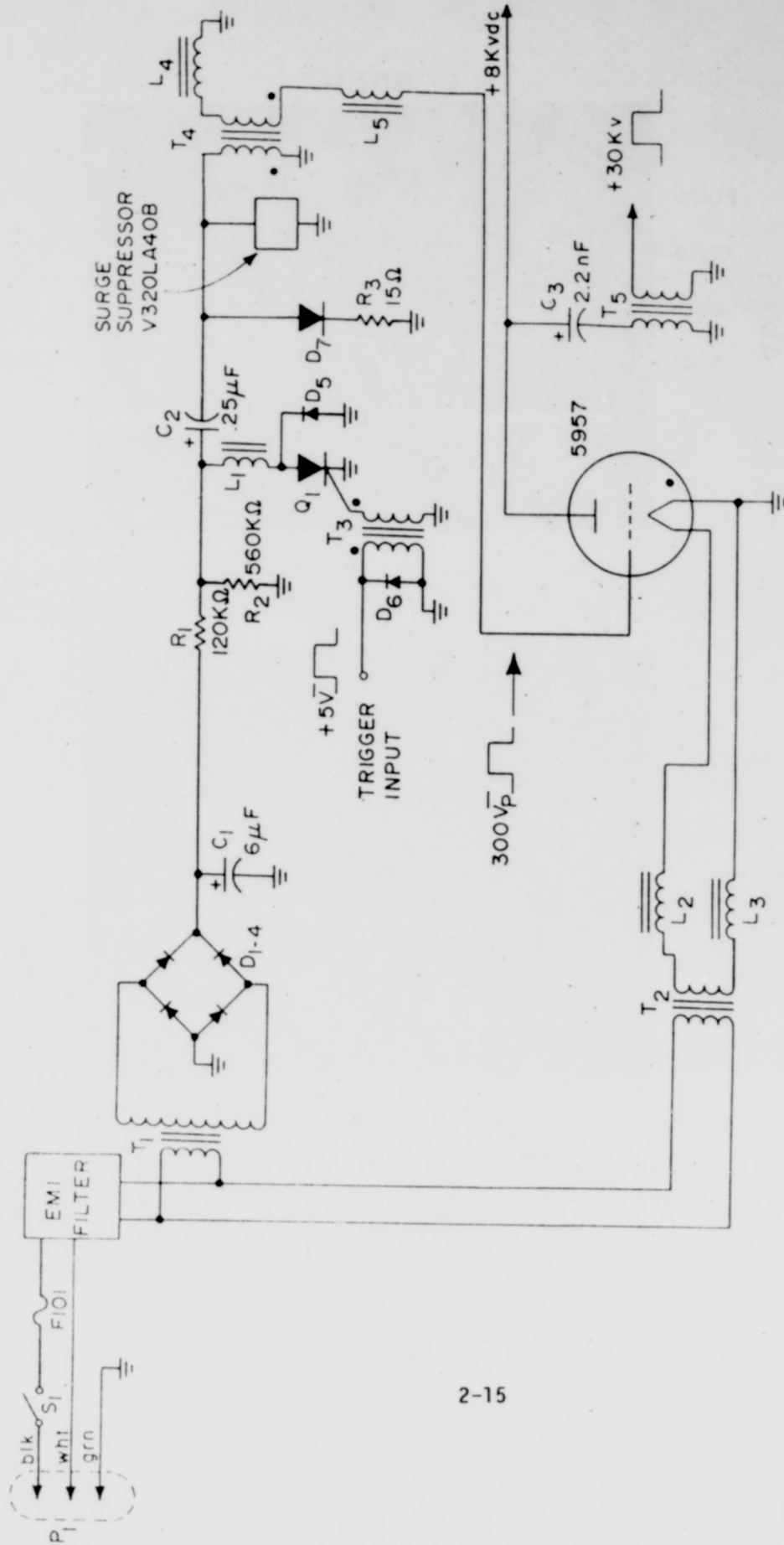


Figure 2-5

The preionizers were tested by collecting the charge produced between the main electrodes with a small d.c. bias voltage. The voltage on the main electrodes was varied and the peak current versus bias voltage was plotted. The plot in Figure 2-8 indicates that a plateau is reached in the collected current from 1000 to 2000 volts. Below the plateau region all the charge between the main electrodes was not collected and above that region ionization is produced due to the high E/N. Knowing the current, I, mobility, W, of the electrons in the gas (N<sub>2</sub>) as a function of E/N and the gas pressure, P, the charge density in the gas can be calculated. Since the positive ion mobility is so much smaller than the electron mobility, the ion current can be ignored. The electron density can be calculated from the following formula.

$$n(e) = I / (AeW).$$

$$W = 3 \times 10^6 \text{ cm/sec for } E/p = 6.7 \text{ v/cm-torr (see reference 30).} \quad (2-3)$$

$$e = 1.6 \times 10^{-19} \text{ coulomb.}$$

$$I = 3.5 \text{ amps, peak current.}$$

$$A = 160 \text{ cm}^2.$$

This gives a value for  $n(e) = 4.6 \times 10^{10} \text{ cm}^{-3}$ . This is a reasonable result compared to other discharge machines using this type of preionization<sup>2,19</sup> and certainly proved sufficient in later experiments to initiate a uniform glow discharge.

The main electrodes were machined from aluminum and the final profile was determined by trial and error by observing the location of arcs along the edges of the electrodes. The electrodes were machined by observing the location of arcs along the edges of the electrodes. The electrodes were polished by hand to a mirror finish using aluminum oxide

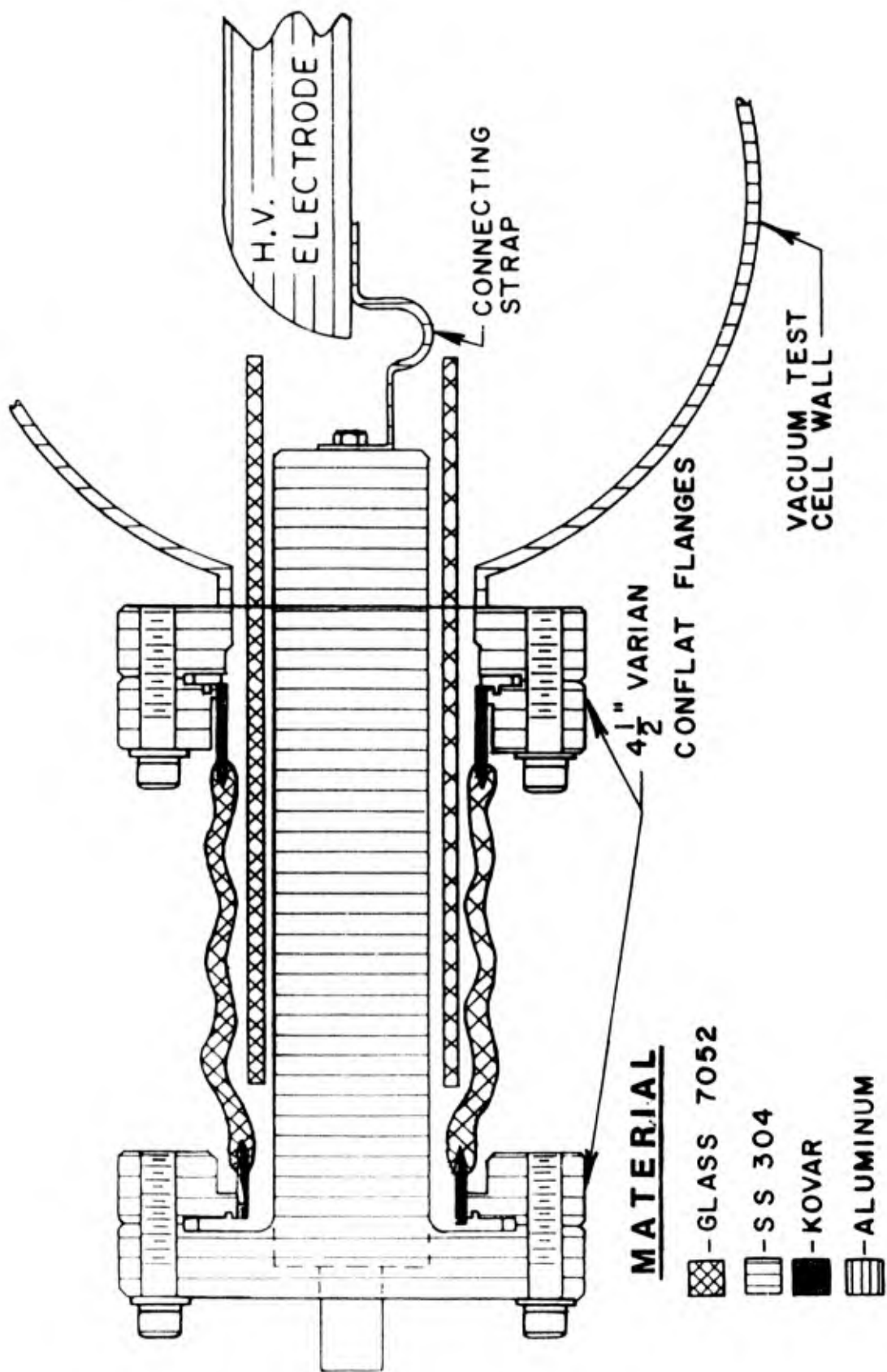


Figure 2-7 TESLA HIGH VOLTAGE FEEDTHRU

PREIONIZER TEST  
 PEAK CURRENT vs. D.C.  
 VOLTAGE ON ELECTRODE

250 torr OF N<sub>2</sub>  
 1 cm gap

PEAK CURRENT (Amperes)

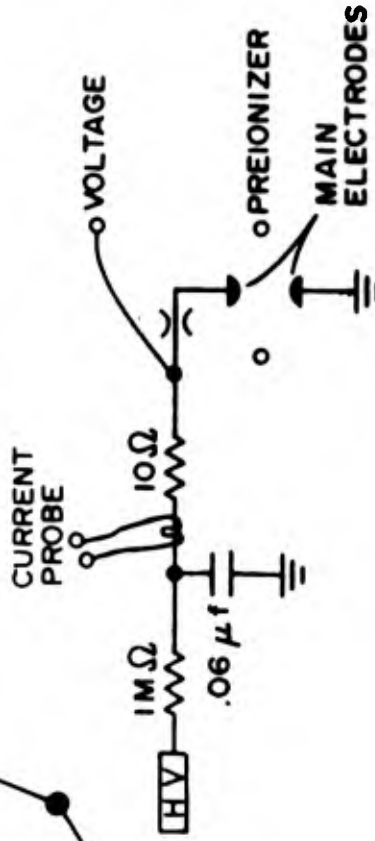
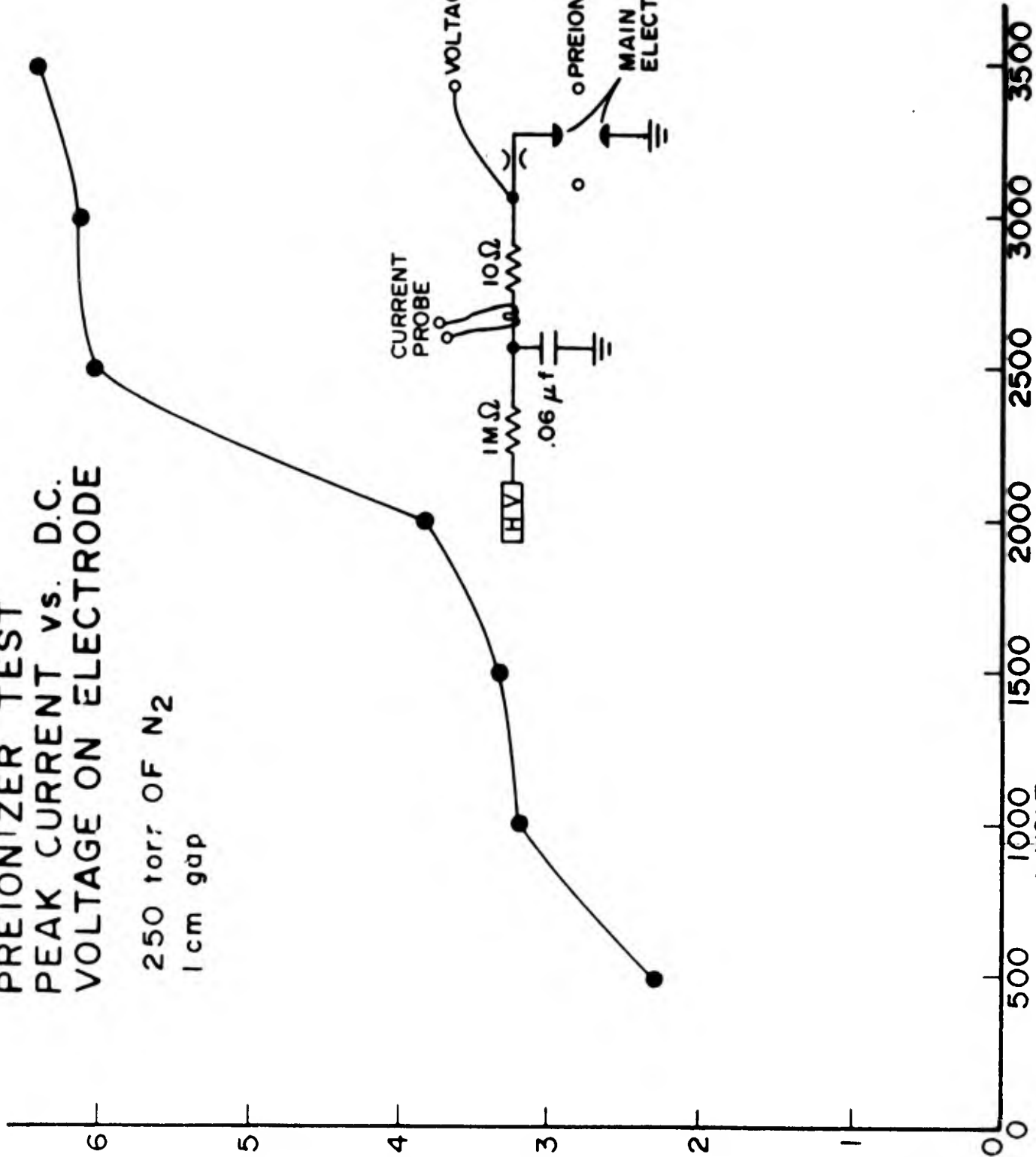


Figure 2-8 D.C. VOLTAGE APPLIED TO MAIN ELECTRODE



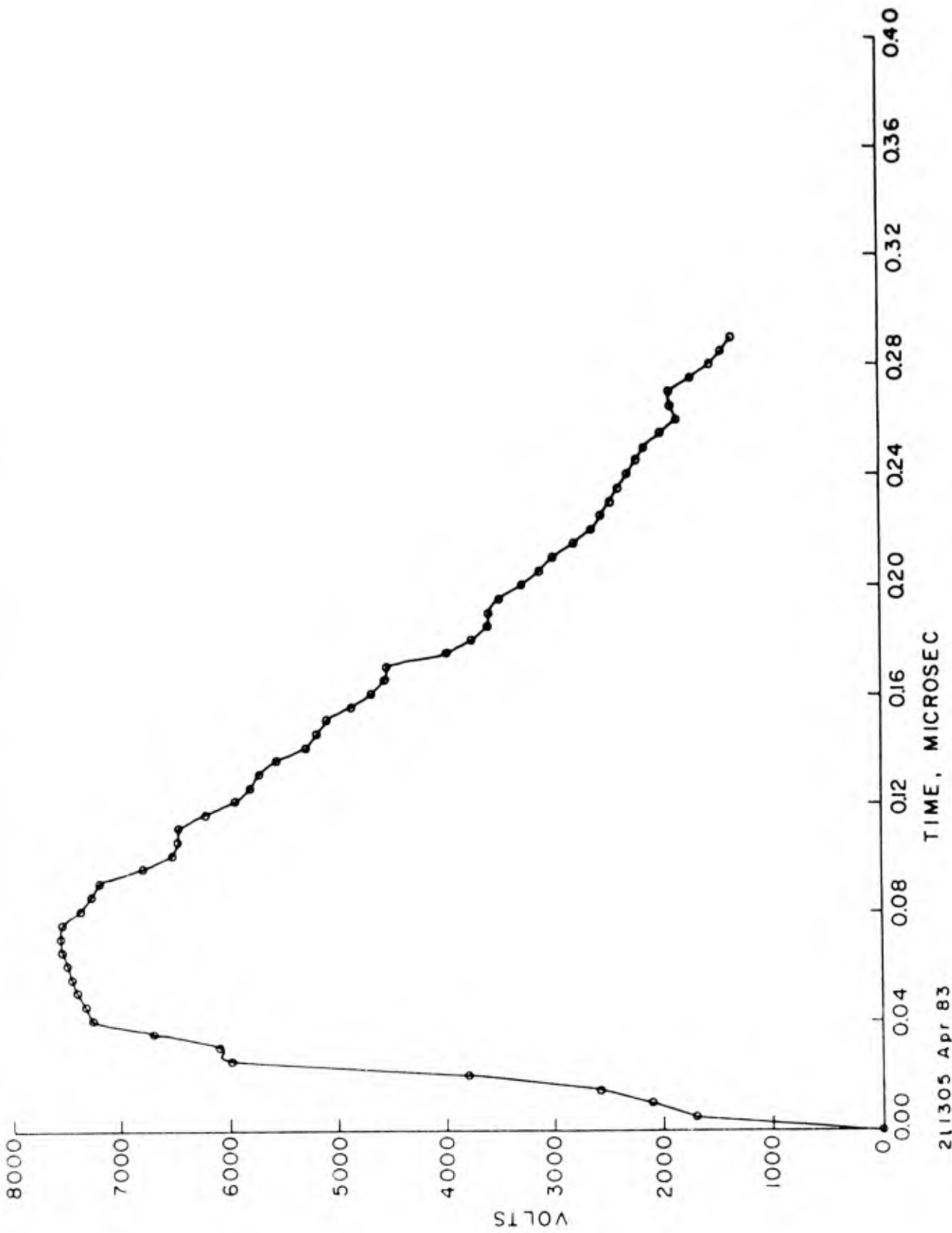
powder. The area of the discharge on the electrodes was approximately 4 cm by 40 cm.

The main high voltage feedthru (Figure 2-7) was designed and built locally at Building 450<sup>23</sup> due to time and cost considerations. It consisted of two glass kovar seals on 4.5 inch conflat flanges and connected together on the glass side. The high voltage conductor was 3.8 cm in diameter and 19 cm long. The feedthru was tested for corona inception and arcing voltage in air. These voltages were found to be 4KV and 66 KV respectively.

### TESLA RESULTS

A typical set of  $V(t)$  and  $I(t)$  curves are shown in Figure 2-6. These curves are the original photographs. The first pulse on the  $V(t)$  curve is the prepulse which was used to aid preionization and the main voltage pulse can be seen after it. The voltage and current curves in Figures 2-9 and 2-10 have been digitized using an automatic digitizer. The resulting data was interpolated by means of a spline fit routine<sup>25</sup> smoothed, differentiated and plotted using a PRIME 850 minicomputer and a CALCOMP plotter. The prepulse on the voltage curve was not included in the digitized curve since its effect on the discharge was negligible except to provide some initial preionization. The voltage across the discharge was calculated using the technique of Pack and Liberman<sup>28</sup> to correct for the voltage drop across the inductive component of the discharge circuit. The circuit inductance was determined both by shorting the electrodes or operating in the arc mode, and measuring the resulting ringing waveform. The inductance was measured from the frequency of the damped oscillations by standard techniques. The circuit

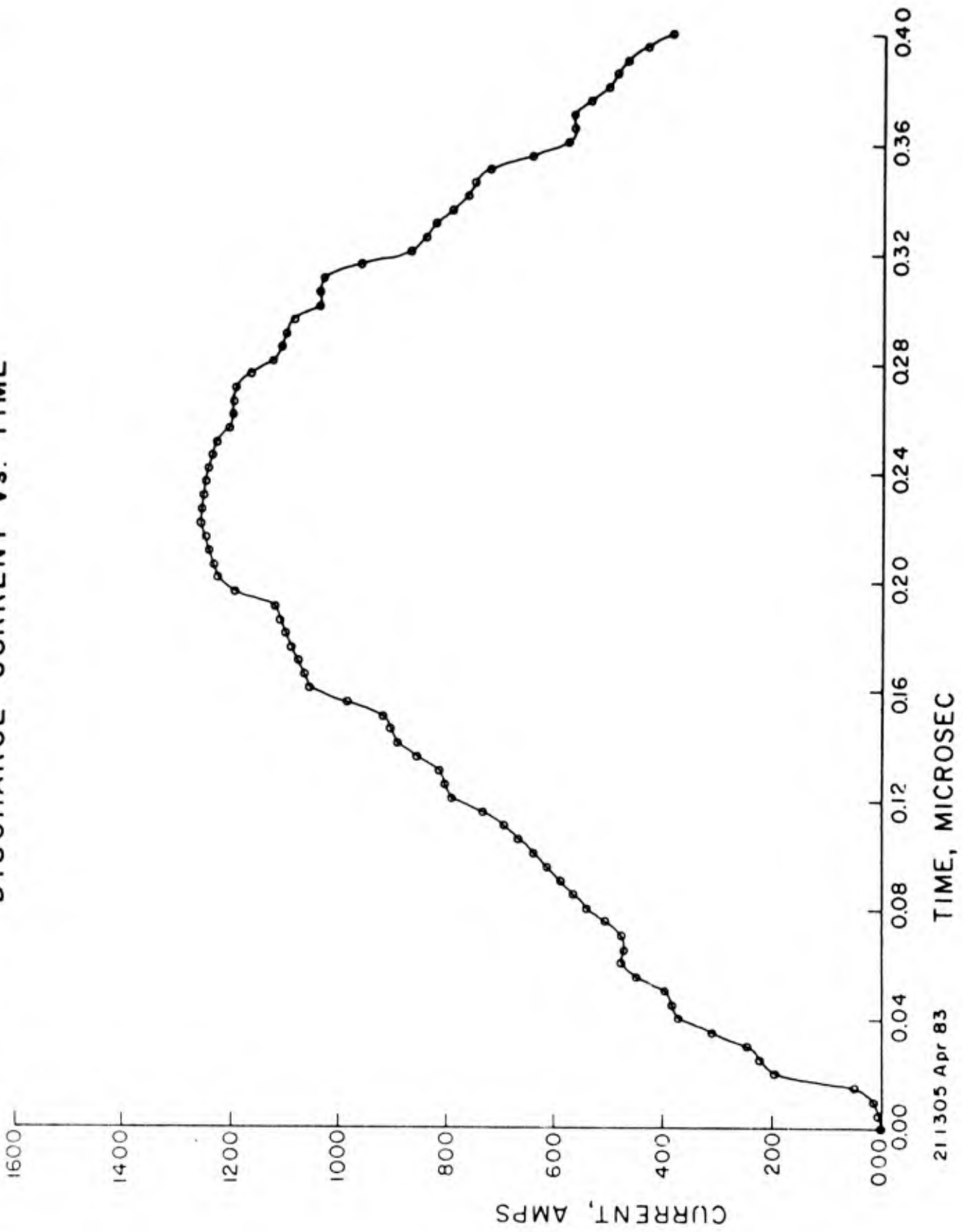
UNCORRECTED DISCHARGE VOLTAGE vs. TIME



211305 Apr 83

Figure 2-9 UNCORRECTED DISCHARGE VOLTAGE vs. TIME

DISCHARGE CURRENT vs. TIME



211305 Apr 83

22-2

Figure 2-10 DISCHARGE CURRENT vs. TIME

inductance,  $L$ , was determined to be 300 nanohenries. This value of inductance was used in a formula that relates the voltage,  $V(t)$ , measured with the oscilloscope, the voltage drop across the circuit inductance and the discharge voltage. The voltage across the discharge,  $V(d)$ , is given by the expression  $V(d)=V(t)-V(sh)-LdI/dt$ .<sup>28</sup> Where  $I$  is the current in the discharge circuit and  $V(sh)$  is the voltage drop across the cathode sheath. The curve of  $V(d)$  is shown in Figure 2-11. It is apparent from the data in Figure 2-9 and 2-11 that there is not a large voltage drop across the circuit inductance. The resistivity,  $RR(t)$ , of the discharge as a function of time is shown in Figure 2-12. Finally, the power,  $P(t)$  dissipated in the switch as a function of time is shown in Figure 2-13. The correction for the potential drop in the cathode sheath that was applied to find the discharge voltage is only approximate. A voltage drop of 200 volts was assumed but was not determined in this experiment. This figure was a reasonable estimate based on the data for sheath voltages which is presented in Von Engel.<sup>26</sup> One of the objectives of measuring the current and voltage curves at several electrode spacings was to determine the voltage drops across the cathode sheath. The data for the resistivity at peak current (not corrected for sheath voltages) for three electrode spacings is shown in Figure 2-14. The three curves were fitted using a polynomial fitting routine and interpolated data were calculated using the given third order polynomial fits. The voltage drops across the discharge are plotted as a function of current density in the discharge for three electrode spacing. The relationship between the

CORRECTED DISCHARGE VOLTAGE vs. TIME

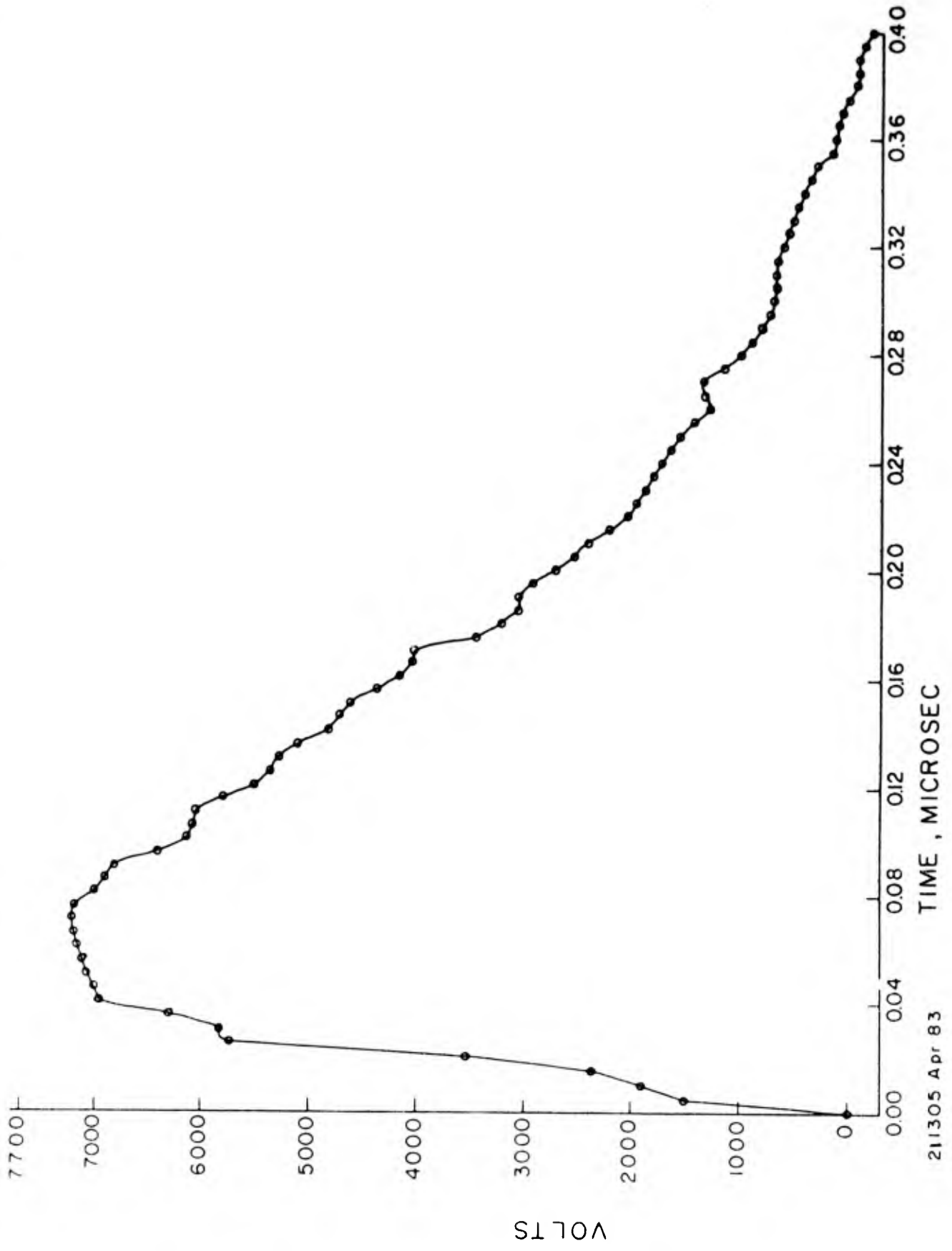
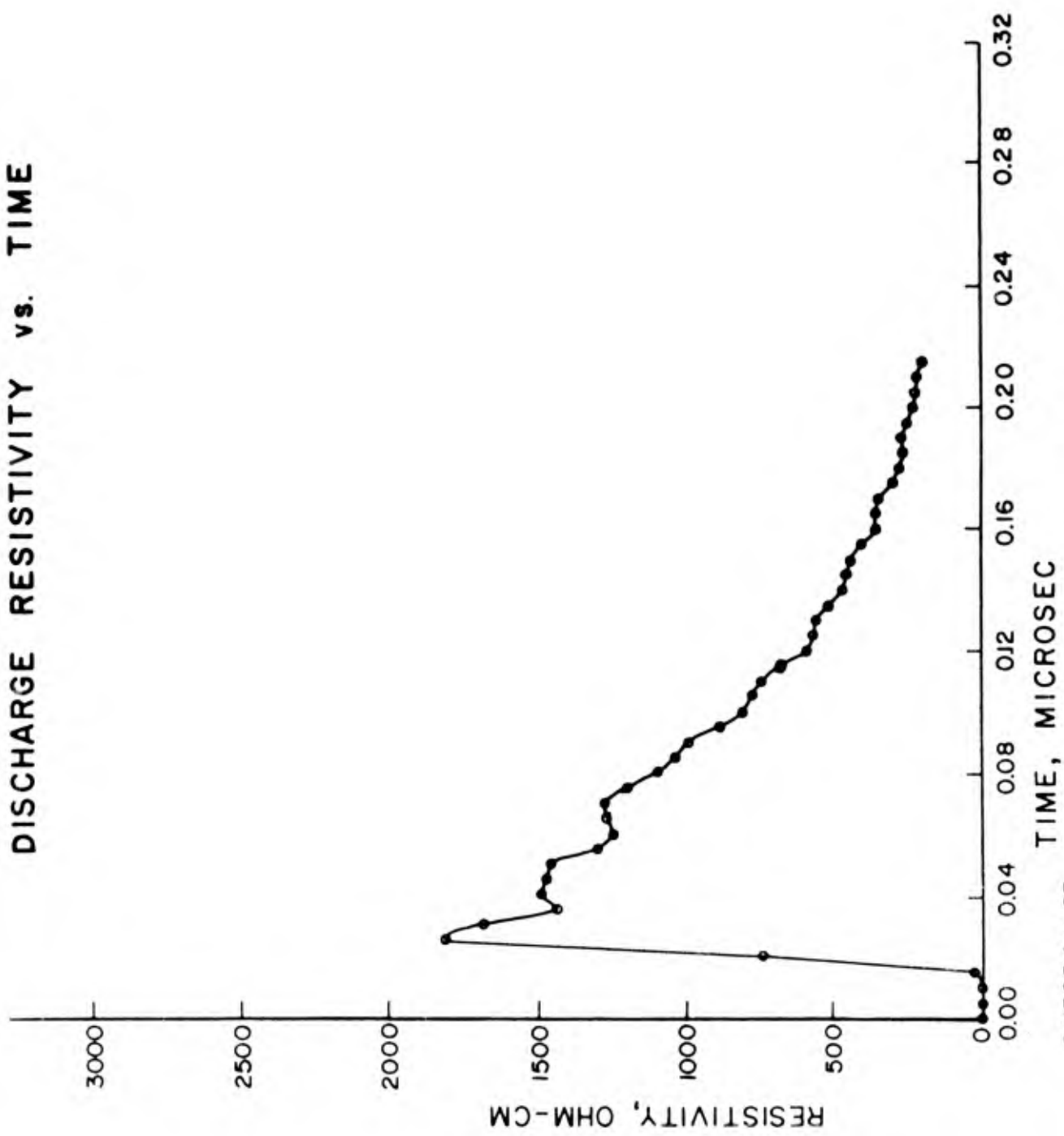


Figure 2-11 CORRECTED DISCHARGE VOLTAGE vs. TIME

211305 Apr 83

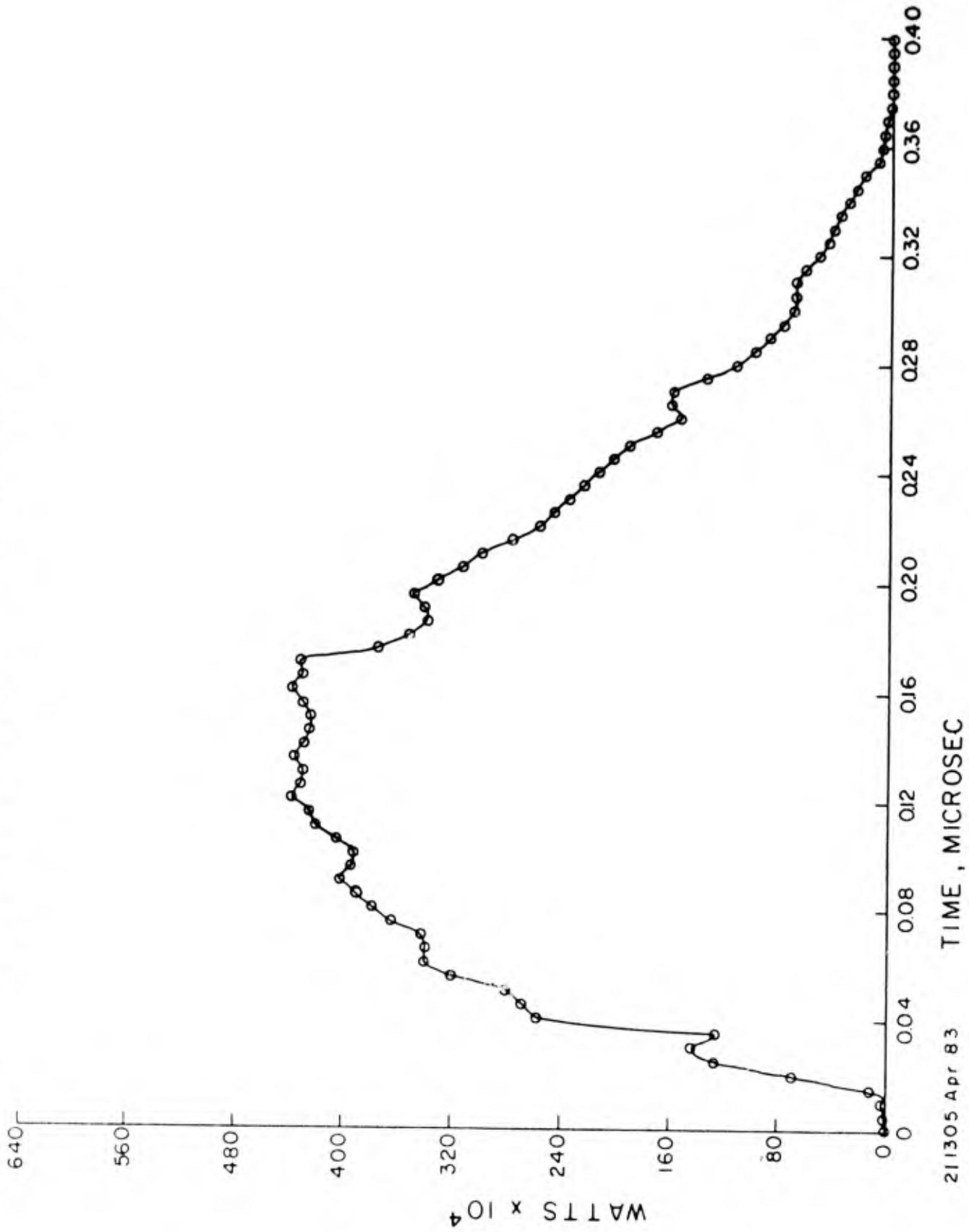
# DISCHARGE RESISTIVITY vs. TIME



211305 Apr 63

FIGURE 2-12 DISCHARGE RESISTIVITY vs. TIME

POWER DISSIPATED IN SWITCH vs. TIME



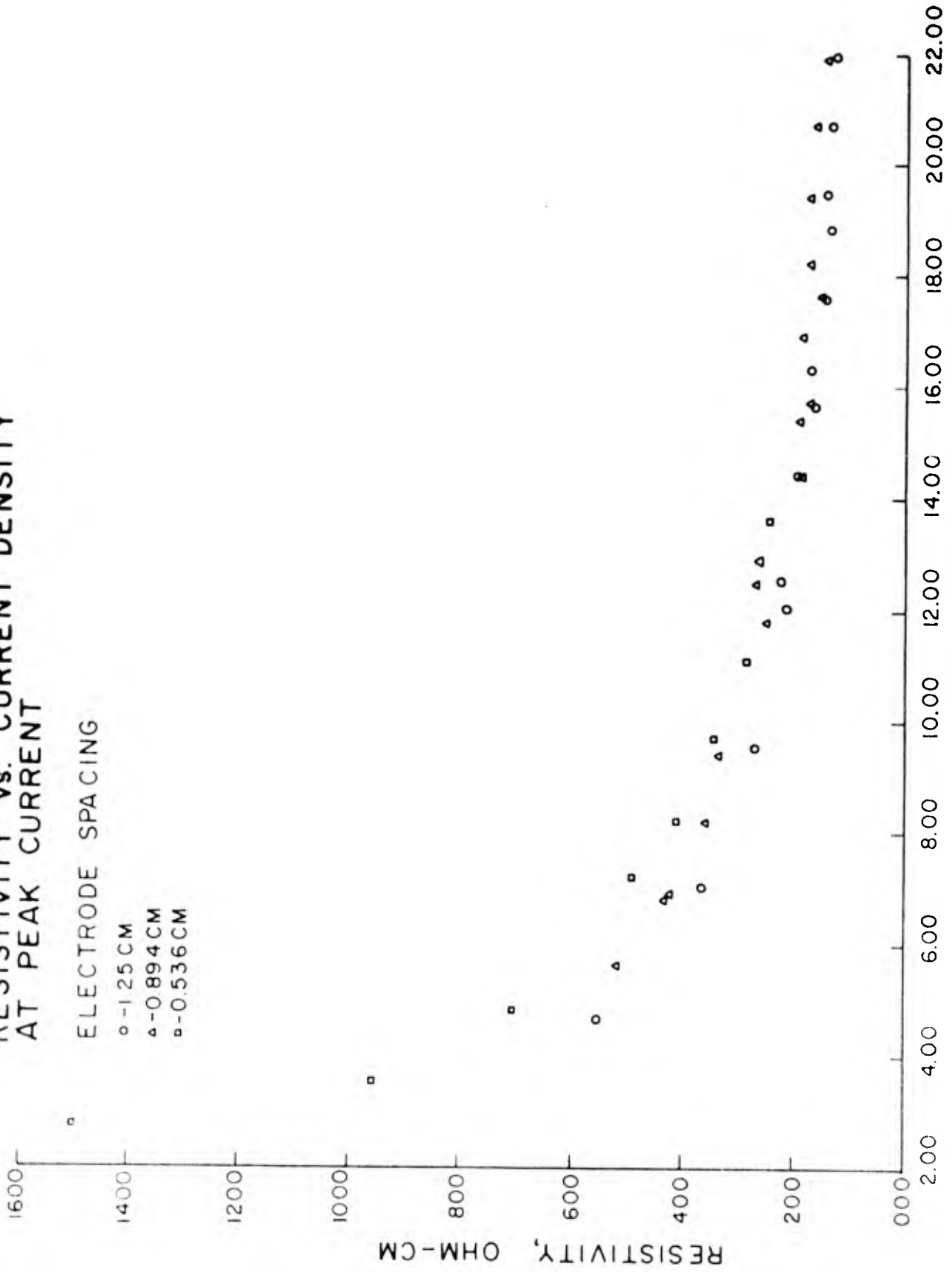
211305 Apr 83

Figure 2-13 POWER DISSIPATED IN SWITCH vs. TIME

# RESISTIVITY vs. CURRENT DENSITY AT PEAK CURRENT

ELECTRODE SPACING

- - 1.25 CM
- △ - 0.894 CM
- - 0.536 CM



211305 Apr 83

Figure 2-14 RESISTIVITY vs. CURRENT DENSITY AT PEAK CURRENT



voltage and the current density vs. electrode spacing was not clear from the preceding analysis. It was intended to extrapolate this smoothed data to zero electrode spacing and obtain the sheath voltages. This is similar to a procedure used to obtain the same information by Doran<sup>31</sup> for hydrogen. The present results may indicate that some discharge parameter such as electrode surface condition was changing during the course of the data collection.

Using the relationship among current density, electron density and electron drift velocity, we obtain from equation 2.1.

$$\gamma = \frac{I}{eAW} \left[ \alpha W + \frac{\partial W}{\partial (E/N)} \frac{\partial E}{\partial t} \frac{1}{NW} \right] \quad (2-4)$$

The following values were used in the calculation of the recombination coefficient:

$d = 0.894$  cm, electrode gap

$e = 1.6 \times 10^{-19}$  coulomb

$A = 160$  cm<sup>2</sup>, area of the electrodes

$N = 2.51 \times 10^{19}$  cm<sup>3</sup>, gas density in the discharge region (760 torr, 20 C)

$W = 5.254 \times 10^6$  cm/sec, electron drift velocity (ref. 15)

$E/N = 9.14$  td

$J = 7.86$  amps/cm<sup>2</sup>, peak current density

$\frac{\partial W}{\partial (E/N)} = 4.8533 \times 10^{23}$  1/sec-volt-cm), partial derivative with respect to  $E/N$  (ref. 30)

$K = 5 \times 10^{22} \text{ cm}^3/\text{sec}$ , ionization rate coefficient (ref. 30)

$\alpha = KN/W = 2.389 \times 10^{-9} \text{ 1/cm}$ , ionization coefficient (calculated from the value in ref. 30)

$I = 1257.3 \text{ amps}$ , peak current from Figure 2-10

The partial derivative of electric field with respect to time was calculated from the experimental data presented in Figure 2-11 after it was differentiated.<sup>15</sup>

$$\frac{\partial E}{\partial t} = 27.9 \times 10^9 \text{ volt/cm-sec} \quad (2-5)$$

This results in a value for the recombination coefficient of  $\delta = 1.08\text{E-}6 \text{ cm}^3/\text{sec}$  at  $E/N = 9.14 \text{ Td}$ . This can be compared to the values for pure Nitrogen and pure Argon in Table 2-1. From this comparison, one can conclude that the calculated value for the recombination coefficient for the Nitrogen/Argon gas mixture is reasonable. Other recombination data for this gas mix were not available for comparison.

A study was undertaken to determine a method to measure the temperature of the gas in the discharge. The study was completed, but the techniques were not implemented in the laboratory. The results of the study are presented in Appendix B for reference.

Table 2-1

Ion Reactions in Nitrogen-Argon Mixtures

<u>Binary Reactions</u>	<u>Rate Coefficient</u>	<u>Reference</u>
(1) $\text{Ar}^+ + \text{N}_2 - \text{N}_2^+ + \text{Ar}$	$k = 7 \times 10^{-12} \text{cm}^3/\text{s}$	17, pg 1392f
	$k = 4.9 \times 10^{-12} \text{cm}^3/\text{s}$	17, pg 2782
	$k = 0.85 \times 10^{-12} \text{cm}^3/\text{s}$	17, pg 2782
(2) $\text{N}_2^+ + \text{N} - \text{N}^+ + \text{N}_2$	$k = 1 \times 10^{-11} \text{cm}^3/\text{s}$	17, pg 1392f
<u>Ternary Reactions</u>		
(3)** $\text{N}^+ + \text{N}_2 + \text{He} - \text{N}_3^+ + \text{He}$	$k = 8.6 \times 10^{-30} \text{cm}^6/\text{s}$	17, pg 1392f
(4) $\text{N}^+ + \text{N}_2 + \text{N}_2 - \text{N}_3^+ + \text{N}_2$	$k = 1.8 \times 10^{-29} \text{cm}^6/\text{s}$	21
(5)** $\text{N}_2 + \text{N}_2 + \text{He} - \text{N}_4^+ + \text{He}$	$k = 1.0 \times 10^{-29} \text{cm}^6/\text{s}$	21, 17
(6) $\text{Ar}^+ + 2\text{Ar} - \text{Ar}_2^+ + \text{Ar}$	$k = 2.5 \times 10^{-31} \text{cm}^6/\text{s}$	10
(7) $\text{Ar}^{+*} + 2\text{Ar} - \text{Ar}_2^+ + \text{Ar}$	$k = 2.7 \times 10^{-31} \text{cm}^6/\text{s}$ for $2P_{3/2}$	21
	$k = 2 \times 10^{-32} \text{cm}^6/\text{s}$ for $2P_{1/2}$	21
(8) $\text{Ar}_2^+ + 2\text{Ar} - \text{Ar}_3^+ + \text{Ar}$	$k = 4.2 \times 10^{-33} \text{cm}^6/\text{s}$	21
<u>Recombination Reactions</u>		
(9) $\text{Ar}_2^+ + e - \text{Ar}^* + \text{Ar}$	$k = 6.7 \times 10^{-7} \text{cm}^3/\text{s}$	17, pg 1495, 4
(10) $\text{N}_4^+ + e - \text{neutral products}$	$k = (1.5 \pm 0.3) \times 10^{-6} \text{cm}^3/\text{s}$	3

\*\* Data is not available for these reactions with argon instead of helium as a collision partner.

## REFERENCES

1. Bailey, W.F., Duke, G., and Garscadden, A., 1979 paper CB-6 at 32nd Gaseous Electronics Conference.
2. Beverly III, R. E., 1978, "Light Emission from High Current Surface Spark Discharges", Pg 357 of Progress in Optics XVI, Ed. by E. Wolf (North Holland).
3. Biondi, M. A., 1982, "Electron Ion Recombination in Gas Lasers" pg 173 in Applied Atomic Collision Physics, Vol. 3, Gas Lasers (Academic Press).
4. Christophorou, L. G., Hunter, S. R., Carter, J. G., and Mathis, R. A., 1982, Appl. Phys. Lett. 41, 147.
5. Douglas-Hamilton, D. H., 1973, J. Chem. Phys. 58, 4820.
6. Dutton, J., 1979, "Spark Breakdown in Uniform Fields" pg 209 of Electrical Breakdown of Gases, Ed. by J. M. Meek and J. D. Craggs (J. Wiley and Sons).
7. Fishburne, E. S., 1967, J. Chem. Phys. 47, 58.
8. Garscadden, A., Vailey, W. F., and Duke, G. L., 1981 paper at Plasma Chemistry Meeting.
9. Hallada, M. R., Bletzinger, P., and Bailey, W. F., 1982, IEEE Trans. Plasma Science PS-10 pg 218.
10. Hill, R. M., Gutcheck, R. A., Huestis, D.L., Mukherjee, D., and Lorents, D. C., 1974, "Studies of E-beam pumped Molecular Lasers", SRI report MP-74-39.
11. Hunter, R. O., 1976, paper IC8 at First International Pulsed Power Conference.

12. Kline, L.E., 1974, J. Appl, Phys. 45, 2046.
13. Kline, L. E., 1982, IEEE Trans. Plasma Science Vol PS-10, 224.
14. Kline, L. E., and Denes, L. J., 1975, J. Appl. Phys. 46, 1567.
15. Long Jr., W. H., Bailey, W. F., and Garscadden, A., 1976 Phys. Rev. A 13, 471.
16. Mackellar, G. R., and Piper, J. A., 1981, paper at Lasers 81 Conference, pg 654 of proceedings.
17. McDaniel, E. W., et al, 1978 "Compilation of Data Relevant to Nuclear Pumped Lasers", Technical Report H-78-1.
18. Meyer, T. W., Hines, J. D., Tannen, P.D., and Jernigan, R. E., 1976, paper at Gaseous Electronics Conference.
19. Norris, B., and Smith, A. L. S., 1977, J. of Phys. E: Sci. Instrum., Vol. 10, pg 551.
20. Piper, L. G., Richardson, W. G., Taylor, G. W., and Setser, D. W., 1972, Faraday Discussions of Chemical Society, 1972, no. 53, pg 100.
21. Wiegand, W. J., 1982, "High Pressure Ion Kinetics", pg 71 in Applied Atomic Collision Physics, vol. 3, Gas Lasers, (Academic Press).
22. A. J. Demaria in "Principles of Laser Plasmas" Ed. G. Bekefi, 1976 Wiley, N.Y.
23. A special thanks goes to Jim Ray, the glass blower in building 450. Without his expertise, the work could not have been completed.
24. H.S.W. Massey, ELECTRONIC AND IONIC IMPACT PHENOMENA VOLUME II, Oxford at the Clarendon press (1969).
25. F.R. Ruckdeschel, BASIC SCIENTIFIC SUBROUTINES VOLUME II, McGraw Hill (1981), Peterborough, NH.
26. A. Von Engel, IONIZED GASES, Oxford at the Clarendon Press (1965).

27. J. D. Cobine "Gaseous Conductors" 1941 McGraw-Hill, N.Y.
28. J. L. Pack, I. Liberman, Review of Scientific Instruments 52, 1580 (1981).
29. J. W. Dzimianski, L. E. Kline, Technical Report AFWAL-TR-80-2041 April 1980.
30. A. Garscadden, Wright Patterson AFB, Dayton, Ohio, AFWAL/POOC, private communication.

0053z

SECTION 3  
ELECTRON DISSOCIATIVE IMPACT EXCITATION  
OF  $\text{HgBr}_2$

INTRODUCTION

Since the observation of lasing <sup>1-5</sup> in the B→X transition of HgBr which occurs in electrical discharges in  $\text{HgBr}_2$  vapor, there have been numerous studies of the discharge characteristics of  $\text{HgBr}_2$ .<sup>6-9</sup> Interest in the spectroscopy of  $\text{HgBr}_2$  dates at least to 1930.<sup>10,11</sup> The broad band character of the fluorescence that is emitted when metal halides are excited in a low energy discharge have made them commercially useful in the lighting industry.<sup>13</sup>

Recent photo absorption measurements seem to agree on the general features of the absorption curves <sup>4,14,15</sup> but do vary somewhat as to the absolute magnitudes. The quantum efficiency measurement by Wilcomb, Burnham and Djeu<sup>14</sup> indicates a threshold for production of HgBr (B-X) emission of approximately 6 eV.

When  $\text{HgBr}_2$  is irradiated with light of various wavelengths, the resulting emission occurs in three bands which is typical of the metal halides.<sup>4</sup> The three absorption peaks occur in  $\text{HgBr}_2$  at wavelengths of 160 nm, 183 nm and 195 nm and produce fluorescence in the following bands: 250-270 nm, 270-290 nm and 350-505 nm, respectively.<sup>4,16,17</sup> It is the u.v. absorption peak at 195 nm (corresponding to 6.4 eV of energy) which directly populates the B state of HgBr by the dissociative excitation of  $\text{HgBr}_2$ . The absolute cross section for the formation of excited HgBr (B) has been measured by Allison and Zare.<sup>12</sup> The reported

cross section at 100 eV was approximately  $1.0 \times 10^{-19} \text{ cm}^2$  and the process was reported to have a threshold of about 25 eV which was determined from Figure 1 (b) of their paper. This determination of the cross section was too low to explain the laser formation efficiency of HgBr (B) in HgBr<sub>2</sub>.<sup>6</sup> It was not easy to reconcile the size of the cross section reported by Allison and Zare compared to the rather sizeable<sup>15,20</sup> photo absorption cross section.<sup>39</sup> In addition, the threshold value reported by Allison and Zare<sup>12</sup> of approximately 25 eV failed to explain the features of earlier photoabsorption and fluorescence efficiency measurements.<sup>14</sup>

A recent study of fluorescence produced by an x-ray sustained discharge in Xe/HgBr<sub>2</sub> mixtures indicated that another separate peak at lower energy than reported earlier existed for the formation of HgBr (B) by electron impact.<sup>18</sup>

The purpose of the present work was to measure the optical excitation cross section for the process shown below.

Process (1)      HgBr<sub>2</sub>+e<sup>-</sup> → HgBr (B) + products

and

HgBr (B) → HgBr (X) + photon (300 - 500 nm).

The optical cross section for the process (1) shown above was studied by monitoring the fluorescence produced by a low energy electron beam as it was directed into a region containing HgBr<sub>2</sub> at low pressure.

#### EXPERIMENTAL APPARATUS

The experimental apparatus (Figure 3-1) consists of a low energy (0-120 volts) electron gun in a bakeable high vacuum container (electron gun chamber), an optical monochromator and photomultiplier tube (PMT) to



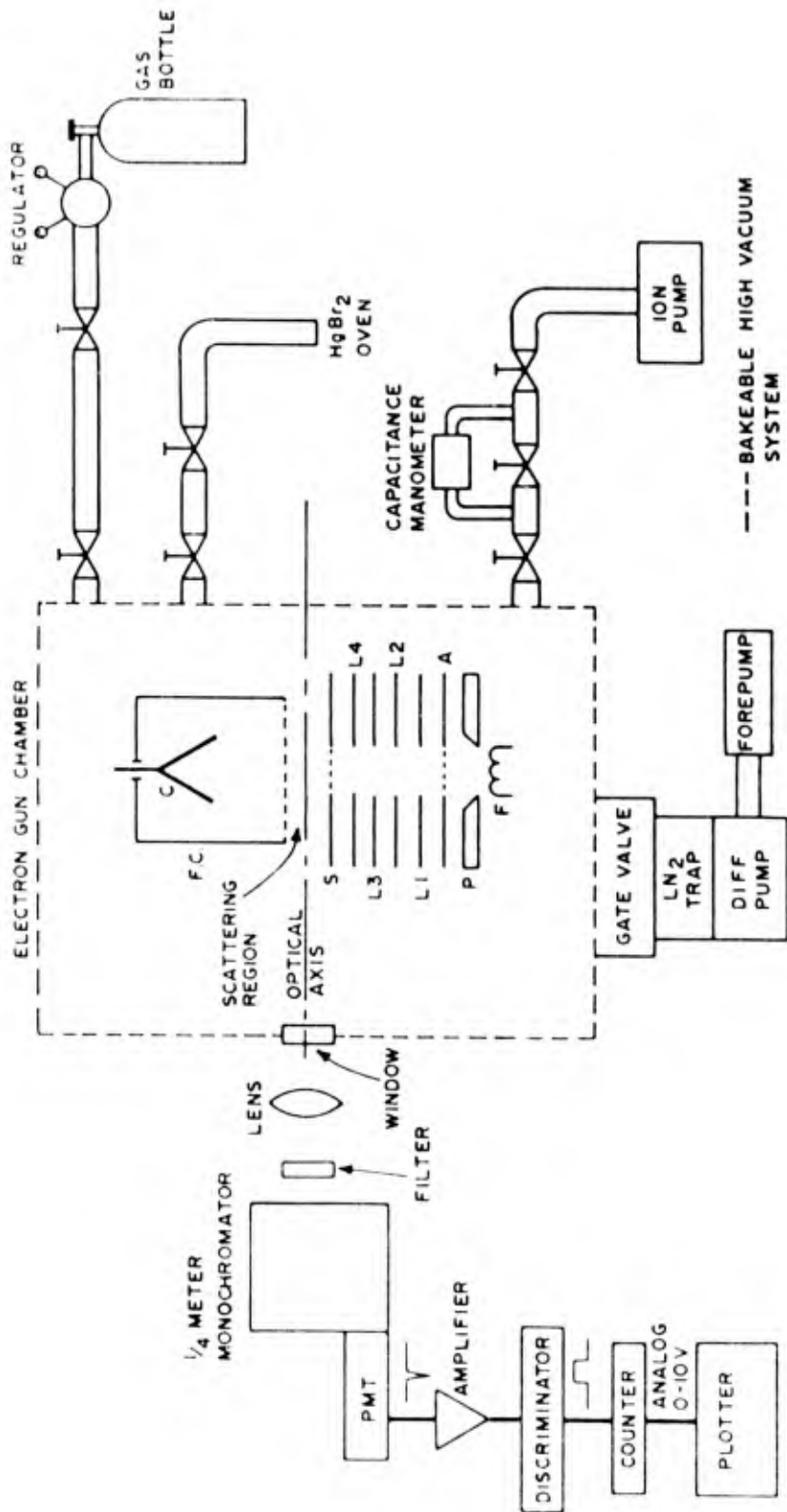


Figure 3-1 EXPERIMENTAL APPARATUS

filter and detect the light and electronic amplifiers, counters and data recording equipment. The chamber is about 15 cm in diameter and approximately 30 cm long.

The vacuum system is constructed entirely from 300 series stainless steel except as noted below. The Varian swing gate valve contains bearings made of high carbon steel; these are not exposed to the  $\text{HgBr}_2$  when the experiment is in operation. There are several Ceramaseal weldable feedthrus (MHV and BNC) installed on the top 8" conflat flange. These feedthrus contain a copper alloy braze as well as nickel alloys.<sup>26</sup> The Varian swing gate valve has one viton sealed flange and another viton seal on the main seal plate. As delivered from the manufacturer, the seal plate was an aluminum alloy. This was replaced by a 300 series stainless steel plate due to corrosion of the aluminum. A triode ion guage in a glass envelope is installed on the chamber and contains nickel alloys in addition to the iridium filament. No corrosion is evident on the guage even after months of running. All conflat flanges and cajon VCR type fittings utilize either copper or nickel gaskets which have been plated with rhodium and then gold plated. The rhodium serves the dual role of stopping the gold from diffusing into the base metal when the plated gasket is heated and the rhodium flash tends to keep the gold-plating solution clean during use. Gold plated copper gaskets were used early in the experiment but they corroded possibly due to the high solubility of copper in the plating solution.<sup>27</sup> The dissolved copper could be plated along with the gold producing a gold-copper alloy which would subsequently corrode due to the copper in the alloy being in contact with the  $\text{HgBr}_2$  vapor.

All stainless steel parts that contacted the  $\text{HgBr}_2$  either solid or gaseous were passivated<sup>44</sup> before use. The passivation process consisted of a thorough cleaning with detergents and solvents to remove oil and grease. This was followed by soaking in 20% nitric acid solution in distilled water for 5 to 20 minutes. Without this passivation step, the stainless steel in a short time would develop a dark green corrosion which was presumably nickel bromide. When the stainless parts were processed as outlined above no corrosion was evident even when left in contact with solid and gaseous  $\text{HgBr}_2$  for 6 months at a temperature of 180 °C.

There are two gas supply manifolds attached to the electron gun chamber. One is used to introduce He, Ar,  $\text{N}_2$ , etc. into the chamber. The second manifold contains approximately 10 grams of  $\text{HgBr}_2$ <sup>21</sup> and is heated to 180 C to produce  $\text{HgBr}_2$  vapor. The  $\text{HgBr}_2$  vapor is metered into the electron gun chamber. Valves on both gas manifolds allow full control of the gas flow including positive shut off.

The pressure in the electron gun chamber is measured by a MKS Baratron<sup>tm</sup> capacitance manometer. The entire apparatus is wrapped with heating tapes, and insulated with 1/4" thick fiberglass to maintain a uniform temperature. The reference side of the manometer is connected to a 0.2 liter/sec. Varian vac-ion pump. A Varian 6 inch gate valve is located at the bottom of the electron gun chamber between a liquid nitrogen trap and the chamber. The entire electron gun chamber is pumped by a Varian vhs-6 oil diffusion pump. During data collection, the gate valve is used as a throttle valve by adjusting the manual opening screw so that the valve plate is held slightly open allowing a continuous flow

of gas from the gas manifold through the chamber and out the gate valve. The flow arrangement is used to run wavelength spectra and relative optical excitation functions. The temperature of the apparatus is measured by three chromel alumel thermocouples located in the outside surface of the vacuum vessel and on the plate on which the electron gun is mounted.

During operation the entire vacuum chamber is heated to 90 C to decrease condensation of  $\text{HgBr}_2$  on the inside chamber surface. This decreases the exposure of internal parts to the  $\text{HgBr}_2$  in the solid form and decreases the possibility of corrosion. Experiments were performed with from 0.1 to 1.3 millitorr of gas pressure in the electron gun chamber.

The electron gun (Figure 3-2) is adapted from a design by Sharpton<sup>25</sup> and utilizes a directly heated thoria coated iridium filament, F, as the cathode. This material is one that will continue to emit electrons even in the presence of  $\text{HgBr}_2$  vapor. The cathode, Pierce element and anode are arranged in a modified Pierce arrangement. The Pierce, P, element has a 0.95 cm diameter aperture to match the length of the coiled iridium filament and the 0.95 cm aperture of the anode, A, is covered with a molybdenum mesh of 80% transmission.

The four focusing lens (L1,L2,L3,L4) of the gun are made from 1 mm thick 304 stainless steel plates which have 0.95 cm diameter apertures and are 4.06 cm square. The scattering region is defined by a grounded shield, S, with a 80% transmission moly mesh covered aperture and a grounded Faraday cup, FC, which contains the electron collector, C. The front opening of the Faraday cup is also covered with the metal mesh to

# ELECTRON GUN

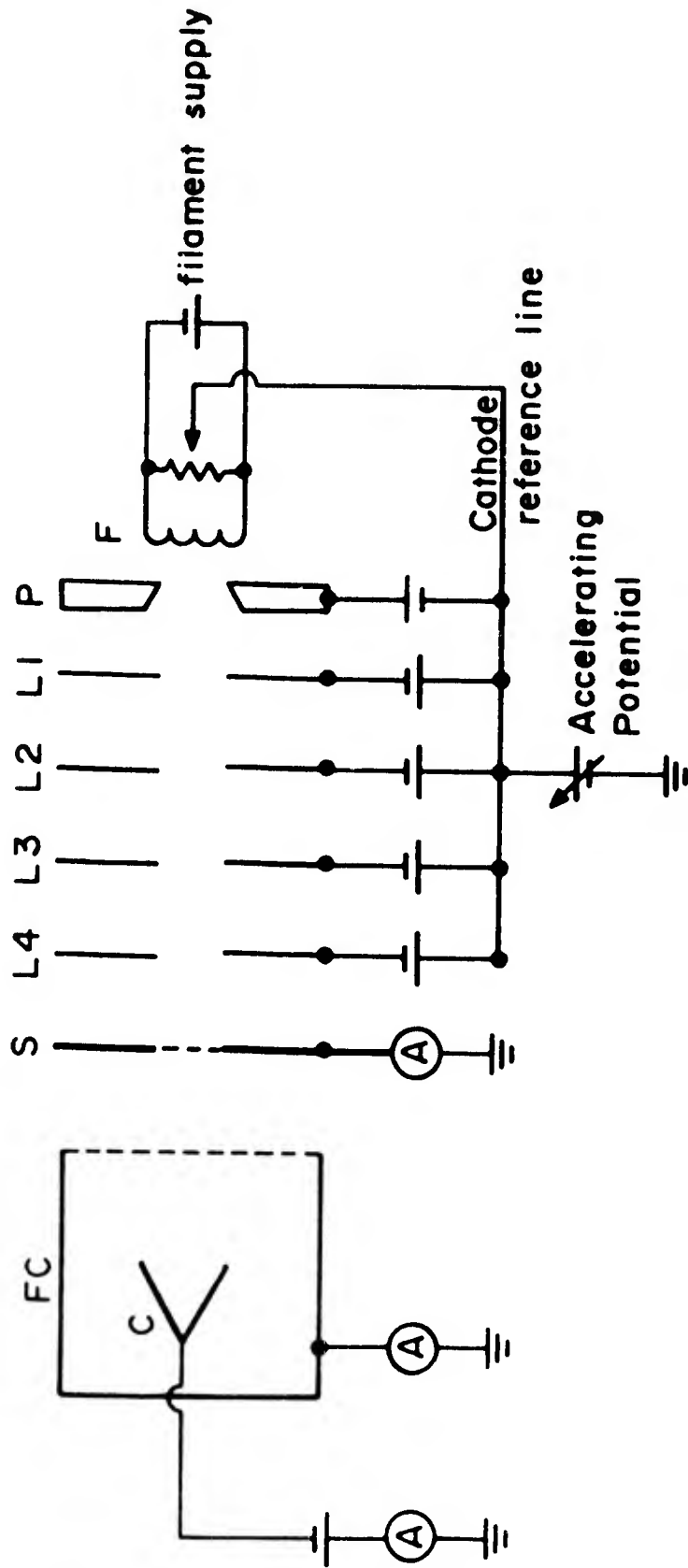


Figure 3-2 ELECTRON GUN

shield the scattering region from the bias potential applied to the collector. This bias potential increases the efficiency with which the electrons that enter the faraday cup are collected. Potentials on elements of the electron gun are referenced to the electrical center of the coiled iridium filament used for the cathode (Figure 3-2), except where otherwise noted.

The axis of the optical detection system is oriented at  $90^\circ$  to the electron beam. Light from the scattering region is focused onto the entrance slot of a Jarrell-Ash 1/4 meter monochromator by a quartz lens that is stopped by an aperture so that the lens f stop matches that of the monochromator. The monochromator slit is oriented so as to be perpendicular to the axis of the electron beam. The monochromator gratings are blazed at 5000 Å and 3000 Å and both have a linear dispersion of 33 Å/mm. The monochromator slits were selected to be 0.250 mm for optical excitation functions and wavelength spectra. This corresponds to a resolution of 8.2 Å in both the optical excitation functions and the wavelength spectra. A Corning colored glass filter CS 4094 (blue-green) is placed just in front of the entrance slit of the monochromator to reduce spectra in the second order for the collection of relative optical excitation functions in the wavelength range 450 to 500 nm. The wavelength spectrum presented here was taken without a filter to allow use of the 2537 Å Hg line in second order as a calibration point.

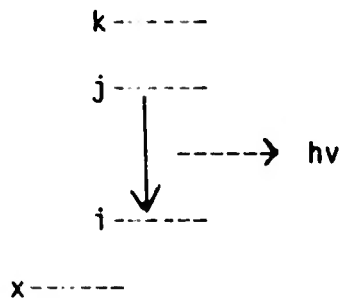
The wavelength of light that is selected by the monochromator is detected by a cooled RCA C31034 photomultiplier tube which has approximately 15 dark counts/sec with 1500 volts across the tube when the cathode is cooled to  $-25^\circ\text{C}$  in a Products for Research<sup>28</sup> pmt cooler.

The pulses from the photomultiplier tube are amplified, shaped and analyzed by a discriminator and counted in a digital counter which supplies an analog signal for the chart recording equipment.

METHOD

1. Level Excitation cross section and optical excitation cross section for a simple multiple level system.

Assume that a molecular system consists of a simple four level system consisting of levels in decreasing order of energy labeled k,j,i and x. These levels are shown schematically below. Assume that optical transitions between the pairs of levels kj,ji and jx are optically allowed.



The number of molecules in state j as a function of time is given by the expression

$$dn_j/dt = N q(j)I/e - A(ji)n_j - A(jx)n_j + A(kj)n_k \quad (3-1)$$

$n_j$  number per unit length along the electron beam of molecules in the state j -  $cm^{-1}$

N number density of gas molecules in the scattering region -  $\#/cm^3$

$q(j)$  level cross section for excitation by electron impact into the state j -  $cm^2$

I beam current of electrons in the scattering region - amp

e charge on the electron-coulomb

$A(ji)$  probability of radiative transtion per second from state  $j$  to state  $i$ -sec<sup>-1</sup>

If equilibrium assumed, then the time derivative is equal to zero in equation(3-1)

$$dn_j/dt = 0. \tag{3-2}$$

The expression that is left could be solved for the cross section  $q(j)$ . Following the discussion of Massey and Burhop<sup>36</sup>, the optical cross section,  $q(ji)$  is defined as

$$Nq(ji)I/e = A(ji)n_j \tag{3-3}$$

and similarly for the transitions  $kj$  and  $jx$ . Equations (3-1)-(3-3) assumes a collisionless system with no photon trapping of the emitted radiation. It can be seen that the level cross section and the optical cross section are certainly related but they are not in general equal. The reason is the additional loss mechanism for molecules in the state  $j$  that undergo a radiative transition to the state  $x$  and the gain of molecules in the  $j$  state due to molecules that have undergone a transition from the  $k$  state to the  $j$  state. The optical cross section only accounts for those molecules that undergo a transition from the state  $j$  to the state  $i$ . The level cross section relates to the total number of molecules that have been directly excited to the  $j$  level.



Using equation 3-2 and 3-3 in equation 3-1, results in an expression that expresses the level cross section in terms of an optical cross section and a transition from a higher level and a transition to a lower level

$$Nq(j)I/e = Nq(ij)I/e + A(jx)n_j - A(kj)n_k. \quad (3-4)$$

The second term on the right side of equation (3-4) is a loss term due to a transition to a lower state while the third term is due to transitions into the j state from a higher lying level. In the more general case, there are many higher levels and the contribution to the population of the j state is called the cascades. It is seen that a measurement of the optical excitation cross section alone is not sufficient to determine the level cross section. In addition, the flux of photons from all transitions originating or terminating on the j state must be measured.<sup>25</sup> This last statement can be demonstrated by noting that for every optical transition one photon is emitted. Recall that the light flux,  $F(ji)$ , due to a transition from the j state to the i state is given by the following expression

$$F(ji) = A(ji)n_j. \quad (3-5)$$

Where  $F(ji)$  has the units of photons/sec-cm. Substituting (3-5) into equation (3-4), results in equation (3-6) which shows the relationship between level cross section, the optical cross section and the flux of light due to molecules entering state j and exiting state j to any state other than the state i.

$$Nq(j)I/e = Nq(ji)I/e + F(jx) - F(kj). \quad (3-6)$$

A more realistic molecular system will include many more levels than the four level system that has been used here for demonstration. In the case where there are several energy levels which cascade into the level under consideration, the  $F(kj)$  term in equation (3-6) is replaced by a sum over all the higher energy levels. Similarly in the case where the level under consideration can undergo optical transitions to several lower energy levels, the single term  $F(jx)$  in equation (3-6) is replaced by a sum over all the lower levels.

## 2. Integrated Optical Emission Cross Section

$F(ji)$  in equation (3-5) is the flux of photons per unit length from the scattering region which corresponds to the transition from state  $j$  to state  $i$ . If the system (atom or molecule) can have several initial and final states which cause light to be emitted into the bandwidth of the optical detector then the total light flux which will be measured by the optical detector will be the sum of  $F(ij)$  over all of the initial and final states for which the wavelength of the resulting photon will be accepted by the detector. The initial fluorescence measurement on  $\text{HgBr}_2$  is a sum of all wavelengths that are within the optical detector bandpass which was centered on 502 nm. However, since the optical bandpass is narrow 0.82 nm compared to the emission band of the molecule (almost 250 nm), only a very small wavelength segment of the total spectrum is measured at any one time. It is for this reason that the spectrum must be integrated in order to determine the total light flux per cm. of

beam. This integral relates to the integrated optical cross section which will be shown next.

Under low energy electron impact,  $\text{HgBr}_2$  produces a band of fluorescence which appears to be continuous when observed at low optical resolution that emission extends from 300 nm to 500 nm. The transitions included in this emission band are between the same two electronic states, the B and X of  $\text{HgBr}$ , but between several different pairs of vibrational-rotational levels of these electronic states. The quantity of interest is the total number of molecules that are produced in the B state that undergo a transition to the X level with the subsequent emission of a photon. If equation (3-5) is substituted into equation (3-3) and the result solved for  $q(ij)$ , the following results

$$q(ji) = e/(NI)F(ji). \quad (3-7)$$

The integrated optical cross section is defined as the sum of  $q(ji)$  over all the possible initial states,  $j$ , and the possible final states,  $i$  that can result in optical transitions between the two electronic states  $\text{HgBr}(B)$  and  $\text{HgBr}(X)$ . The optical transitions between the initial and final states produce fluorescence in the  $B \rightarrow X$  emission band. This sum is replaced by an integral in the case of a continuous set of levels, Equation (3-8) expresses the integrated optical cross section,  $Q(B-X)$ , for the  $B-X$  transition of  $\text{HgBr}$  as a function of the photon flux per cm. of beam in the scattering region

$$Q(B-X) = e/(NI) \sum_{ij} F(ji). \quad (3-8)$$

Where  $j$  refers to rotational vibrational levels within the electronic state B of HgBr and  $i$  refers to rotational vibrational levels within the electronic state X of HgBr. In order to determine the integrated optical cross section, the flux of light of the proper wavelengths from the scattering region must be measured. The wavelength region of interest is determined by all the optical transitions that connect the two electronic states the B and the X state of HgBr.

For HgBr<sub>2</sub> the range of interest is for upper vibrational levels of from 0 to 20 and lower vibrational levels of from 0 to 33.<sup>3,29</sup> Lasing has been reported near 5018 and 4996A by Parks<sup>30</sup> and at 5020 and 5040A by Schimitschek and co-workers.<sup>1</sup> Refer to Tellinghuisen and Ashmore<sup>29</sup> and references therein for assignments of spectral lines to specific vibrational transitions.

In the present work, we are reporting a cross section at a given electron energy over a narrow bandwidth of fluorescence as well as a cross section at that same electron energy but integrated over the entire emission band of the HgBr(B-X) transition. There are two reasons for reporting both a narrow band optical cross section and an integrated optical cross section. The narrow band cross section is closer to the actual lab measurement and thus is not dependent on the calibration sensitivity of the optical detection system over a wide wavelength range but only includes the sensitivity calibration at the wavelength of the measurement (i.e 502 nm). If one can assume that all the upper levels

can be efficiently relaxed by the buffer gas in an electrical discharge laser then the level cross section integrated over the entire emission band is a quantity that could be used to model a discharge laser. After making some assumptions about the cascades into the B state of HgBr and the branching ratios, it is possible to determine a reasonable estimate of the integrated level cross section for the B state from the integrated optical cross section. It is clear from the discussion above that if all the levels higher in energy than the upper laser level are not relaxed into that level then an adjustment must be made in the integrated level cross section before it is used in any model.

### 3. Electron Gun

#### a. Beam current vs accelerating voltage:

The electron gun was subjected to extensive testing before it was actually put into use. One of the most important characteristics of any electron gun is the change of beam current as the accelerating voltage is changed. If the beam current is not fairly constant then this can change many parameters of the experimental setup such as beam size, space charge effects, location of focus, etc. In the region of from 0 to 6 volts accelerating potential, the beam current increased slowly and reached an almost flat plateau increasing 10% in the range of accelerating potential from 7 to 20 volts. Shown in Table 3-1 is a typical set of data for the beam current versus the accelerating potential. The exact shape of the curve depends on the voltages on each lens element and the condition of the cathode but the data presented is representative of a set-up that took a reasonable amount of time to accomplish.

TABLE 3-1 BEAM CURRENT VERSUS ACCELERATION VOLTAGE

-----  
 accelerating voltage:

1.36 3.00 4.00 5.00 6.00 7.00 8.00 10.0 15.0 20.0 100

beam current, microamps:

0 15.3 22.11 26.2 28.8 30.6 31.2 31.8 32.7 33.5 37.3  
 -----

data run: 1400 30 June 82

b. Florescence signal vs pressure

Data is shown in Figures 3-3,3-4 showing the fluorescence signal versus gas pressure of HgBr<sub>2</sub> and He. This type of data is collected in order to insure that the experiment is operating in the single collision region. The transition out of the single collision region is evidenced in Figure 3-3 for HgBr<sub>2</sub> pressures greater than approximately 0.5 millitorr by the deviation of the data from the straight line which has been fitted to the data collected below 0.5 millitorr. The single collision region requires that any electron in crossing the collision region has a small probability of suffering a single collision and a very much smaller probability of having two collisions. The probability, P(x), that an electron will have a collision with a molecule in traveling a distance x through a region containing a gas of density N is given by the following expression:

$$P(x) = \exp(-NQX)$$

where Q is the total collision cross section for electrons on the gas at

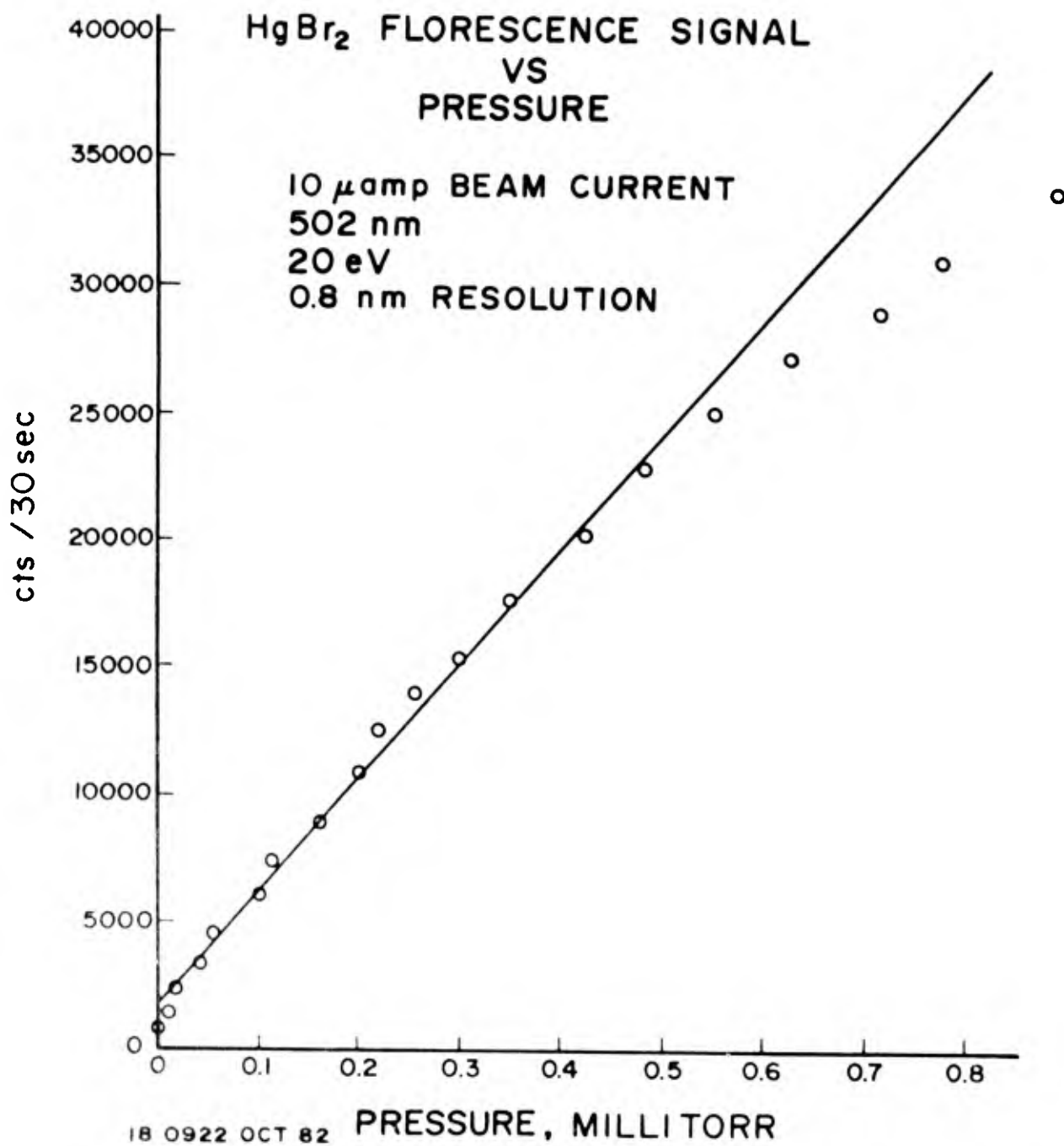
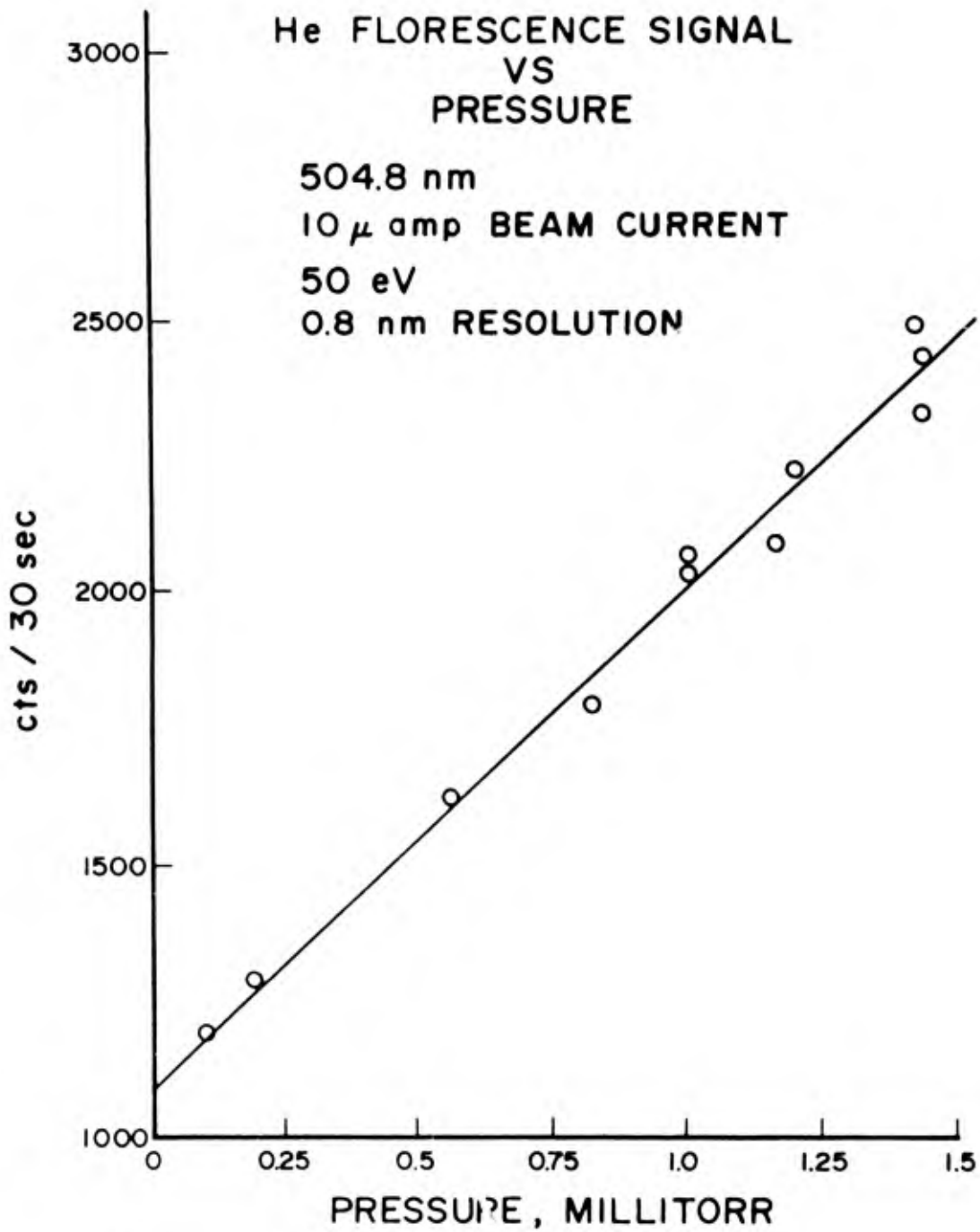


Figure 3-3



13 1250 OCT 82

Figure 3-4



some energy and  $N$  is the gas density in the scattering region. Some typical values are  $N=1 \times 10^{+13} \text{ cm}^{-3}$  (for a pressure of 0.26 micron and a temperature of 25 C),  $Q=1 \times 10^{-16} \text{ cm}^2$  and for the length of the scattering region  $x=1 \text{ cm}$  this gives a probability of  $P(x)=0.001$  and the probability of two collisions within the collision region would be  $P_2(x)=1 \times 10^{-6}$ . Thus for the case outlined above, it is reasonable to assume single collision conditions.

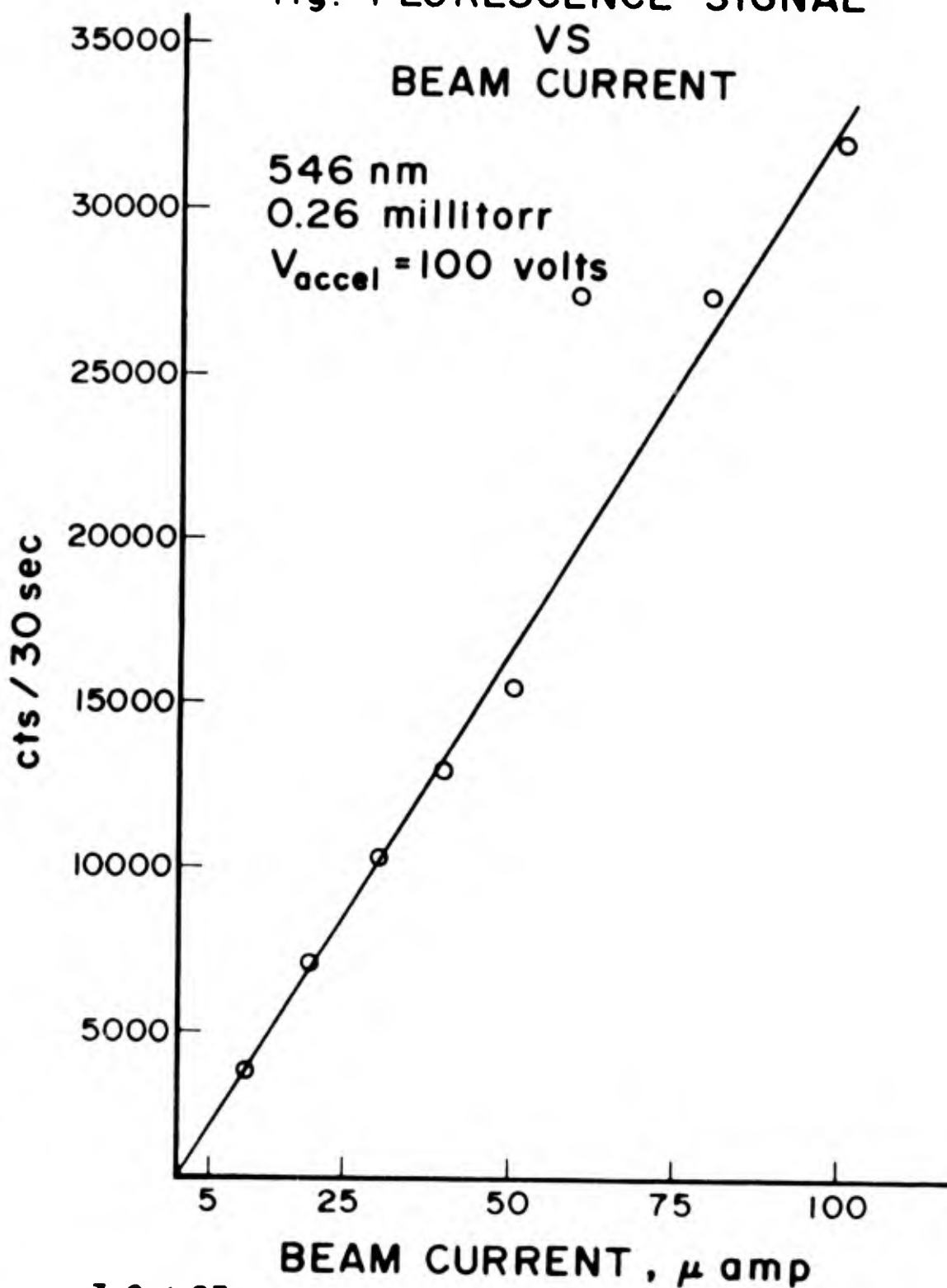
c. Florescence signal vs beam current and shape of a known excitation function:

A measurement of the florescence signal at 5460 A versus the beam current at constant pressure was performed. (Figure 3-5) This emission line is produced by electron impact on  $\text{HgBr}_2$  with the production of the  $\text{Hg}^*$  which leads to the 5460 A spectral line of Hg. The purpose of this experiment and the one in which signal versus pressure at constant beam current is recorded was to identify the limits of the region where the signal is a linear function for this transition of both the gas pressure and the beam current. Equation (3-1) is only valid in this linear region so it is important to confine the operation of the experiment within the limits of this region. Since the entire data analysis is based on equation (3-1), operation outside these limits would invalidate the analysis. Outside of the linear region, processes such as molecule-molecule collisions, photon trapping and multiple electron scattering become important in the case of high pressure. For operation with high beam currents, space charge effects become important and must be considered in the data analysis.

The florescence signal vs pressure (constant beam current) for several values of beam current were measured. The florescence signal

Hg. FLORESCENCE SIGNAL  
VS  
BEAM CURRENT

546 nm  
0.26 millitorr  
 $V_{\text{accel}} = 100$  volts



3 Oct 83

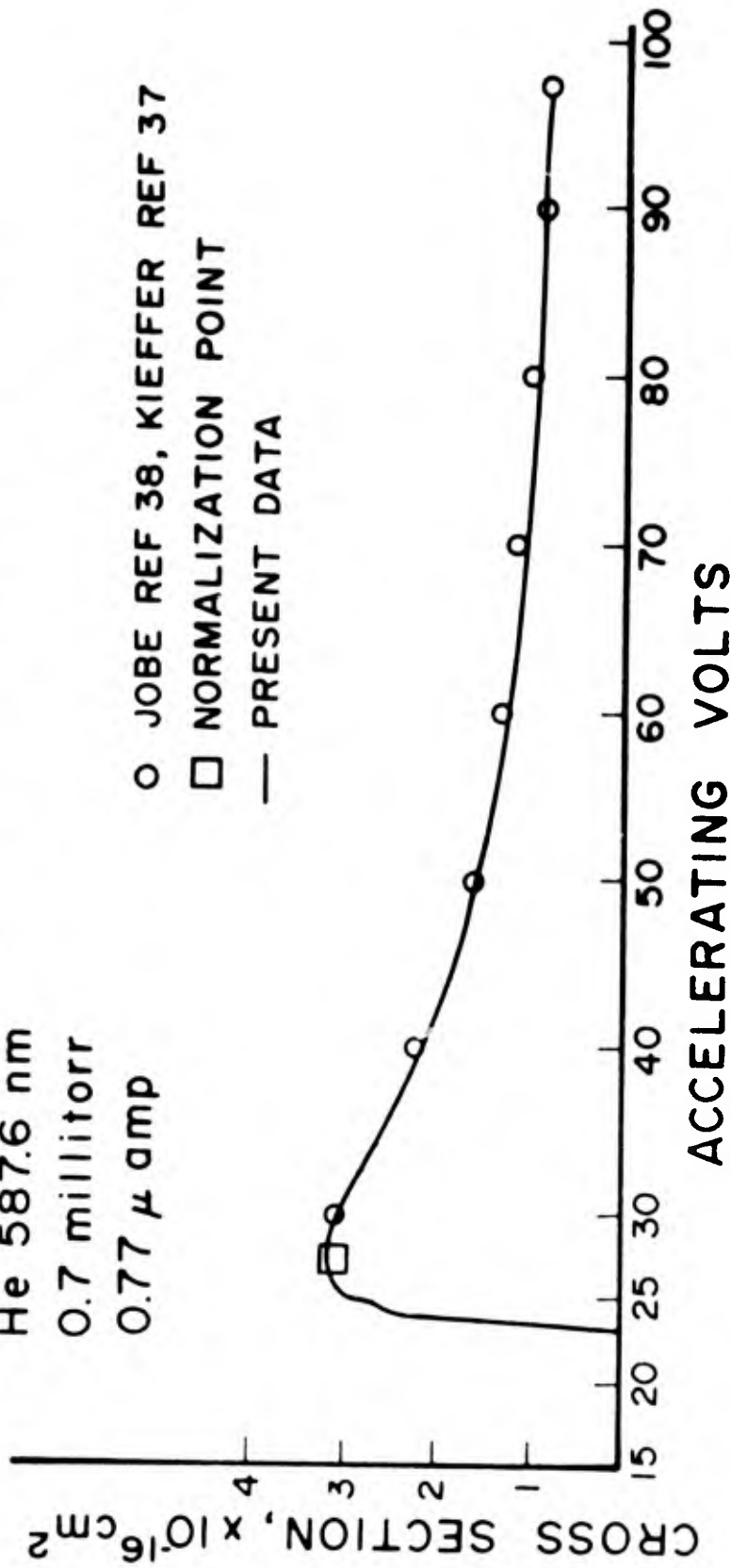
Figure

vs beam current at constant pressure for several pressures was also measured for both He and HgBr<sub>2</sub>. In the case of He the wavelength was set to detect the 504.8 nm line of He so that the results of Van Zyl, et al.<sup>24</sup> could be used to calibrate the relative optical excitation function taken in HgBr<sub>2</sub> at 502 nm. The work of Van Zyl, et al has been used as a standard due to their careful control of the experimental variables especially the temperature of the blackbody source which was the primary standard used to calibrate their optical system. For HgBr<sub>2</sub>, 502 nm was chosen since it was the peak in the wavelength spectra. The optical detection system, lens, blue green filter and all stops wavelength resolution and optical alignment were maintained constant for the He and HgBr<sub>2</sub> measurements.

The ability of the apparatus to accurately record the shape of the optical excitation function was tested by measuring the relative optical excitation function of He ( $3^3P \rightarrow 3^3D$ ) at 5876 Å. The measured optical excitation function was compared to the shape of the excitation reported by Jobe<sup>38</sup> and Kieffer<sup>37</sup> by normalizing the vertical and horizontal scales at the peak of the two optical excitation functions and comparing how the two curves matched at other points. The data is shown in Figure 3-6 the solid recorder trace being the present data normalized at the peak to the data of Jobe<sup>38</sup> representative points of which are shown in the closed circles. The agreement was found to be satisfactory throughout the range of accelerating voltages of interest. The small shoulder just above the threshold of the He (5876 Å) relative optical excitation probably corresponds to a resonance which has been reported by Jobe as appearing at 23.7 eV. The agreement at high energies

OPTICAL CROSS SECTION He ( $3\ ^3D-2\ ^3P$ )

He 587.6 nm  
 0.7 millitorr  
 0.77  $\mu$  amp



8 1301 Aug 82

Figure 3-6

above the peak demonstrates that effects such as secondary emission due to the electron beam hitting apertures and screens is not a problem in this apparatus in the energy range above 23 eV. There was very little shift in the energy scale which was determined by comparing the appearance potential and the energy of the threshold reported by other workers. Even if this effect is not present in one gas, this does not guarantee that the effect will not be present in other gases. It is reassuring that any contact potentials in He, if present, were small (meaning less than 0.2 eV).

To insure that space charge effects in the electron beam did not affect the shape of the  $\text{HgBr}_2$  optical excitation functions the beam current in the scattering region was varied by lowering the temperature of the directly heated cathode by changing the current supplied to the heater. The heater current was varied from 2.3 amps at 8 volts to 2.0 amps in several steps and recording the optical excitation function at each power setting. At each cathode power setting the gun lens voltages were tuned and an optical excitation function recorded. Emission functions were also recorded at fixed cathode power and for several combinations of lens voltages again to compare the shape of the  $\text{HgBr}_2$  optical excitation function in each case. The shape of that portion of the optical excitation function above 6 eV did not change shape or threshold in any of the cases studied. In the region extending from disappearance of beam current, up to an electron energy of 6 volts, the width of the peak which appeared at approximately 2.5 eV could be varied. For a further discussion of this small peak see the results section. This effect is probably due to changing the energy resolution

of the electron beam. Particularly effective in causing this effect was the choice of Pierce element and anode potential. Generally the Pierce/anode voltage combination which produced the greatest beam current produced the lowest energy resolution and vice versa. The energy resolution was determined by applying a retarding voltage to the shield element, S, and recording the beam current as a function of the retarding potential on the shield. In the case of the data presented in this paper, the gun was always tuned to give the highest possible energy resolution (1 eV). This is rather low energy resolution and is probably due to the voltage drop across the emitting region of the directly heated cathode.

4. Calibration of the optical detector at 504.8 nm and calculation of the narrow band optical excitation function at 502 nm in  $\text{HgBr}_2$ :

The fluorescence signal measured by the optical detector is a function of the pressure of  $\text{HgBr}_2$  in the scattering region, the wavelength,  $\lambda$ , the temperature of the gas, T, and the beam current, I, as well as the detector sensitivity and geometrical factors due to the arrangement of the detection system. The fluorescence signal for  $\text{HgBr}_2$  is given by the expression

$$S(\text{HgBr}) = (G(\lambda)q(\text{HgBr})i(\text{HgBr})P(\text{HgBr})/T(\text{HgBr}))+B(\lambda). \quad (3-9)$$

Where  $G(\lambda)$  includes the detector sensitivity, transmission of the optics and monochromator, geometrical factors and a constant due to the conversion of density to pressure.  $G$  is assumed to remain constant from the  $\text{HgBr}_2$  measurement to the He measurement.  $T$  is the temperature of the gas in the scattering region. The beam current, I, and the pressure,

P, can vary from one experiment to the other so they are shown as functions of the particular gas. B(1) is the signal due to background counts from the photomultiplier tube and it is assumed constant from one run to the next. The optical cross section q (HgBr) is the cross section at 502 nm slits on a grating with a linear dispersion of 3.3 nm/mm. The value for the optical bandwidth, 0.8 Å, was determined by actually measuring the width on a chart record of the Hg 5460 Å line in the HgBr<sub>2</sub> spectra and using the known lines of Hg to calibrate the wavelength scale. Solving equation (9) for q (HgBr)

$$q(\text{HgBr}) = (S(\text{HgBr}) - B)T(\text{HgBr})/GI(\text{HgBr})P(\text{HgBr}). \quad (3-10)$$

A similar equation holds for the case of He

$$q(\text{He}) = (S(\text{He}) - B)T(\text{He})/GI(\text{He})P(\text{He}). \quad (3-11)$$

Solving the last two equations for q(HgBr), the following is obtained

$$q(\text{HgBr}) = q(\text{He})(S(\text{HgBr}) - B)I(\text{He})P(\text{He})P(\text{He})T(\text{HgBr}) \\ (I(\text{HgBr})P(\text{HgBr})(S(\text{He}) - B)T(\text{He})). \quad (3-12)$$

The measurement of q (HgBr) was accomplished by measuring the signal, S, versus the gas pressure at constant beam current. The equation  $S = AP + B$  was fitted to the data and the slope and intercept, B, which is the background counts are determined for each gas. Several of these runs were made for both gases, each run comprising about ten points. A plot of the data for HgBr<sub>2</sub> and He are shown in Figures 3-3 and 3-4 respectively. Once the constants A and B are known, the values for the ratio,  $Rat = (S - B)/IP$ , and the optical cross section q(He) are plugged into equation (3-12). The temperature was 90 C for both the He and HgBr<sub>2</sub> data runs. The value for this He cross section has been taken from the recent work of Van Zyl, Dunn and Heddle.<sup>24</sup> The

value of  $8.08 \times 10^{-20} \text{ cm}^2$  at 50 eV for the He line 504.8 nm which corresponds to the transition  $4^1S \rightarrow 2^1P$  has been used for the variable  $q(\text{He})$ . The average value of the ratio for  $\text{HgBr}_2$  is  $\text{Rat}(\text{HgBr})=143.7$  counts/sec-micron-microamp and the value for He was calculated to be  $\text{Rat}(\text{He})=3.08$  counts/sec-micron-microamp. These last two values are determined from the measurements of fluorescence signal versus the gas pressure. The temperature in both cases is the same and thus cancels. A value of  $q(\text{HgBr})=3.77 \times 10^{-18} \text{ cm}^2$  at an electron energy of 20 eV was calculated using equation (3-12). This measurement in  $\text{HgBr}_2$  was taken at 502 nm with an optical bandpass of 0.82 nm full width at half max(FWHM). The same bandpass was used for the He measurement with a wavelength of 504.8 nm. Both measurements used the same optical set-up which included a Corning CS 4-94 blue-green filter to reduce the signal from second order.

The energy scale of the electron gun was calibrated by noting the difference between the value of the accelerating potential at the threshold of the  $B \rightarrow X$  transition in  $\text{HgBr}$  at 502 nm and the value in the energy of that same threshold that has been previously observed<sup>20,32</sup> and calculated.<sup>16,19</sup> The threshold of the transition appeared at an accelerating potential of 7.5 volts and the energy of the threshold has been reported as 6.1 eV  $\pm 0.2$  by various workers. Most of the shift in the energy scale in the present experiment can be accounted for in contact potentials in the electron gun and potential drops across the directly heated cathode. Since a directly heated cathode is used, there is a voltage drop across the area from which electrons are emitted of up to 8 volts. By proper adjustment of the voltage on the Pierce



element and the anode, the area from which electrons are extracted from the cathode can be limited thus avoiding most of the broadening of the electron energy distribution that would occur if all the electrons emitted from the cathode were to be accepted by the electron gun optics. The zero of the energy scale is assumed to be the point where the beam current decreases to zero. Between 0 eV (zero beam current) and 6 eV, there were no convenient energy calibration points which could be used in the present experiment to check the linearity of the energy scale. It is for this reason as well as the energy resolution of the beam that we estimate the error the energy calibration below 6 eV to be within  $\pm 1.0$  eV. It was possible to use another gas and calibrate the energy scale but this would not necessarily calibrate the scale for  $\text{HgBr}_2$ . The reason for this is that the electron gun is immersed in the gas that is being studied. This configuration has the advantage of providing a simple and direct determination of the pressure in the scattering region. As far as we know, the present experiment is the only one set up for  $\text{HgBr}_2$  that has an absolute pressure measurement by a capacitance type manometer. At the same time, the gas can interact strongly with the electron gun especially the hot cathode in the case of  $\text{HgBr}_2$ . This interaction can cause severe differences in the way the lens voltages must be set in order to focus the beam over a wide range of accelerating potential for different gas species. This effect was certainly observed in the present experiment. The contact potential for He was less than 0.5 eV but for  $\text{HgBr}_2$  it was estimated to be greater than 1 eV; the lens voltages for the two gases were also very different.

The beam current was monitored using a Hewlett Packard micromicroammeter and recording the analog output on a chart recorder. By recording the optical excitation function and the beam current simultaneously, the fluorescence signal can be normalized to beam current. Also, it can be determined that no abrupt changes in the focal position of the beam in the scattering region are taking place as the accelerating voltage is changed. In all cases, the data presented in this paper are raw data which are uncorrected for changes in beam current. This correction was not made since above the threshold of the HgBr(B) state the beam current was a slowly increasing function of the accelerating potential.

#### 5. Operation of the system

In the flow mode, the time required for a complete change of gas in the gun chamber was about 10 to 20 seconds. The flow mode was necessary due to the length of data runs (20 minutes to 3 hours) and the gas load from the walls of the apparatus. Gas load from the chamber walls was probably due to reactions of dissociation products of HgBr<sub>2</sub> with the stainless steel walls. In the flow setup, the valve used to throttle the gas flow from the electron gun chamber was adjusted so that the pressure due to gas load from the walls was less than  $1 \times 10^{-6}$  Torr. The resulting contamination was thus chosen to be three orders of magnitude lower in pressure than the HgBr<sub>2</sub> sample. The fluorescence due to the background gas was not detectable by the optical detection system with the throttling valve adjusted as described above. Although a detailed analysis of the background gas was not attempted, a wavelength spectrum at an electron energy of 100 eV was made to insure that there

were no leaks to atmosphere in the vacuum system. There was no  $N_2^+$  spectrum evident but Hg line spectrum was present after several months of normal operation of the apparatus. In addition to checking the background gas for nitrogen ion spectra, the entire vacuum system was He leaked checked several times through the course of the experiment using a VEECO<sup>tm</sup> brand He mass spectrograph leak detector.

## RESULTS AND DISCUSSION

### 1. Wavelength Spectra:

The wavelength spectra taken at an electron energy of 100 eV shows the three distinct emission bands which are typical of metal halides.<sup>4</sup> In addition the emission spectrum of atomic mercury is present. There are probably two sources of mercury spectrum in this experiment. First, after some hours of operation, free mercury could collect on the interior surfaces of the stainless steel vacuum system. Although we have observed no free Hg inside our apparatus background gas wavelength spectrum at fixed electron energy show definite mercury atomic spectra. Background gas is the gas load from the walls of the vacuum container. All vacuum systems have this gas load.<sup>34</sup> It can be difficult to detect this gas without a throttling valve between the vacuum pump and the vacuum chamber in an electron beam/fluorescence experiment unless a very strong optical transition is observed. Fortunately in the present experiment, such a valve was installed and by almost closing this valve a sufficient pressure of background gas could be collected in an hour or so in order to measure wavelength spectra or optical excitation functions. In addition to background gas, a second source of excited mercury could be

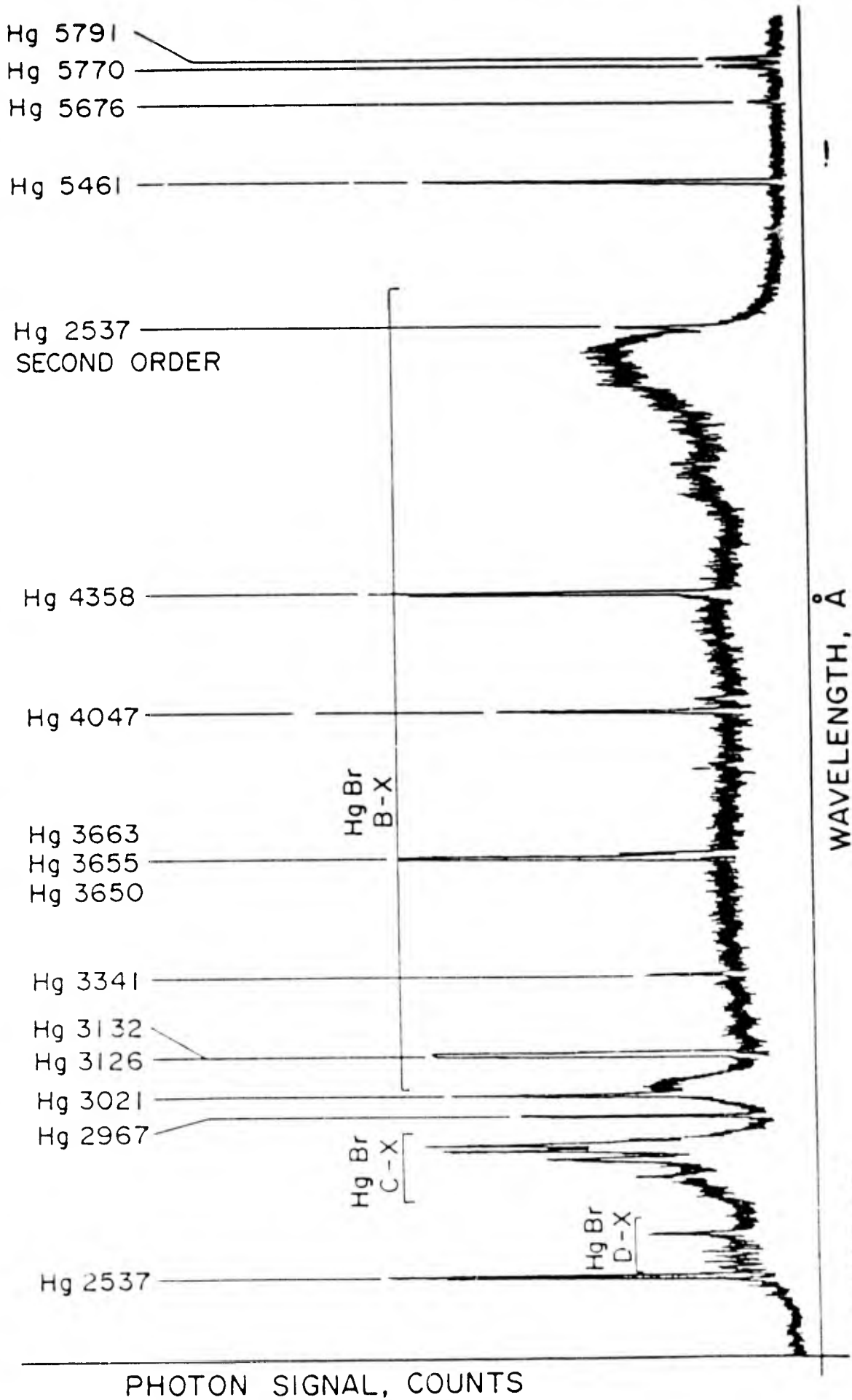


Figure 3-7 HgBr<sub>2</sub> FLUORESCENCE FOR THE PROCESS  
 e- + HgBr<sub>2</sub> -- HgBr\* + Br AND HgBr\* -- HgBr + PHOTON  
 100eV 90°C 1 mtorr HgBr<sub>2</sub> RESOLUTION 0.33nm

the dissociative process of electron impact on  $\text{HgBr}_2$ . This dissociative process could be a one step process which directly produces  $\text{Hg}^*$  or a two step process which produces Hg in the ground state which is then excited in a separate process such as collision with an electron or other particle thus producing  $\text{Hg}^*$ . The wavelength spectra was taken with no long wavelength filter in the optical path. This allows the second order 2537 A mercury line to appear at 5074 A and was used as a calibration point on the wavelength scale.

## 2. Optical cross section at 502 nm:

The cross section for production of fluorescence at 502 nm by electron impact on  $\text{HgBr}_2$  was put on an absolute scale by comparing it to the 504.8 nm fluorescence of He. The cross section measurements for production of fluorescence by He under electron impact of Van Zyl, Dunn and Chamberlain<sup>24</sup> have been compared to the fluorescence in the present experiment by measuring the fluorescence signal as a function of pressure. The results of these measurements are shown in Figures 3-3 and 3-4. The optical cross section for production of fluorescence in a 0.82nm bandpass centered on 5020 A by  $\text{HgBr}_2$  due to dissociative excitation by 20 eV electrons was determined to be  $3.8 \times 10^{18} \text{ cm}^2$ . This result is uncorrected for the effects of polarization of the fluorescence.

The signal as a function of beam current (Figure 3-5) was also measured to insure operation in the linear region free from the effects of space charge, collision effects and photon trapping. (see methods section for a full discussion) The advantage of using another cross section measurement as a calibration is that most of the geometric

factors and detection efficiencies of the optical detection system cancel in the analysis. The only stipulation is that all characteristics of the detector system, geometrical factor, detection efficiencies and transmission coefficients of optical elements, etc. must remain constant from one run to the next.

### 3. The optical excitation function:

Figure 3-8 shows a scan of fluorescence signal at 502 nm as a function of electron energy. The data above the threshold show a rather steep slope which is about 1 eV in total length along the horizontal axis; there are some small oscillations just at the end of the steep slope. A region that is almost flat extends beyond the steep slope to at least 30 eV. The energy of the threshold has been calibrated using the results of two independent experiments from other laboratories.<sup>32,33</sup> The relative excitation functions were normalized by shifting the entire curve horizontally until the threshold values occurred at an energy of 6.0 eV. In the raw data the threshold appeared at an accelerating potential of approximately 7.5 volts. The only change that has been made on the horizontal axis was to shift the entire excitation function 1.5 volts to the left; no other changes have been made to that scale. This normalization can be considered the calibration of the energy scale. The electron scattering work of Spence and Dillon<sup>33</sup> identify a  $^1\Sigma^+$  state. They have not reported a threshold for this state but from visual examination of the data presented by Spence and Dillon it appears to be just above 6 eV. say 6.1 or 6.2 eV. The  $^1\Sigma^+$  state has been identified as the state of  $\text{HgBr}_2$  that dissociates into  $\text{HgBr}$  (B) state<sup>16,19,23</sup> and which leads to fluorescence in the B-X band of

EXCITATION OF  $\text{HgBr}_2$   
 $\text{HgBr(B)}-\text{HgBr(X)}$  FLUORESCENCE  
502 nm  
0.5 mtorr

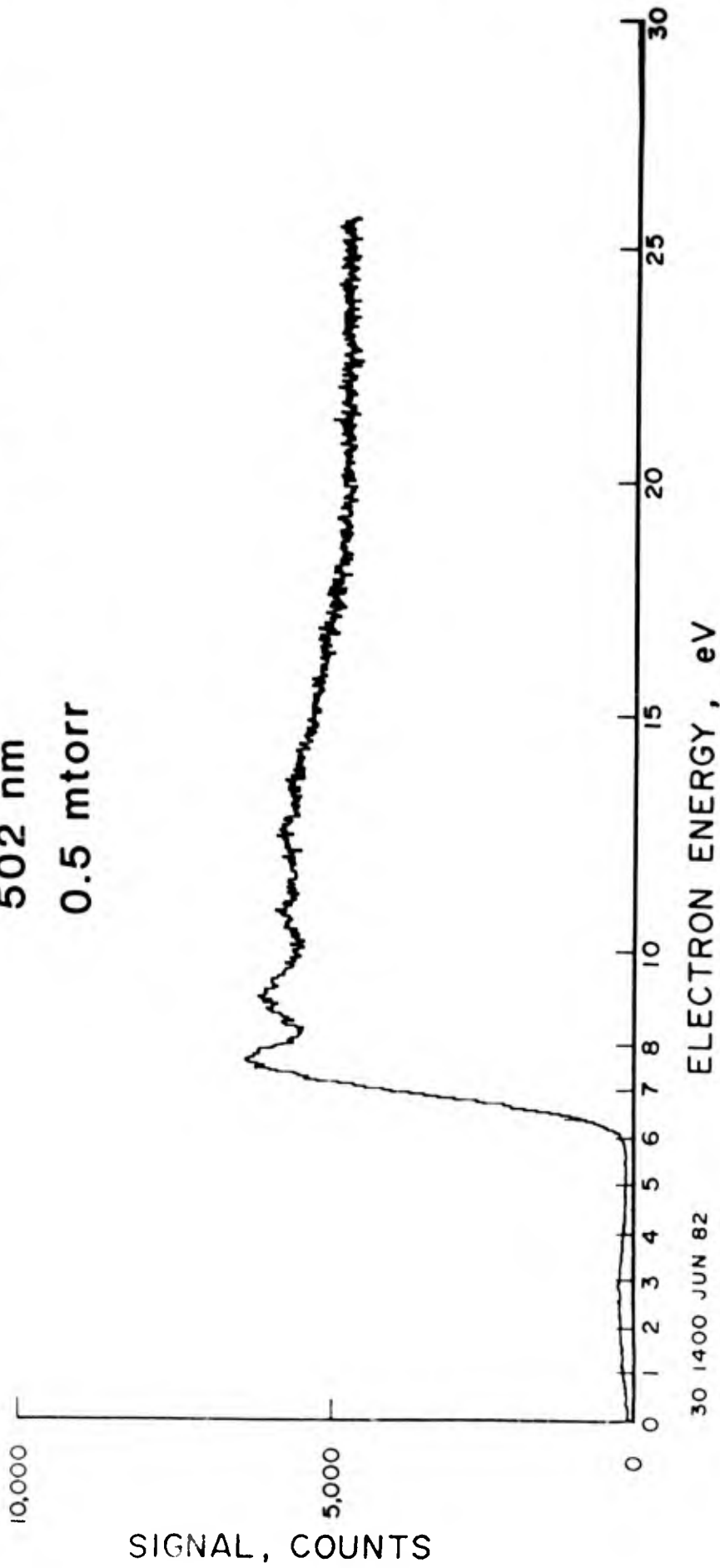
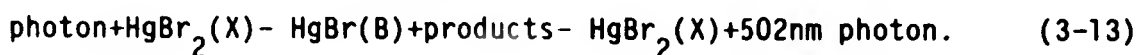


Figure 3-8 EXCITATION OF  $\text{HgBr}_2$   $\text{HgBr(B)}-\text{HgBr(X)}$  FLUORESCENCE  
502 nm 0.5 mtorr

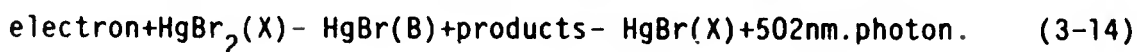
HgBr. It is then assumed that the state that Spence and Dillon observed at about 6.1 eV is the state that leads to the 502 nm HgBr(B-X) fluorescence that was observed in the present experiment. The photoabsorption cross section measurements of Wilcomb, Burnham and Djeu<sup>14</sup> in Figure 1 of that paper shows an absorption cross section that appears to have a threshold at about 210nm which corresponds to 5.9 eV and with a peak at around 200 nm (6.2 eV). Wadt in his recent structure calculations of HgBr<sub>2</sub> and HgBr<sup>16,19</sup> calculated the energy of the  $1^1\Sigma^+$  as 5.97 eV.

It is not clear at this time whether the entrance and exit channels for the two processes of 13. and 14. shown below are the same. In order to relate the threshold for production of HgBr<sub>2</sub>(B-X) fluorescence of the two experiments (photodissociation vs. electron impact), it is first necessary to know the pathways of the two reactions.

photodissociation



electron impact dissociative excitation



The recent work of Chen and Chanry<sup>32</sup> indicates that the threshold for process 14 above should be lower than indicated in the photoabsorption work of Maya.<sup>4</sup> All of the optical excitation function data presented here has had the threshold normalized to 6.0 eV.



The optical excitation, presented here, is the sum of several vibrational transitions due to the finite bandpass of the optical detection system and the nearly continuous emission band of  $\text{HgBr}_2$  when viewed at the resolution used in the present experiment (0.82 nm). The data shown in Figure 3-8 is the optical excitation function integrated over the monochromator bandpass.<sup>22</sup> It is important to specify the value of this bandpass for each measurement since in the case of  $\text{HgBr}_2$  the fluorescence signal is almost directly proportional to the monochromator bandpass due to the band nature of the fluorescence. A cascade analysis has not been undertaken and for these reasons it is not possible to calculate a total level cross section<sup>22</sup> from the present data. It would be easy by making certain reasonable assumptions about possible cascade contributions and transitions to other lower states to estimate the level cross section. The slope above the 6.0 V threshold is steeper than might be expected for an optically allowed transition.<sup>6,22,25</sup> This may imply that there is a channel for production of  $\text{HgBr(B)}$  that goes via a triplet level in  $\text{HgBr}_2$ . Since the structure calculations of Wadt<sup>16,19</sup> included no mention of a triplet state near 6 eV., there may be no triplet level in this energy range which could act as the intermediate state in the dissociation process. In addition, the measurements of the degree of polarization of light emitted by  $\text{HgBr}_2$  undergoing photodissociation by polarized light of Husain, Wisenfeld and Zare<sup>23</sup> indicate that the identification of the state preceding the formation of  $\text{HgBr(B)}$  is the  $1^1\Sigma^+$  the energy of which was calculated by Wadt.<sup>16,19</sup>

The recent modeling of an e-beam sustained discharge in  $\text{HgBr}_2$  /nobel gas mixtures by McGeoch, Hsia and Klimek<sup>6</sup> assumed that the fluorescence process with a 6.0 eV threshold had a peak at approximately 4 times the threshold energy. The present results would indicate the shape of the 6 eV cross section should be adjusted.

4. Calibration of the relative sensitivity of the optical detector as a function of wavelength:

The calibration of the optical detector over a wide wavelength range is carried out by comparing the detector signal as a function of wavelength from a tungsten light source to the theoretical shape calculated by measuring the temperature of the source and using the blackbody curves for the given temperature. The theoretical shape of the fluorescence signal versus wavelength is then calculated by the blackbody formula using the experimental values of the emissivity of a tungsten radiator by DeVos.<sup>31</sup> The temperature of the tungsten radiator was measured by a Leeds and Northrup optical pyrometer. Since these pyrometers are calibrated against a blackbody, the temperature must be corrected to a true temperature knowing the emissivity of the radiating surface.<sup>31,40</sup> By comparing the shape of the actual signal that the optical detector produces as a function of wavelength to the theoretical curve, the relative response function of the detector is calculated. The relative detector response is put on an absolute scale by calibrating the response at one wavelength. This was done by using the calibration of the He line at  $504.8 \text{ nm}^{24}$  as discussed above. A BASIC computer program, called SPECI, will calculate the response of the optical system as well as the integrated optical cross section if the optical cross

section at one wavelength is known. The program also requires a digitized wavelength spectra of a tungsten radiator at a known temperature and one of  $\text{HgBr}_2$  entered on the appropriate lines in DATA statements. The wavelength spectra of a  $\text{HgBr}_2$  uncorrected for optical detector response is shown in Figure 3-10. The emissivity of the tungsten radiator at each wavelength for the given temperature<sup>31</sup> must also be entered into the program. The program SPECI calculates the response of the optical system as a function of wavelength after correcting the tungsten spectra for scattered light. The program also calculates a wavelength spectra of  $\text{HgBr}_2$  corrected for the response of the optical detector system; the corrected spectra using three response functions calculated at three different tungsten radiator temperatures is shown in Figure 3-11. The normalized response of the detector system was calculated, see Figure 3-9, using a tungsten source which was operated at the following three temperatures: 2914 K, 2848 K, 2719 K. The three temperatures were calculated from measurements using the optical pyrometer and the correction tables published elsewhere.<sup>40</sup>

The large relative error at the shorter wavelengths is caused by the thermal tungsten radiator which gives orders of magnitude more signal in the infrared region compared to the uv wavelengths. The radiation that is transmitted into the monochromator at the shorter wavelengths is much smaller in magnitude than that at the longer wavelengths. The huge photon flux at long wavelengths can bounce around inside of the monochromator and ultimately be detected by the photomultiplier tube having bypassed the grating. When the monochromator is set on a uv wavelength, the pmt detects a small signal due to the uv radiation and

# NORMALIZED DETECTOR RESPONSE

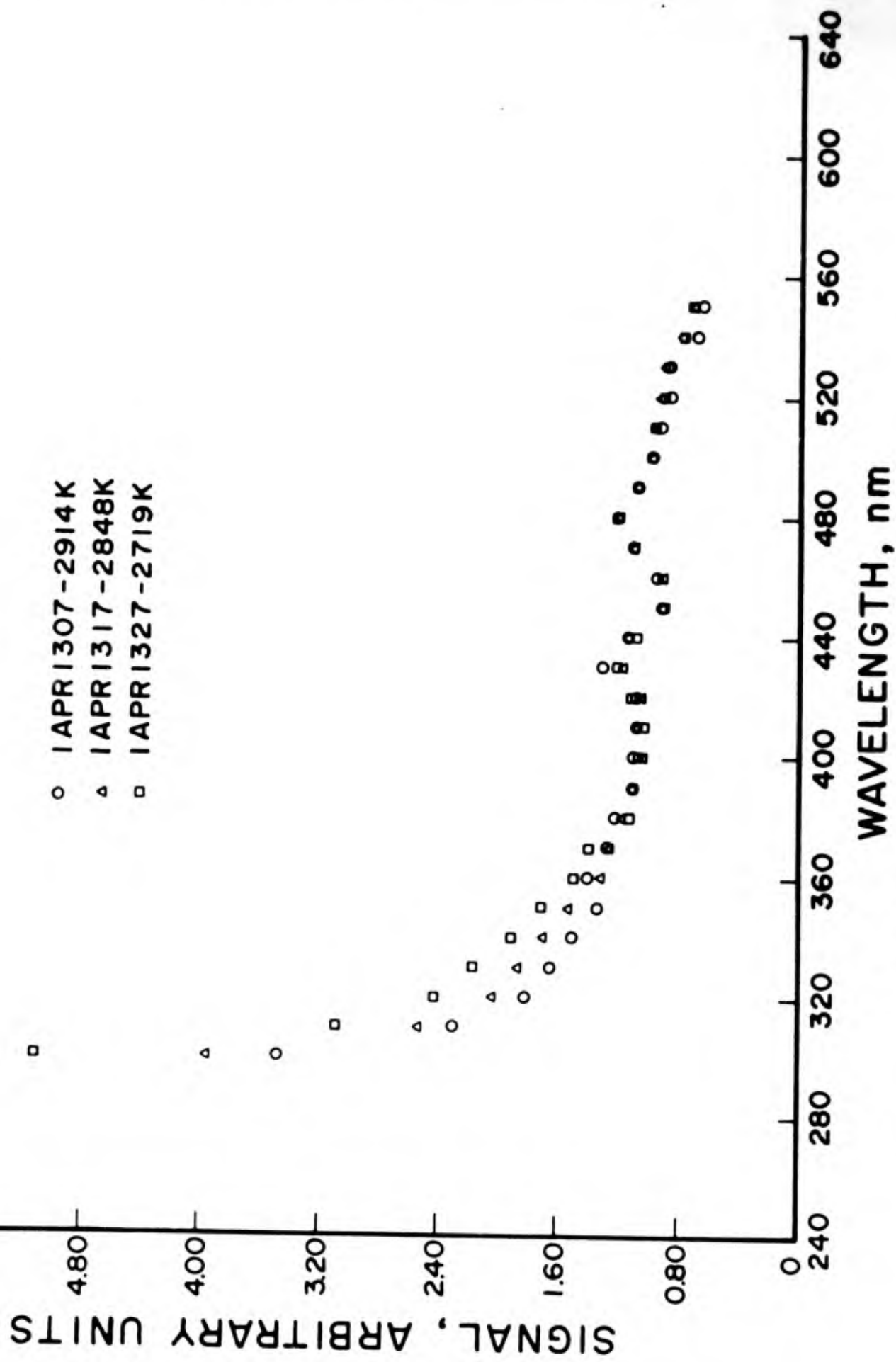


Figure 3-9 NORMALIZED DETECTOR RESPONSE

# UNCORRECTED WAVELENGTH SPECTRA

HgBr<sub>2</sub>  
ELECTRON ENERGY 100 eV  
PRESSURE 1 millitorr of HgBr<sub>2</sub>  
OPTICAL RESOLUTION 0.33 nm  
GRATING BLAZE 3000 Å

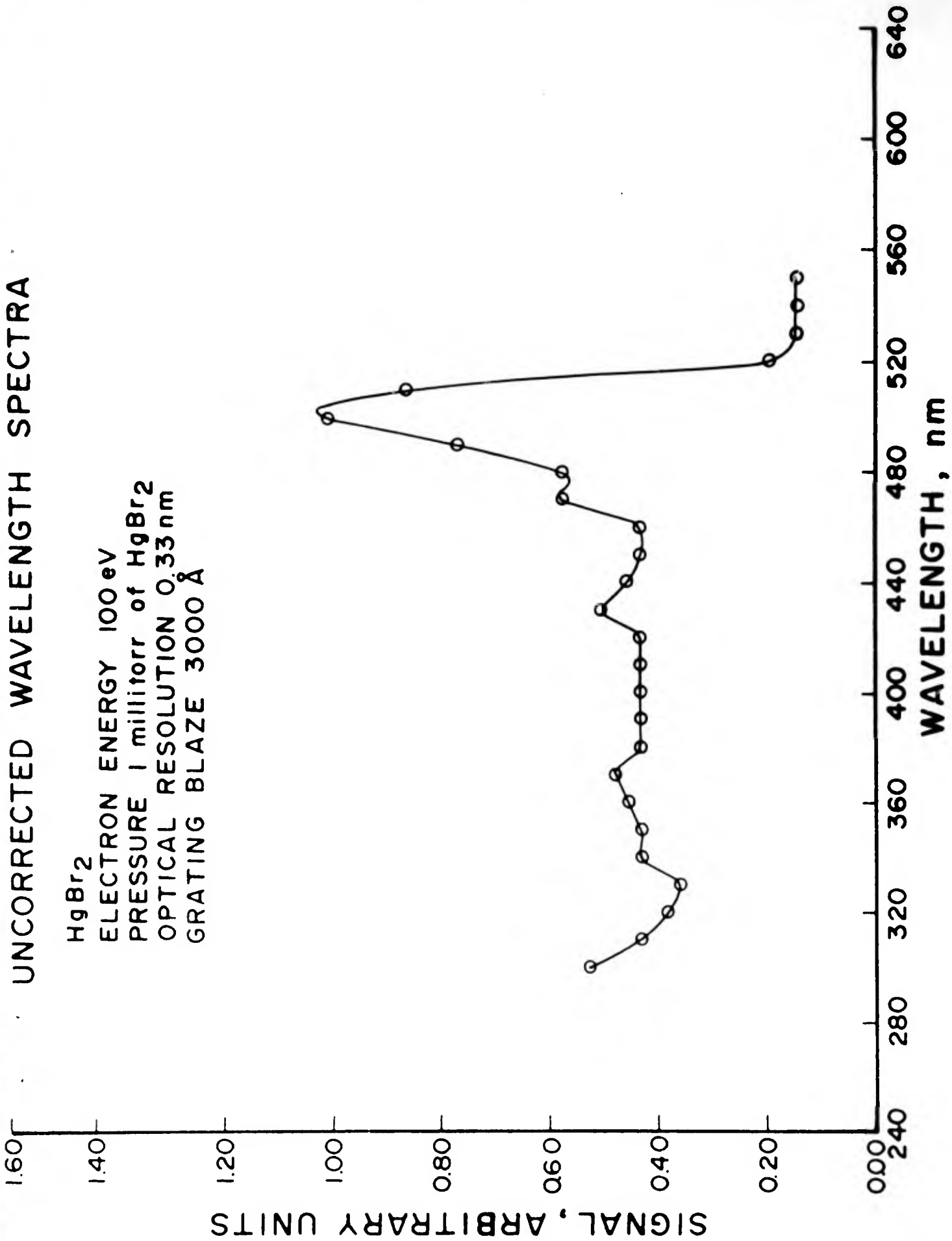


Figure 3-10 UNCORRECTED WAVELENGTH SPECTRA

# CORRECTED WAVELENGTH SPECTRA

- 1 APR 1307 - 2914 K
- △ 1 APR 1317 - 2848 K
- 1 APR 1327 - 2719 K

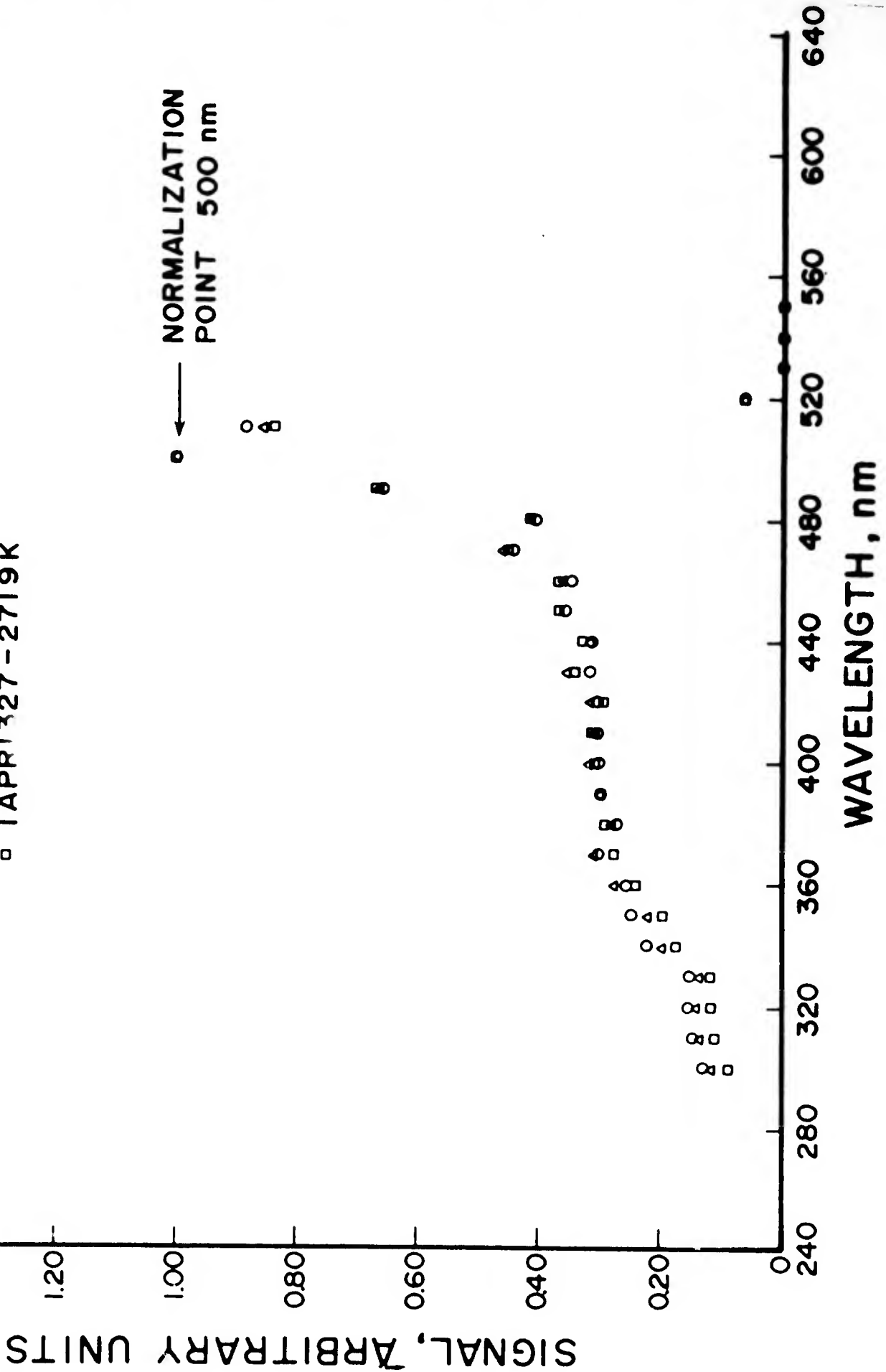


Figure 3-11 CORRECTED WAVELENGTH SPECTRA

another signal due to the scattered light from all other wavelengths. The scattered light signal detected when using a thermal radiator can approach or exceed the magnitude of the uv radiation even though the scattered light is diminished each time it is reflected from the internal surfaces of the monochromator. This is a result of the large relative magnitude of the long wavelength radiation compared to that in the uv.

The scattered light contribution at a number of wavelengths has been estimated using the method described below. This method works well from 200 to 400 nm and generally the scattered light is small at wavelengths from 400 to 500 nm. The method consists of measuring the fluorescence signal at some wavelength below the cutoff of a long wavelength pass filter such as quartz, pyrex or soda glass. In each case, the signal without the filter consists of a true signal (true in the sense of signal due to fluorescence at the selected wavelength within the monochromator bandpass) plus a signal due to the scattered light. When the filter is placed in the optical path, the only fluorescence detected will be scattered light since the long pass filter will not transmit any of the wavelengths below the cutoff. It is quite simple in this manner to get reasonably good estimates of the amount of scattered light in the wavelength interval of 200 to 400 nm since many common glasses have cutoff wavelengths in this interval. There are also techniques using sets of calibrated bandpass filters for measuring the scattered light. These and other useful schemes for scattered light measurement in optical systems are more fully described in a paper by Winter and Bloeman.<sup>42</sup>

## 5. Raw and Corrected HgBr<sub>2</sub> Spectra:

The wavelength spectra for HgBr<sub>2</sub> is shown in Figure 3-7. The spectra presented in Figure 3-7 was manually digitized at 10 nm intervals after the wavelength scale had been calibrated using the Hg line spectra which appeared in the spectra. The digitized raw spectra, normalized to be equal to one at 500 nm, was transmitted to a minicomputer and plotted by a calcomp plotter. The digitized spectra uncorrected for the response of the optical detection system is shown in Figure 3-10 and is labeled raw spectra. The raw spectra is plotted and a spline fit is drawn through each point of the data set. Each point of the raw spectra is multiplied by the normalized detector response (Figure 3-9) and the resulting curve is normalized to be equal to the one at 500nm. The resulting curve is called the corrected spectra and is shown in Figure 3-11. The three curves shown in Figure 3-11 are the results of using three normalized detector response curves measured at different temperatures of the tungsten radiator. The curve labeled 1 Apr 1317-2848 K is used for the calculation of the intergrated optical cross section presented in the next section.

## 6. Integrated HgBr<sub>2</sub> Optical Cross Section:

The corrected HgBr<sub>2</sub> spectra can be integrated but since this spectra is normalized to one at 500 nm the spectra must be calibrated at some point first. The calibration is taken from the 5048 A absolute fluorescence measurement described above. The bandwidth of the optical system has been determined to be 0.82nm full width at half maximum (fwhm). Once the corrected spectra is integrated, the ratio of the area under the corrected spectra to the area under the monochromator



bandpass is calculated. It is assumed that the shape of the bandpass function of the monochromator is rectangular and one unit in amplitude by 0.82 nm wide. The ratio of two areas is calculated by SPECI and the result is multiplied by the absolute optical cross section for production of fluorescence at 502 nm in the 0.82 nm bandpass; the product is the integrated optical excitation function for the entire emission band of HgBr<sub>2</sub>.

Integrated optical cross section for production of HgBr(B → X) fluorescence from 5500 Å to 3000 Å has been determined to be  $(3.67 \pm 1.08) \times 10^{-16} \text{ cm}^2$  at an electron energy of 20 eV. The error is believed not to exceed  $\pm 30\%$  in the integrated optical cross section determination. The major error in the measurement is due to the density determination in the scattering region. It is estimated that the error in the pressure measurement is not larger than  $\pm 15\%$  with HgBr<sub>2</sub> due to zero drift of the pressure measuring instrument and the condensable nature of the gas sample and temperature differences in the vacuum chamber. The remainder of the estimated error is due to the measurement of beam currents, fluorescence signals, drifts in the pmt and electronics and the value of the He cross section.<sup>24</sup>

The value for the integrated optical cross section at 20 eV reported in this work compares to the value of  $3.2 \times 10^{-16} \text{ cm}^2$  reported by Chantry and Chen.<sup>32</sup>

7. Production of Fluorescence below the 6 eV threshold for the production of HgBr (B → X) fluorescence

Below the 6 eV threshold for the B → X transition in HgBr, there was a very weak and diffuse fluorescence produced in the collision region

(referred to as a diffuse glow in the following but not to be confused with a glow discharge). The intensity of the diffuse glow seemed to have a broad peak at about 4 eV. The shape of the peak could be changed by adjusting the voltages on lenses of the electron gun. But in no case did the diffuse fluorescence fail to appear in the same general energy range. Figure 3-12 shows another scan of the relative excitation function of  $\text{HgBr}_2$  at 502 nm. The setup was the same as Figure 3-8 except the region from 0 to 6 eV has been expanded by a factor of 10; all other parameters of the experiment remained the same. It is seen very clearly from Figure 3-12 that the diffuse glow was present at zero energy. This was also observed by eye and these observations confirmed the electronically recorded data. The diffuse glow was roughly twice the size of the bore of the electron gun and the region of the diffuse glow had very poorly defined edges. The fluorescing region seemed to be symmetric about the axis of the electron gun. A detailed check of the electron gun in the energy range below 6 eV, clearly demonstrated that the beam was focused and not blowing apart due to space charge effects. There have been two processes identified recently that could explain the  $\text{HgBr(B)}$  fluorescence below 6 eV.<sup>35</sup> The peaks found by Azria et al in the low energy production of  $\text{Br}^-$  occur at zero eV and at 4 eV. These peaks in themselves do not explain the diffuse fluorescence that was observed in the present experiment since it has been shown by Azria et al<sup>35</sup> by considering the energy balance that neither of these peaks can produce  $\text{HgBr(B)}$  but instead produce  $\text{HgBr(X)}$ . Due to the arrangement of the experimental apparatus in the present experiment, the electron gun was immersed  $\text{HgBr}_2$  when the experiment was in operation. It has

EXCITATION OF  $\text{HgBr}_2$   
 $\text{HgBr}_2(\text{B})-\text{HgBr}(\text{X})$  FLUORESCENCE  
502 nm  
0.5 mtorr

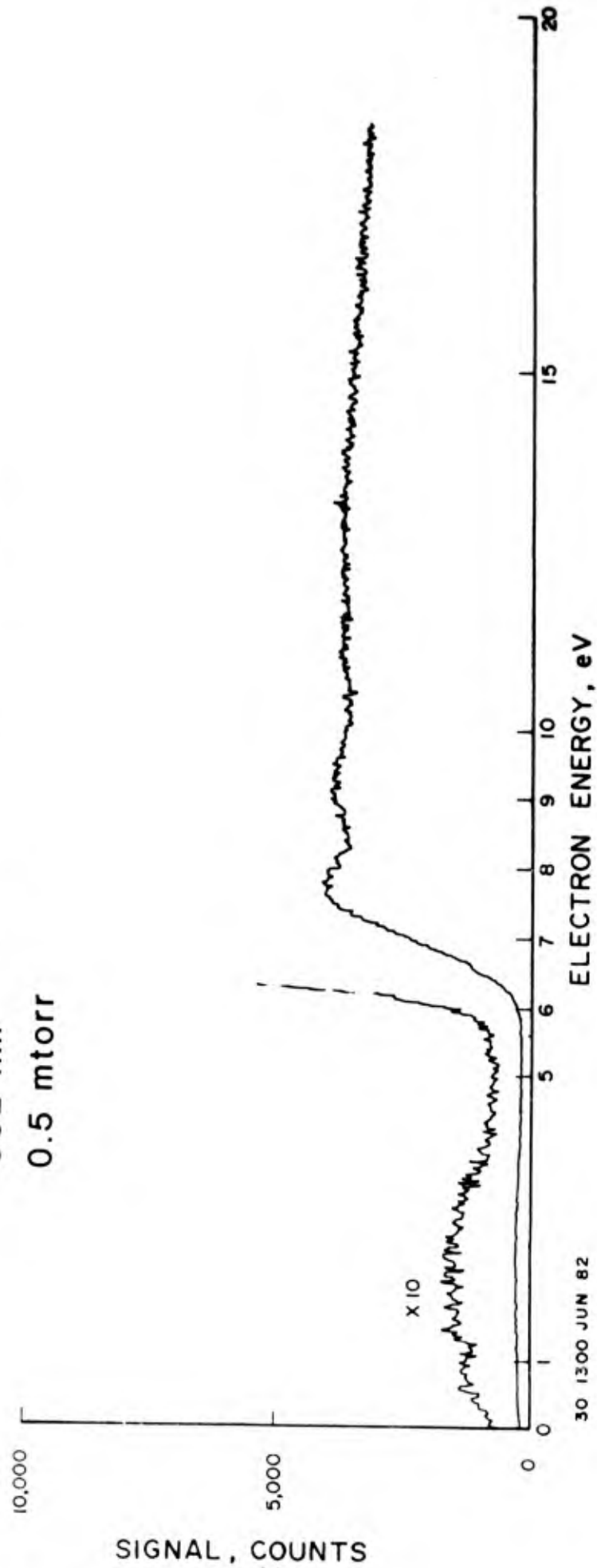
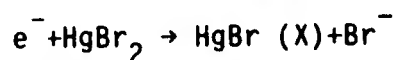


Figure 3-12 EXCITATION OF  $\text{HgBr}_2$   $\text{HgBr}_2(\text{B})-\text{HgBr}(\text{X})$  FLUORESCENCE

already been mentioned that the advantage of this type arrangement is the accuracy and ease of making an absolute pressure measurement. The disadvantage is that the gas can interact with the electron beam along its entire length especially at the cathode and along the beam line. The lenses of the electron gun had potentials applied in the range of 10 to 300 volts in order to focus the beam. During operation, it was possible to directly observe the beam line and along most of the length there was a bright blue-green fluorescence. The diffuse light in the scattering region is now thought to be caused by the resonance absorption of photons emitted from regions along the electron beam but not in the scattering region. The HgBr in the scattering region can be produced by the dissociative attachment process shown below.<sup>35</sup> The HgBr is probably produced in the electron beam and then diffuses outward; this would explain the symmetry of the diffuse glow region with respect to the axis of the electron beam. Once the HgBr molecule resonately absorbs a photon, the excited molecule reemits a photon and undergoes a transition to the ground state emitting a photon in the B-X emission band. Due to the short lifetime of the HgBr(B) state, a molecule at thermal velocities would not move far before making a spontaneous transition.

#### Dissociative Attachment



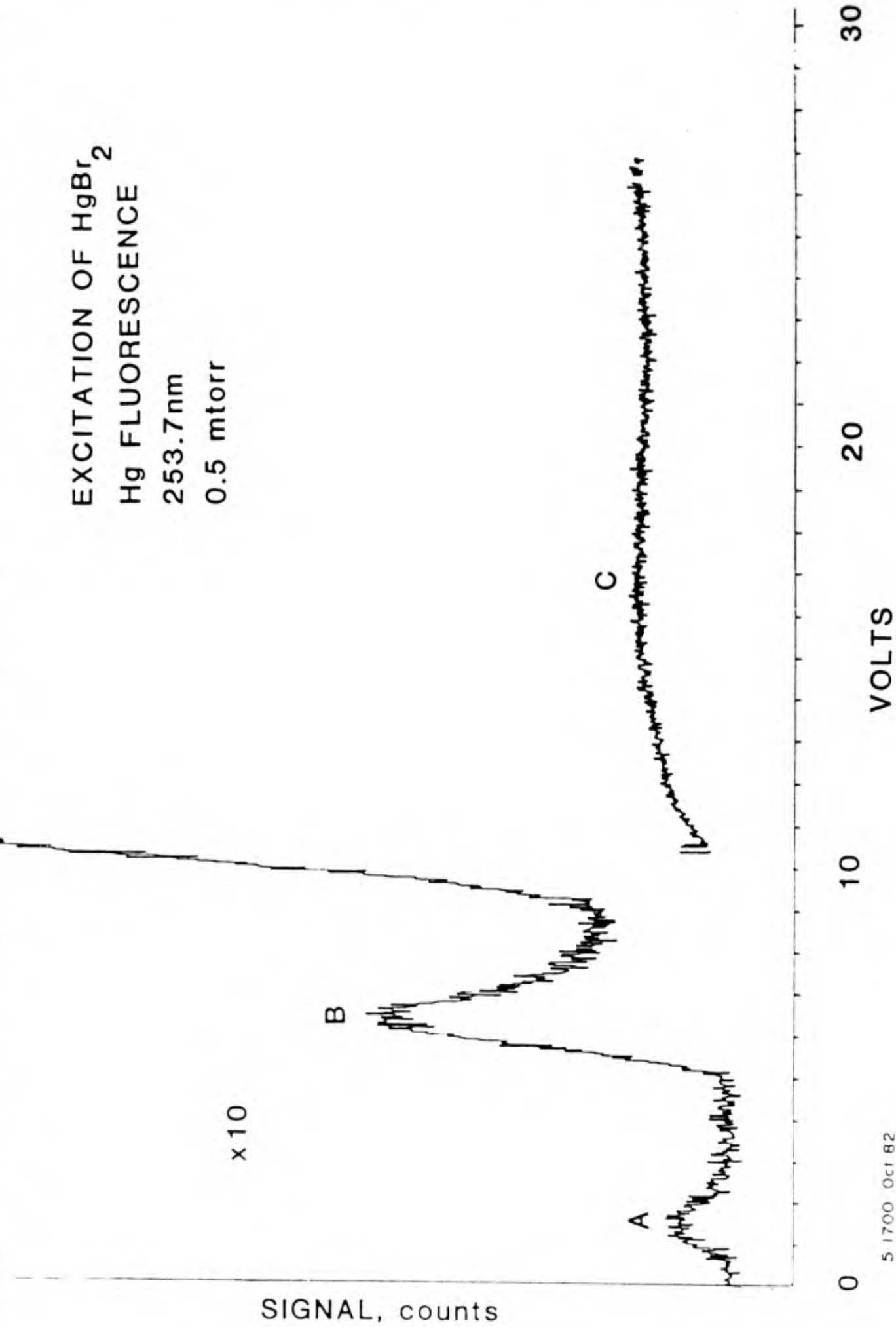
This production mechanism would explain two aspects of the fluorescence below 6 eV that were the most perplexing and difficult to explain otherwise. The two points are first the diffuse nature of the fluorescence. It is known that the lifetime of the state HgBr(B) is about

23 nsec<sup>43</sup>; this is certainly too short a lifetime to allow much diffusion of the excited B state molecules from the region of the electron beam. Second, due to the energy balance it is not possible to produce HgBr(B) by electron excitation at 4 eV.<sup>35</sup>

8. Production of  $\text{HG}^*$  in the dissociative excitation of  $\text{HgBr}_2$ :

The wavelength spectra of  $\text{HgBr}_2$  is shown in Figure 3-7. In addition to the three prominent bands labeled B $\rightarrow$  X, C $\rightarrow$  X and D $\rightarrow$  X, there are several lines due to mercury in the spectra. The source of this Hg spectra was of considerable interest since free Hg can affect everything from vacuum system components to the chemistry of the  $\text{HgBr}_2$  in the gas phase. An optical excitation function of one of the most intense Hg lines was recorded and is shown in Figure 3-13. The horizontal axis is not a calibrated energy scale but is the accelerating potential which is probably 1 to 2 volts higher than the actual energy. This optical excitation function shows a shape that is certainly not characteristic of Hg but is very similar to those of  $\text{HgBr}_2$  at 502 nm. Below 8 volts accelerating potential, the peak labeled B shows some similarity to those due to atomic Hg taken by Kenty.<sup>41</sup> The 2537 Å optical excitation function shows a feature labeled A with a threshold at approximately 1 volt and a peak at about 2 volts. A much larger feature is labeled C which has an 8 volt threshold and rises to a broad plateau above 10 volts. The ratio of peak B to peak C could be decreased by increasing the flow rate of  $\text{HgBr}_2$  through the chamber. The peak B is probably due to free Hg that has collected on the inside vacuum container walls and peak C to dissociative excitation of  $\text{HgBr}_2$ . At least some of

EXCITATION OF  $\text{HgBr}_2$   
Hg FLUORESCENCE  
253.7nm  
0.5 mtorr



5 1700 Oct 82

Figure 3-13 EXCITATION OF  $\text{HgBr}_2$  Hg FLUORESCENCE

the Hg spectra below 8 volts is due to free Hg that has collected in the vacuum system but there is another substantial fraction above 8 volts that is produced by the dissociation of  $\text{HgBr}_2$ . The similarity of the shape of the 2537 Å optical excitation function and the 5020 Å optical excitation function implies that much of the Hg spectra originates from the dissociation of  $\text{HgBr}_2$ . The small peak at 2 volts which is labeled A is probably due to the resonant absorption of photons emitted from regions of the beam line outside the scattering region as discussed above. The small peak A also implies that there is a mechanism near zero eV that produces free Hg.

## REFERENCES

1. E.J. Schimitschek and J.E. Cleto, *Optics Letters* 2, 64 (1977); E.J. Schimitschek, J.E. Celto & J.A. Trias, *Appl. Phys. Lett.* 31, 608 (1977).
2. W.L. Nighan, Technical Report, 1 Nov 1980 for Office of Naval Research Contract #N00014-76-0847; W.L. Nighan, *Appl. Phys. Lett.* 36, 173 (1980).
3. V.K. Vieland, *Zeitschrift fur Electrochem* 64, 760, (1960); *J. Chem. Phys.* 67, 4976 (1977).
4. J. Maya, *J. Quantum Electronics* QE-15, 579 (1979).
5. R.A. Olson & D.F. Grosjean, SRL, Dayton, Ohio, Private Communication.
6. M.W. McGeoch, J.C. Hsiz, D.E. Klimek to be published in *J. Chem. Phys.*
7. J. Degani, M. Rokini, S. Yatsiv, *J. Chem. Phys.* 75, 164 (1981).
8. R.S.F. Chang, R. Burnham, *Appl. Phys. Lett.* 36, 397 (1980).
9. W.L. Nigan, *Appl. Phys. Lett.* 36, 173 (1980).
10. G. Herzberg, *The Spectra of Diatomic Molecules*, Van Nostrand Reinhold, New York (1950).
11. R.W.B. Pearse, *The Identification of Molecular Spectra*, Wiley, New York (1976).
12. J. Allison, R.N. Zare, *Chemical Physica* 35, 263 (1978).
13. J.F. Waymouth, *Electric Discharge Lamps*, Cambridge, MA, MIT Press (1971).
14. B.E. Wilcomb, R. Burnham, N. Djeu, *Chem. Phys. Lett.* 75, 239 (1980).



15. R.A. Olson, D.F. Grosjean, Technical Report, AFWAL-TR-80-2026, Wright-Patterson AFB, Ohio.
16. W.R. Wadt, J. Chem. Phys. 72, 2469 (1980).
17. R. Burnham, E.J. Schimitschek, Laser Focus 54, (June 1981).
18. J. Degani, M. Rokni, S. Yatsiv, J. Chem. Phys. 75, 164 (1981).
19. W.R. Wadt, Appl. Phys. Lett. 34, 658 (1979).
20. J. Maya, J. Chem. Phys. 67, 4976 (1977).
21. Anderson Labs, Urbana, IL
22. H.S.W. Massey, E.H.S. Burhop, Electronic and Ionic Impact Phenomena, Vol. 1, Clarendon Press, Oxford (1969).
23. J. Husain, J.R. Wisenfeld, R.N. Zare, J. Chem. Phys. 72, 2479 (1980).
24. B. Van Zyl, G.H. Dunn, G. Chamberlain, D.W.O. Heddle, Phys. Rev. A 22, 1916 (1980).
25. F.A. Sharpton, Excitation of Neon Atoms by Electron Impact, a Dissertation, University of Oklahoma, Norman, Oklahoma (1968); K.G. Walker, Simultaneous Ionization and Excitation of Neon by Electron Collision, a Dissertation, University of Oklahoma, Norman, Oklahoma (1971).
26. Ceramaseal Company, New Lebanon, New York, Private Communication.
27. Englehard Corp., Iselin, New Jersey, Private Communication.
28. Products for Research, PMT Cooler model TE-104, Danvers, Mass.
29. J. Tellinghuisen & J.G. Ashmore, Appl. Phys. Lett. 40, 867 (1982).
30. J.H. Parks, Appl. Phys. Lett. 31, 297 (1977).
31. J. C. DeVos, Physica 20, 690 (1954).

32. P.J. Chantry, C.L. Chen, Final Report #82 9C1-EXC11-RI, May 15, 1981 to June 30, 1982, Westinghouse R&D Center, 1310 Beulah Rd. Pittsburgh, PA 15235.
33. D. Spence & M.A. Dillon, ANL-80-115, Part 1, Oct 1979 - Sept. 1980, Argonne National Lab, Argonne, IL.
34. S. Dushman, Scientific Foundations of Vacuum Technique, second edition, Wiley (1962); Leybold Heraeus Product and Vacuum Technology Reference Book; D.J. Santeler, D.W. Jones, D.H. Holkeboer, F. Pagano, Vacuum Technology and Space Simulation, Aero Vac Corp., NASA SP-105; NTIS, N66-36129.
35. R. Azria, J.P. Ziesel, R. Abouaf, L. Bouby, M. Tronc, J. Phys. B. 16, 17 (1983).
36. H.W.S. Massey and E.H.S. Burhop, Electronic and Ionic Impact Phenomena, Oxford University Press (1969).
37. L. J. Kieffer, NBS miscellaneous publication 289, (1967).
38. J. D. Jobe Excitation Processes in Helium, a dissertation, University of Oklahoma, Norman, OK (1968).
39. A. Garscadden private communication AFWAL/POOC Wright-Patterson Air Force Base, OH 45433.
40. AIP Handbook of Physics, section 6K; CRC Handbook of Physics and Chemistry 49th Edition, page E-228.
41. C. Kenty J. Appl. Phys. 21, 1309 (1950).
42. H. Winter, E.W.P. Bloemen J. Phys. E. 15, 1007 (1982).
43. M.N.R. Hutchinson, E.S. Theocharous Chem. Phys. Lett. 81, 553 (1981).
44. F. Rosebury Electron Tube and Vacuum Technology, Addison-Wesley (1965).

## APPENDIX A

### STANDARD OPERATING PROCEDURE

For Identification of Valves, Refer to Figures 2-1 & 2-2

#### EVACUATION OF CHAMBER (if necessary)

- A1) Close V1 Open V3 to use DK20 as holding pump on diffusion pump.
- A2) Open V8 to rough out the chamber.
- A3) When chamber has reached a pressure of  $10^{-2}$  Torr as indicated on TC2, close V8 and V3.
- A4) Open V1 and V2; then the diffusion pump is acting on the system with the DK50 acting as the forepump.

#### EVACUATION OF GAS MANIFOLD (if necessary)

- B1) With V15 and V19 closed open V4, V16, and V18 to establish a reference pressure for the baratrons. When TC5 indicates a sufficiently low pressure, close V16.
- B2) Open V15 and V17 to rough out the manifold using the DK20. If required, open V11, V12, and V13 to pump out the lines to the gas bottles. When the baratrons indicate a sufficiently low pressure, close V15 and V4.
- B3) Open V14 and V10 to pump on the manifold with the ultra high vacuum capabilities of the main pumping system.
- B4) If necessary open V19 and V18 to check on baratron zero settings.
- B5) Close all valves V10 - V20.

### FILLING OF GAS MANIFOLD

- C1) If necessary, evacuate the gas manifold using the steps outlined above.
- C2) Ensure that V10 and V14 are closed.
- C3) If the above procedure is not necessary, check the baratron's zero setting by opening V15, V16, V18, and V 19. Establish an absolute reference, as measured on TC5, by opening V4. When sufficiently low pressure has been reached, close V4, V15, V16, and V19.
- C4) Open V17. Then the baratrons read the pressure in the manifold.
- C5) Fill the manifold from the gas bottles by opening V11, V12, or V13 and the appropriate needle valve. For greatest accuracy, start with the gas for which the smallest fraction is required in the gas mix.

### FILLING OF VACUUM CHAMBER FROM THE GAS MANIFOLD

- D1) If necessary to check baratron's zero settings and reference, follow the procedures in C3 (above).
- D2) Open V10. The Baratrons measure pressure in the chamber.
- D3) Open V17 until the pressure in the chamber reaches the desired value. Close V17.

### PROCEDURE FOR CONNECTING SAMPLE BOTTLE

- E1) If possible, attach sample bottles to system before experiment is commenced. Then open valve at neck of sample bottle during "Evacuation of Gas Manifold" procedure described above. After evacuation, close the sample bottles

valves. The advantage in connecting the sample bottle at this time is that they are then evacuated by the ultra-high vacuum capability of the main chamber. If it is decided to take samples after an experiment has commenced, follow the steps E2 to E6.

- E2) Close valves V10, V15, V17, V19.
- E3) Attach the sample bottles to the appropriate VCR fitting.
- E4) Open V15 to evacuate the tubes now filled with air.
- E5) If required to check the baratrons' zero settings and reference, follow the procedure in C3 (above).
- E6) Open the S.B. valves with V15 open to evacuate the S.B.'s. Close the S.B. valves.

#### PROCEDURE FOR TAKING A SAMPLE FROM EITHER MANIFOLD OR CHAMBER

- F1) Close the S.B. valves and V15.
- F2) Open either V10 or V17, depending on from where it is desired to take a sample.
- F3) Open V15 and V4 and pump away some gas.
- F4) When one is sure that the gas in the lines near the sample bottle is from the bulk of the chamber and not from the large diameter tubing connected to the chamber, open the S.B. valve and close V15.
- F5) Close V10, V17, and the S.B. valve. Record the baratron reading.
- F6) Open V15 to evacuate the tubing.
- F7) Close V15 and V4.

- F8) If it is desired to disconnect the sample bottle from the system at this time, follow steps (E2) to (E6). Attach either another sample bottle or a blind VCR cap to the sample port.

#### OPERATION OF HIGH VOLTAGE DISCHARGES

- G1) Ensure no extraneous personnel are present.
- G2) Turn on trigger unit and oscilloscopes.
- G3) Turn on pressurized air for the spark gaps, with a slow air bleed rate. Set the air pressure at a high valve.
- G4) Turn on high voltage supply. Turn up the high voltage to its desired value.
- G5) Turn down the pressure of compressed air until the spark gap self triggers. Then turn up the air pressure slightly.
- G6) Proceed with experiments, using trigger unit to fire the spark gap.

#### SHUTDOWN PROCEDURES

- H1) Turn down the high voltage power supply, continuing to fire the trigger unit at regular intervals.
- H2) Turn off the compressed air regulators, allowing the spark gap pressure to fall to zero.
- H3) Turn off the power supply, the trigger unit, and oscilloscopes.
- H4) If it is necessary to approach the high voltage components, use a grounding rod to discharge both sides of all capacitors.
- H5) Evacuate the chamber as in steps (A1) to (A3) or (A4).

**EMERGENCY SHUTDOWN**

- I1) Turn off the high voltage power supply and the trigger unit.
- I2) Use a grounding rod to short out both sides of all capacitors.
- I3) Turn off the compressed air regulator.

## APPENDIX B

### TEMPERATURE AND METASTABLE DENSITY DIAGNOSTICS

#### MEASUREMENT OF TEMPERATURE IN ARGON NITROGEN DISCHARGES

Reference: Copley & Camm JQSRT 14. 899 (1974).

1. Rotational temperature found from measurements of intensities in C-B transitions of  $N_2$  at 3805 A.
2. Rotational temperatures obtained from "well-known formula" for distribution of intensities in a rotational band, after summing over triplet contributions.
3. Accuracy 10% @ 1000 K.
4. Experiment utilized a spectrometer with resolution of 0.1 A°.

#### DYE LASER DIAGNOSTICS OF METASTABLES

To measure the density of metastables produced in pulsed discharges in the TESLA chamber, it is proposed to use an NRG tunable dye laser. The characteristics of the laser system are summarized in the table, along with characteristics of the available detecting systems.

<u>Laser</u>	$N_2$ laser pumped dye laser
	$N_2$ laser
	Dye laser
	Beamwidth
	Divergence
	Spectral Width
	900 kw for 5 ns FWHM
	5% efficient - 45kw
	~ 2mm
	3 mrad
	~ 0.04 nm

#### AVAILABLE SPECTROMETERS

- (1) Jarrell Ash 1/4 m: 0.2 nm spectral width. Response with RCA 8540 photomultiplier  $2 \times 10^4$  amps/watt approximately.
- (2) 1/2 m spectrometer: 0.03 nm spectral width.



## LASER-ATOM INTERACTIONS

The interaction between a radiation source and a two level atom when both the radiation source and the atomic response function have arbitrary line width has been considered by Greenstein and Gates [JOSA 65, 33 (1975)]. This paper has some shortcomings, as discussed later, but nevertheless it is a good starting point because it explicitly considers the irradiation line shape. They consider the steady state solution to the master equation for a two level system with excitation by a radiation field and relaxation from the upper to the lower level until an equilibrium distribution is reached. They derive an absorption coefficient given by

$$k = k_0 L [1 + LI/I_S]^{-1} = - \frac{1}{I} \frac{dI}{dz}$$

where the small signal ( $I \ll I_S$ ) absorption is given by [mks units]

$$k_0 = \frac{N\omega\mu^2 T_2}{\tau c \epsilon_0} (-\rho_0)$$

and the saturation intensity is given by

$$I_S = \frac{c\tau^2\epsilon_0}{2\mu^2 T_1 T_2}$$

The dimensionless function  $L$  ( $0 < L < 1$ ) represents the overlap between the frequency response of the atomic system and the frequency distribution  $I(\omega)$  of the exciting radiation

$$L(\omega_r, \omega_0) = L_a(\omega, \omega_0) I(\omega) d\omega [ \int I(\omega) d\omega ]^{-1}$$

where

$$L_a(\omega, \omega_0) = [1 + (\omega - \omega_0)^2 T_2^2]^{-1}$$

is the Lorentzian absorption line shape. Other terms are defined as follows

- $\omega$  = frequency in  $\text{sec}^{-1}$  [hertz/2 ]  
 $\omega_0$  = absorption frequency  
 $T_2$  = coherence relaxation time  
 $T_1$  = energy relaxation time of upper state  
 $\mu$  = transition matrix element  
 $N$  = number density  
 $\rho_0$  = population difference in the absence of radiative transitions  
 $= [1 - e^{-\omega_0/kT}] [1 + e^{\omega_0/kT}]^{-1} \approx -1$

Greenstein and Bates treat an oversimplified view of a typical atomic system and it is of more interest to treat a multilevel system such as that shown in the figure. The equations describing the evolution of the matrix elements in this case are considered by Murray Sargent III, M. O. Scully, and W. E. Lamb Jr. in Laser Physics (Addison Wesley 1974) pg. 103. Note the equations in S., S., and L. differ from those in G. & B. because of the difference between the Schroedinger and Interaction interpretations of quantum mechanics. The formulae derived in G. and B. are still valid provided the following substitutions are made

$$\rho_0 = \frac{\lambda_a(\gamma_b - \gamma_1) - \gamma_b(\gamma_1 + \gamma_a)}{\gamma_b(\gamma_a + \gamma_1)}$$

and

$$I_S = \frac{c\tau^2\epsilon_0 (1 + \lambda_1/\lambda_a)}{\mu^2 T_2 (1/\gamma_a + 1/\gamma_b)}$$

Here  $\lambda_a$  and  $\lambda_b$  are the pumping rates of the upper and lower levels respectively, and the relaxation rates are best defined by referring to the diagram. The pumping rates include cascade transitions from higher excited levels except that from the upper to the lower level, which is explicitly taken into account.

There are still three problems with this treatment. One problem is that it neglects possible degeneracies of the atomic levels. There is some indication that the saturation parameter is given by

$$I_s = \frac{2\tau^2 c \epsilon_0}{T_2 \mu^2} \frac{1 + \gamma_1/\gamma_a}{1/\gamma_a + g_a/g_b \gamma_b}$$

in the case that the upper and lower levels have degeneracies  $g_a$  and  $g_b$  respectively. I have not verified this formula and doubt its accuracy since it differs from the previous one by a factor of two in the case  $g_a = g_b$ . However, it serves to point out that the level degeneracies will not enter into the problem in an obvious manner.

The small signal absorption coefficient is modified for transitions between degenerate levels.

$$K_0 = \frac{(-\rho_0 N) g_a}{g_b} \frac{\omega \mu^2 T_2}{\tau c \epsilon_0}$$

This can be verified by comparing with the formulae 3.90 and 3.83 of Garbuny, Optical Physics (Academic, 1965).

Note in addition that Greenstein and Bates neglect to perform a spatial average of the direction of the dipole moment with respect to the direction of observation. This introduces a factor of three:

$$\mu^2 = \frac{e^2}{3} (\chi_{ab})^2$$

See Merzbacher, Quantum Mechanics, pg. 454. Garbuny uses classical arguments (pg 74) to produce this factor of three.

The third shortcoming of the above theory is that the absorption coefficient and its frequency dependence was derived in the steady state approximation. The explicit time dependent solution for the elements of the density matrix is difficult for any particular shape of the laser pulse. However, in the limit that the exciting radiation pulse and the population differences do not change appreciably in a time  $T_2$ , the equation for the off diagonal density matrix elements can be solved and eliminated, resulting in coupled equations for the population of the atomic levels (pg. 104 of S. S. & L., modified).

$$\dot{\rho}_{aa} = \lambda_a(t) - (\gamma_a + \gamma_1)\rho_{aa} + R(\rho_{bb} - \rho_{aa})$$

$$\dot{\rho}_{bb} = \lambda_b(t) - (\gamma_b + \gamma_1)\rho_{bb} + R(\rho_{aa} - \rho_{bb})$$

The simplification to these rate equations is justified in the present experimental situation in which the laser pulse length is 5 ns and the mean free time between phase disturbing collisions varies from 0.14 ns at 100 Torr to 10 ps at 1400 Torr in Argon. Certainly this approximation is valid at the higher pressures in the range considered. The steady state solution for the above equations leads to the same solutions for level densities and the saturation intensity as considered previously. In performing the experiments at higher pressures, the steady state solutions to the rate equations can be used since relaxation times are small compared with pulse length. The experiment can be performed for  $I < I_s/L$  or  $I > I_s/L$ . The latter case corresponds to driving the transition with the laser pulse much faster than the relaxation time so that every molecule which can absorb does. This is discussed in more detail in a following section. In both cases mentioned above the

solution to the absorption equation

$$k = - \frac{1}{I} \frac{dI}{dz} = \frac{k_0 L}{1 + LI/I_s}$$

is

$$\ln \frac{I_{in}}{I_{out}} + \frac{L}{I_s} (I_{in} - I_{out}) = k_0 L \Delta z$$

For the unsaturated case, only the first term on the left hand side of the above equation is significant.  $k_0$  can be found directly from the absorbed intensity ratios, provided the spectral distribution of the laser radiation and the absorption bandwidth  $T_2$  are known. Since ratios of intensities are used, calibration of the detection system is not required. For the case of saturated absorption, only the second term on the left hand side of the above equation is significant. The saturation intensity  $I_s$  must be known, but the solution for the small signal absorption  $k_0$  does not require knowledge of the spectral distribution of radiation since the factor  $I$  cancels out. Extracting information about the metastable density that existed prior to the laser pulse  $-\rho_0 N$ , from the small signal absorption coefficient  $k_0$  requires knowledge of the phase relaxation time  $T_2$  and dipole moment matrix element  $\mu$ . A survey of the available information for the Argon atom is given in a following section.

#### PREVIOUS EXPERIMENTS PROBING ARGON METASTABLES

Chang and Setser [JCP 69, 3885 (1978)] describe an experiment in which a 5 ns FWHM dye laser pulse was used to measure lifetimes of levels that are optically connected to the argon metastable states. This paper gives a good description of the relevant spectroscopy. In particular,

this paper gives a list of the dyes and solvents needed to access different spectral lines terminating on the metastable level. In the paper, the lifetimes of each of the levels optically connected to the metastable states and the branching ratios for transitions out of the excited state are measured.

Because the work presented in the above referenced paper is concerned only in decay rates of levels and not in the absolute determination of individual level populations, it was of little concern to the experimenters whether their laser was sufficiently intense to saturate the optical transition or not. This is a stark contrast to the anticipated experiment measuring population densities. In an earlier paper (Faraday Discussions Chem. Soc. 1972 No. 53 pg. 100), Setser and coworkers had measured the quenching processes and rate constants for interaction of metastable argon atoms with diatomic and triatomic molecules. For this work an Oriel Optics Spectral Calibration Argon pen lamp was used as a source for steady state absorption measurements on transitions originating on the Argon metastables.

Argon and other atomic metastables have been probed by reabsorption [Kato et al., JOSA 69, 175 (1979)], self absorption [Jolly and Touzeau, JQSRT 15, 863 (1975)], and intracavity absorption (references in Brink and Meider, Optics Letters 6 366 (1981)). In none of these cases can an accurate absolute value of number density be found as easily as in an absorption experiment. Zamir et al. [IEEE J. Quant. Elect. 15, 281 (1979)] have observed visible absorption from electron beam excited Krypton. The decay of the absorption was very rapid (10-20 ns) at eight atmospheres pressure. They point out the absorption should be useful as a monitor of the metastable density.

Copley and Lee [Can. J. Phys. 53, 1705 (1975)] measure populations and the electron excitation coefficients of the  $^3P_2$ ,  $^3P_1$ ,  $^3P_0$ , and  $^1P_1$  levels of argon by monitoring the absorption out of these levels to higher argon levels. Two of these levels are metastable, and two have allowed transitions to the ground state.

#### SATURATION OF LASER INDUCED FLUORESCENCE

It has been proposed that measuring of species concentrations is simplified when the laser is sufficiently strong to saturate the optical transition [I. W. Daily, Applied Optics 17, 225 (1978); 16, 568 (1977); 15, 955 (1976)]. Under these conditions the laser induced fluorescence signal is no longer dependent on quenching rates which may not be known accurately or on laser power. The effects of using a pulsed laser for saturation measurements is considered by Calcar et al [JQSRT 21, 11 (1979)]. They show misleading results are obtained by taking time integrated as distinct from time resolved measurements. Moreover, the spatial distribution of the laser radiation in the region of observation must be uniform.

Some complications in the procedure using the saturation of laser induced fluorescence have been observed. It was found that the laser excited species might react with neutral species [Calcar et al. JQSRT 21, 11 (1979)], or the population of short lifetime excited atoms is equivalent to low ionization potential impurities or can transfer their energy to electrons in super elastic collisions [Measures, J. Appl, Phys. 48, 2673 (1977)]. In one case, the power difference between that predicted and that experimentally observed to saturate the laser induced fluorescence was explained by super radiant emission from the laser

excited species [Sharp and Goldwasser, Spect. Data B, 31, 431 (1976)]. This was verified by examining the polarization of the fluorescence. It could, however, be avoided by ensuring the coherence relaxation time  $T_2$  is much shorter than the laser pulse length. The other complications mentioned above must be taken into account, if they occur at all, whether one makes measurements in the linear portion or the saturated region in the dependence of laser induced fluorescence on laser intensity. In measuring laser induced fluorescence, branching ratios for what happens to the laser excited atoms must be known.

SAMPLE CALCULATION OF PARAMETER

This is determined by the spectral distribution of the radiation source.

$$\text{Case 1 Suppose } I_{\omega} = I_0 / \Delta\omega_L \text{ if } |\omega - \omega_0| < \frac{\Delta\omega_L}{2}$$

$$= 0 \text{ otherwise}$$

$$\text{Then } L = \frac{2}{\Delta\omega_L T_2} \tan^{-1} \frac{\Delta\omega_L T_2}{2}$$

$$\rightarrow 1 \text{ for } \frac{1}{2} \Delta\omega_L T_2 \ll 1$$

$$\rightarrow 1 / \Delta\omega_L T_2 \text{ for } \frac{1}{2} \Delta\omega_L T_2 \gg 1$$

Case 2 Suppose  $I_{\omega}$  is Lorentzian with HWHM given by  $T_0$   
 i.e.  $I_{\omega} = I_{\omega r} [1 + (\omega - \omega_r)^2 T_0^2]^{-1}$ ,  $2T_0 = 1 / \Delta\omega_L$

$$\text{Then if } \omega_r = \omega_0, L = (1 + \frac{T_2}{T_0})^{-1}$$



The actual spectral distribution will have to be measured for measurements in the 100 Torr range since  $T_2 \sim 0.1$  ns and the dye laser manufacturer quote the spectral width of the dye laser as 0.04 nm.

Then  $\Delta\omega_L T_2 \sim 0.8$  | 100 Torr

But  $L = 1$  is a good approximation at 1400 Torr.

PRESSURE BROADENING OF ARGON SPECTRAL LINES

- (1) Copley and Camm JQSRT 14, 899 (1974)
- (2) Vallee et al. JQSRT 18, 327 (1977)
- (3) Copley JQSRT 16, 553 (1976)
- (4) Hindmarsh & Thomas Proc. Phys. Soc. A77, 1193 (1961)

Some additional references in (1) above. N. B. widths  $\Delta\omega/N$  should scale as  $T^{0-3}$  for van der Waal's forces. See discussion of measurements

pg. 905 of Copley and Camm above.

nm	Width in $\text{cm}^{-1} \text{ cm}^{-3} \times 10^{-20}$				$\text{cm}^{-1}$
	$\delta/N$	$\delta/N$	$\delta/N$	$\delta$ 100 T.	
707	$2.9 \pm 0.3$	2.7	2.05	0.066	0.16
738	$4.02 \pm 0.23$		2.9	0.093	0.11
841	$16.2 \pm 1.0$		12	0.39	0.027
Temp(k)	1130	1130	400	400	
Ref	(1)	(2)	calc.	calc.	calc.

$\Gamma = \Delta\omega$  where  $\Delta\omega =$  spectral HWHM in radians/sec.

$\bar{T}_2$

In applying this result to an Ar:N<sub>2</sub> mixture, one assumes that phase perturbation by an N<sub>2</sub> molecule colliding with an excited argon atom is the same as that by a ground state argon atom. This is most probably not true, although may be the same order of magnitude.

Note, however, that these transitions terminate on metastable state, and

the relaxation of the metastable state by collisions with  $N_2$  is 100 times more probable than that with Argon. This difference might also be reflected in the optical broadening cross section. Note the values of  $T_2$  are about one tenth the mean free time between gas kinetic collisions.

### COLLISIONAL QUENCHING OF ARGON METASTABLES

(1) Fishburne, J. C. P. Vol 47 Pg 58 (1967).

Measures the collision cross section for nitrogen-argon metastable energy transfer to be 100 times that for argon-argon de-excitation collisions. Absolute values were not measured.

(2) Piper et al. (inc. Setser) Faraday Discussions of Chem. Soc. 1972 No. 53 pg. 100 (1971).

Rate constant for deactivation of Argon  $^3P_2$  metastables.

$$k(N_2) = (3.3 \pm 0.3) \times 10^{-11} \text{ cm}^3 \text{ s}^{-1}$$

$$k(\text{Ar}) = 3' \times 10^{15} \text{ cm}^3 \text{ s}^{-1}$$

Hence in a 10%  $N_2$  90% Ar mixture at 100 Torr the lifetime of the  $^3P_2$  metastables is 94 ns and is 7 ns at 1400 Torr.

### LIFETIME OF EXCITED ARGON STATES

Measured by Chang and Setser JCP 69 3885 (1978).

For  $^2P_3$  level at 107290  $\text{cm}^{-1}$

Radiative lifetime 27.6 ( $\pm$  0.9) ns

Collisional deactivation by Argon

- to lower states in  $^2P_3$  manifold  $k=6.3 \times 10^{-11} \text{ cm}^3 \text{ s}^{-1}$

- to 1s manifold  $k=4.7 \times 10^{-11} \text{ cm}^3 \text{ s}^{-1}$

Total  $k=1.1 \times 10^{-10} \text{ cm}^3 \text{ s}^{-1}$

at 100 Torr collisional lifetime

2.8 ns

at 1400 Torr collisional lifetime

0.2 ns

Note these are only twice the M.F.T. between gas kinetic collisions.

### EXPERIMENT

Measure absorption or laser induced fluorescence on the 707 nm line from the  $1s_5$  metastable state to the  $2p_3$  state.

Reasons for choice of this line.

- (1) All the relevant parameters are known, including deactivation rates and branching ratios for downward transitions.
- (2) Both the upper state and the lower state of the transition are five fold degenerate. Therefore, the ratios of the degeneracies cancel out and the formulae presented in the previous section are applicable.
- (3) This is the highest state in the  $2p$  manifold. Transitions from the metastable states to other states in the  $2p$  manifold occur in the near infrared, where detectors become less responsive.

For this 707 nm line I calculate a small signal absorption coefficient and saturation intensity of

$$k_0 = f_{ms} 10^9 \text{ m}^{-1}$$

where  $f_{ms}$  = fraction of argon atoms that are in the relevant metastable level

$$\text{and } I_s = \begin{matrix} 0.6 \text{ W/cm}^2 & \text{at 100 Torr} \\ 9 \text{ W/cm}^2 & \text{at 1400 Torr} \end{matrix}$$

Note that  $k_0$  is independent of pressure but that  $I_s$  is proportional to the square of pressure.

$$k_0 = f_{ms} N \frac{g^a}{g_b} \frac{\omega \mu^2 T_2}{\tau c \epsilon_0} \quad T_2 = 0.16 \text{ ns} \quad 100 \text{ T.}$$

$$I_s = \frac{c \tau^2 \epsilon_0}{\mu^2 T_2 (1 + 1)} \frac{\bar{\gamma}_a}{\bar{\gamma}_b} \quad \begin{matrix} \gamma_a = 1/2.8 \text{ ns} \\ \gamma_b = 1/94 \text{ ns} \end{matrix}$$

## POSSIBLE MEASUREMENT METHODS

### Absorption Experiment with Incoherent Source

Use as source an Oriel Argon calibration light, modified if necessary to give a constant output.

Assuming source is Doppler broadened at 400 k, the spectral width of the lamp output is  $0.032 \text{ cm}^{-1}$  for the 707 nm line.

Note the absorption linewidth varies from  $0.066 \text{ cm}^{-1}$  at 1400 T. Assuming the source emits  $10^{-6} \text{ w}$  at 707 nm, the order of magnitude estimates of responsivity shows the line to be barely observable. However, there is no justification for assuming that power level. To observe the metastables with nanosecond time response, it is essential that the photomultiplier have a 50 ohm termination.

For a 50 cm discharge, the absorption coefficient is  $k_0 \Delta z = f_{ms} 5 \times 10^8$ .

From  $\ln \frac{I_2}{I_1} = k_0 L \Delta z$  since we are much below saturation intensity  
 $L \sim 1$  spectral overlap function

$I_2$  = signal in absence of discharge

$I$  = signal with discharge

Minimum detectable absorption 1% - corresponds to  $f_{ms} \sim 10^{-10}$ . It is very probable that signal will be totally absorbed.

### Complications

- (1) There may be emission at this wavelength in the discharge. This emission if it exists must be measured as a function of time and subtracted off the observed signal.

(2) There may be beam steering effects due to index of refraction changes caused by sudden heating of the gas. This could be checked by replacing the argon calibration lamp by a helium source of the same dimensions. The helium emission will not react resonantly with any of the gas in the chamber, and any change of observed signal is due to discharge induced beam distortion or steering. The beam distortion will be minimized when it is symmetrically located between the electrodes and apertured to pass only through the positive column in which the power deposition is uniform. However, there will be edge effects which may not be negligible. It may be necessary to subtract off a contribution to the signal as measured using a non-resonant helium source

(3) Both  $k_0$  and  $I_s$  depend on relaxation parameters which are temperature dependent. The gas temperature will increase dramatically during the pulsed discharge, but the gas density will remain constant. The relaxation parameters will, however, be time dependent. The  $T_2$  parameter is, however, only weakly temperature dependent (Copley, JQSRT 16, 553 [1976]),

$$T_2 \propto T^{-0.3}$$

and it could safely be evaluated by taking an average temperature value. Aside Measurements of  $T_2$  and all the relaxation parameters are always made under conditions in which the excitation is very small. The broadening is caused by interactions of the excited atom undergoing the transition with ground state molecules. In this case, however, a significant fraction of the atoms will be in excited electronic states. It would be very

interesting to make a measurement of  $T_2$  under these conditions. I doubt that a value for  $T_2$  measured under low excitation conditions is valid under conditions of high excitation. Nobody else has ever worried about this, however.

#### Absorption Experiment with Laser Source

The absorption experiment could be performed using the laser as a source.

Since the laser output will be in the form of 45 kw pulses, if the output is expanded to occupy some fraction of the interelectrode space, the intensity will be of the order of  $10^4$  W/cm<sup>2</sup>. This is much greater than the saturation intensity of the medium at all pressures.

A spectrometer must be used with the dye laser to measure the wavelength of the output and ensure it coincides with an Argon spectral line (e.g. 707 nm). If a photomultiplier is used with the spectrometer, powers greater than approximately  $10^{-6}$  W will cause nonlinear response. Hence, strong attenuation of the beam is required. It is desirable to bounce the beam off a ground glass screen so that only diffused light enters the spectrometer.

If the laser beam is attenuated before passing through the medium to the point that the intensity is less than the saturation intensity, then the experiment is in fact very similar to that with the incoherent source. The same complications as mentioned previously are applicable. However, now to plot metastable density as a function of time will require many discharge shots and many laser shots with variation of the time delay. The shot-to-shot reproducibility of both the TESLA discharge and the laser output will affect the accuracy of the results. If

sufficient intensity is available from the incoherent source, I would recommend that approach to the measurements.

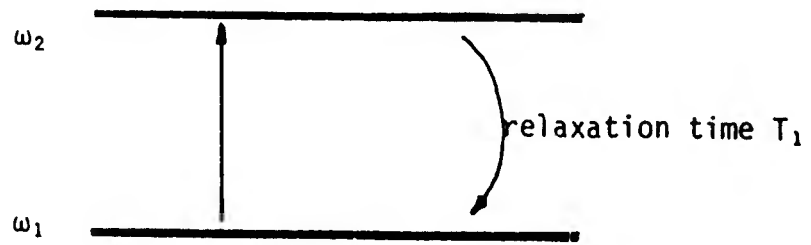
If the laser is not attenuated until after it traverses the medium, then it will saturate the medium and the change in intensity due to the presence of the discharge is

$$\Delta I = k_0 I_S \Delta z = f_{ms} N \tau \omega \Delta t \frac{1 + \gamma_l / \gamma_a}{1/\gamma_a + 1/\gamma_b}$$

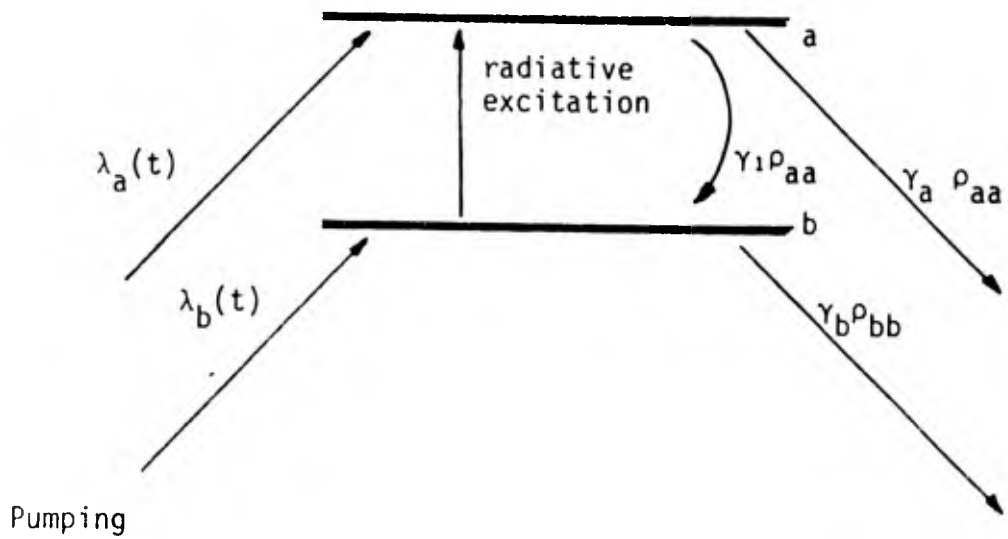
The relaxation parameters are known, and hence the fraction of atoms excited to the metastable states can be found directly from the intensity change. However, this requires calibration of the detection system.

#### Laser Induced Fluorescence Experiment

Refer to the papers of Daily - Applied Optics 15, 955 (1976); 16, 568 (1977); 17, 225 (1978) and to the discussion in an earlier section of this report.

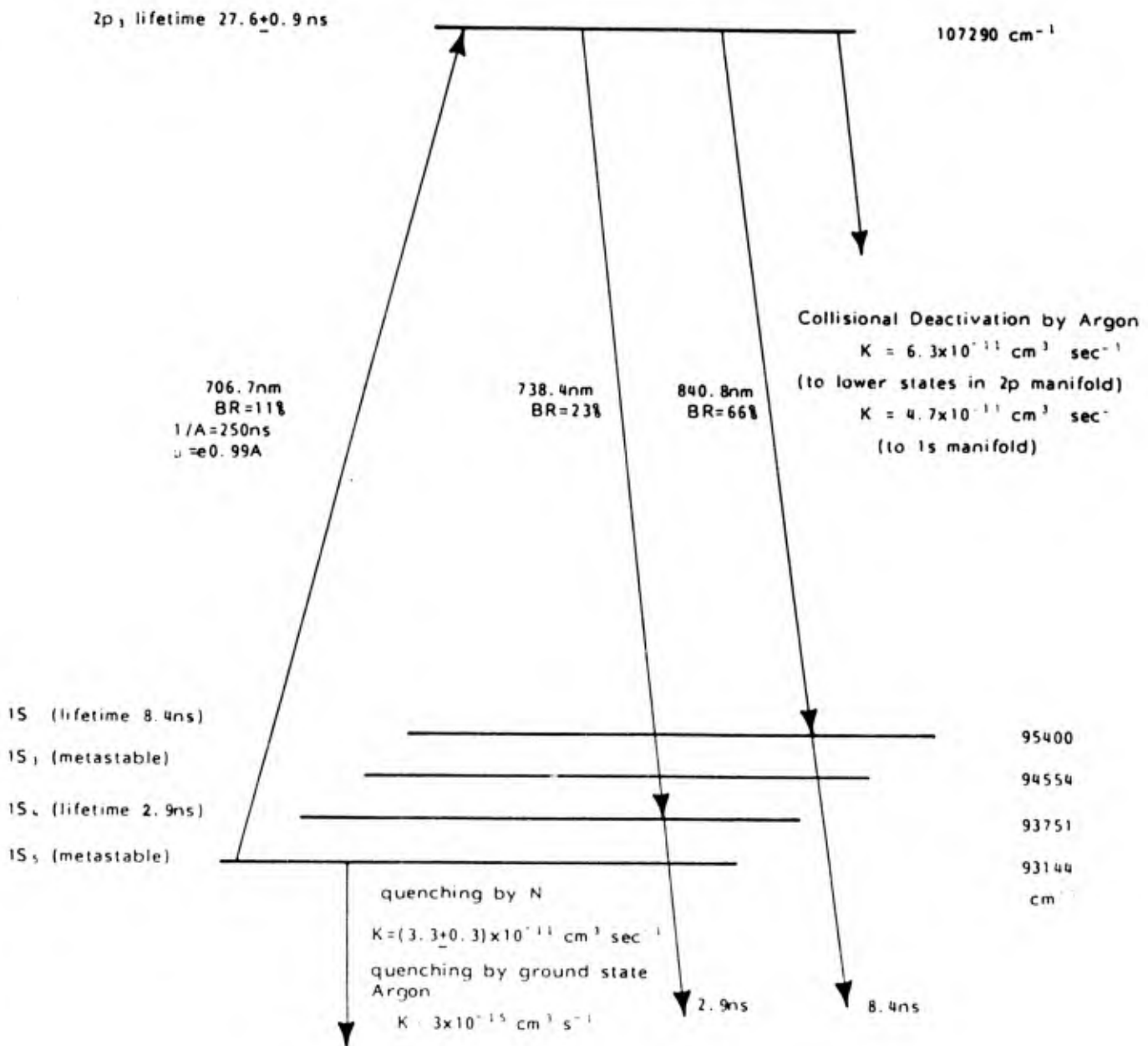


Case considered by Greenstein & Bates

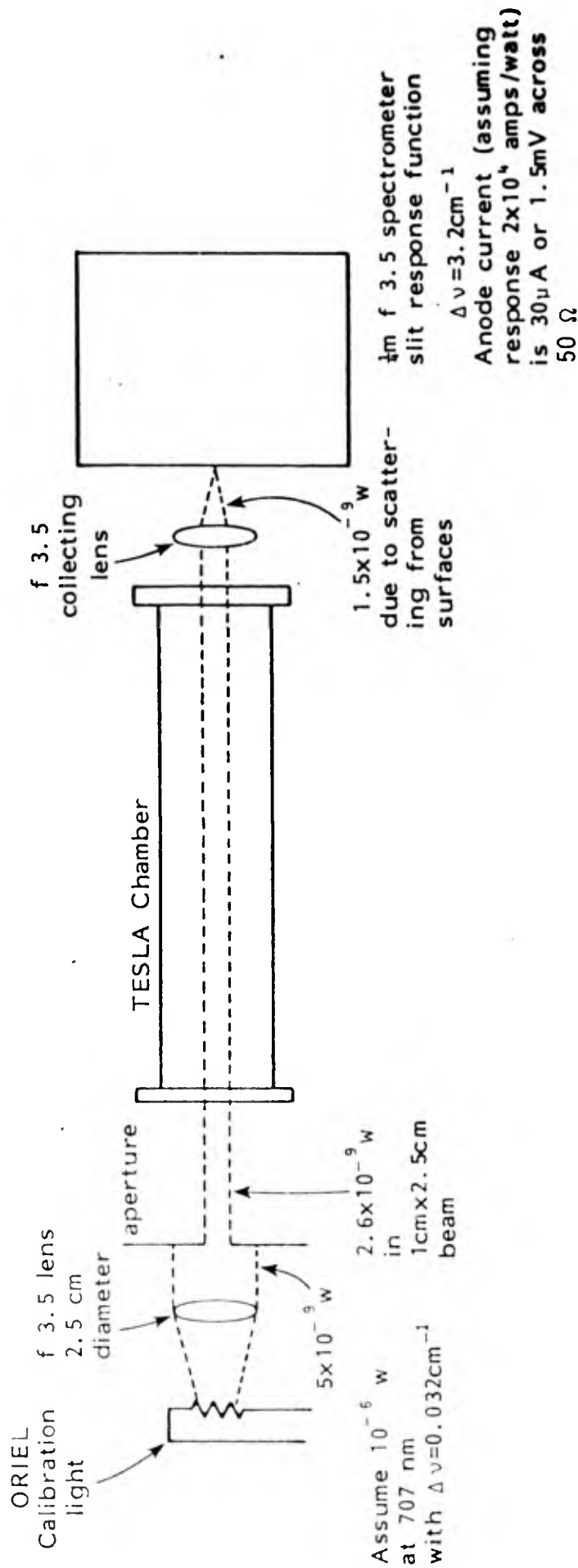


More general case (modified from Sargent, Scully, and Lamb).





DIAGNOSTICS OF METASTABLE ARGON



METASTABLE ABSORPTION EXPERIMENT  
Order of Magnitude Estimates